DETECTING MOTION OF A NANOMECHANICAL RESONATOR NEAR THE QUANTUM GROUND STATE

A Dissertation

Presented to the Faculty of the Graduate School

of Cornell University

In Partial Fulfillment of the Requirements for the Degree of

Doctor of Philosophy

by

Tchefor Tumasang Ndukum

January 2011

DETECTING MOTION OF A NANOMECHANICAL RESONATOR NEAR THE QUANTUM GROUND STATE

Tchefor Tumasang Ndukum, Ph. D.

Cornell University 2011

In the recent decade, tremendous amount of work has been done to probe the quantum properties of macroscopic mechanical devices. As a first step, researchers are racing to cool “large” mechanical objects to their quantum ground states. In this dissertation, I will describe the physics of the resolved sideband cooling technique used by our group to cool a nanomechanical resonator (NR) to its motional ground state. To this end we have fabricated high-Q NRs parametrically coupled to superconducting microwave coplanar waveguides (SR). We have been able to cool the motion of a 6.3 MHz nanomechanical resonator coupled to a 7.5 GHz superconducting resonator. Starting from a thermal occupation of ~500 quanta, we have observed mechanical occupation factors as low as 3.8 +/- 1.2 and expect the mechanical motion to be found with probability 0.21 in the quantum ground state of motion. I will describe the factors which are limiting further cooling and progress towards colder states of motion. By measuring differences in up and down-conversion of microwave photons in a process analogous to Raman scattering, we expect to observe fundamental quantum behavior of the nanomechanics. Furthermore, using a backaction evading configuration for our system, we should in principle be able to squeeze one of the quadratures of motion of the NR below the standard quantum limit.

The results of this dissertation and the future works indicate the path forward for future experiments that prepare, detect and manipulate non-classical states of NR motion.

BIOGRAPHICAL SKETCH

I was born in Bamenda, an exotic town full of life, in the North West Province of Cameroon. My secondary and high school education were done in Wum and Bambili all in the same Province. After high school, I was fortunate to be granted admission at the prestigious University of Buea, Cameroon. There I spent three happy though demanding years studying Physics and Mathematics with Computer Science as a minor. By this time in my educational career, I was very motivated and passionate about studying Physics and hence pursued my dream and accepted a position to do a masters degree at Cambridge University in the UK. Immediately after my time at Cambridge, I spent a year as a graduate teaching assistant at Michigan Technological University studying Physics. Later on I moved to Cornell University in the Fall of 2004 to pursue a PhD degree. I joined Prof Keith Schwab's group in the Spring of 2006 and immediately started working on cooling a mechanical device to its quantum ground state by coupling it to a quantum electrodynamics system. During the first two years of my degree, I was also heavily involved in a collaboration with Prof Kamil Ekinci's group of Boston University on the development of the novel ultra fast, high bandwidth rf-Scanning Tunneling Microscope.

After my PhD, I intend to take up a post doctoral position at the Massachusetts Institute of Technology to study the fundamental properties of suspended graphene devices.

… to Doris with love …

… and to my family …

'It always seems impossible until it is done!' – Nelson Mandela

ACKNOWLEDGMENTS

I want to first and foremost acknowledge the funding support I received during my time as a graduate research assistant at Cornell University. I am grateful to the Institute of African Development (IAD) and the Africana Center for paying my tuition during my first year (2004-2005) at Cornell University. Between 2006 and 2007, I was funded by an NSF grant through the Cornell Center for Materials Research (CCMR). Amongst other things, I was involved in a collaborative effort with Utku Kemiktarak and Prof Kamil Ekinci of Boston University on building a novel rf-Scanning Tunneling Microscope. Starting from the spring 2008 until the end of my time at Cornell, I was funded by a grant from the Foundational Questions Institute (FQXi) to probe quantum mechanics with mechanical structures.

I am very thankful to my family who consistently provided moral support and encouragement over the years. They were there to sympathize with me and say “ashia” during the low moments as well as celebrate with every breakthrough in the lab. To my wife Doris Ngemasong for enduring the marathon schedule that my PhD handed me. To my parents Teresa and Anderson Ndukum for making sure that I stayed focused in school in my childhood days. I know you are proud of this PhD achievement. Thank you to my siblings Julius, Mafor (R.I.P.), Ntsang, Boh, Bi, Luwani, Lum and Fru for encouraging me to always press on and for letting me know that you have my back. To my in-laws, Pascaline Awah-Ndukum and the Dickmu family, Matthew Ndonwi and his family and the Ngemasong family I thank you for your love and support.

I am indebted to Prof Keith Schwab for the opportunity to be part of his dynamic team of researchers. I am grateful for his mentorship, drive, leadership and

friendship during my graduate school life. I was particularly fortunate to be heavily involved in building his low temperature Lab at Cornell from scratch. Over the years Keith has taught me to be a fine low temperature experimentalist through hands-on exciting and novel research projects. He constantly pushed me to bring the best out of me both as an independent researcher as well as a team player. I count myself blessed to have been part of his research group.

During my PhD years, I was privileged to work with Tristan Rocheleau and Dr. Jared B. Hertzberg as Lab colleagues. I have learned a great deal from these talented scientists who shared the spirit of the Schwab group. Tristan's appreciation and knowledge of the little details and finesse that one would normally by-pass while setting up for an experiment ensured that we had high end quality and safe set ups to make our measurements. Jared was (and still is) selfless and tireless, very meticulous and pedantic on any experiment we worked on. This kept us grounded and patient as we had many second chances of re-validating findings of our experiments. I always had a friendly banter with Lord Darren Southworth who hung out with the Schwabies a lot of the time including group lunches and dinners. Thank you to Dr. Matt Shaw for your help during the last set of fabrications and measurements prior to the end of my PhD. Though it might have felt like we were passing on the baton, you provided extra man power which we so needed at the time. Thank you to Chris Macklin, Peter Hauck, Mannolis Savva, Madeleine Cobert, Peter Swift, Ross Anderson, Matt and Sara Brin Rothenthal who helped in practical ways to ensure that the experiments were running smoothly.

I specially thank Prof Aash Clerk for his theoretical input on all the major projects of this dissertation. With his in-depth knowledge of the physics we are after, I am appreciative of the fact that he was able to clearly and effectively communicate his

ideas to us experimentalists. The theoretical models of Chapter 2 are an extension of earlier discussions with him.

I want to thank the many experimental colleagues who made the basement of Clark Hall a bearable and fun place to do research as well as my theorist friends of the 5^{th} and 6^{th} floor. I also want to acknowledge my friends from Philip Hall, and the CNF clean room. I know you understand that it is arduous to acknowledge each and every one of you on this section of my dissertation. But I trust that you accept my thanks for your friendship and counsel over the years.

As an experimentalist, one gets to machine a lot of parts and adaptors for key apparatus. To Nate Ellis of the student machine shop, I want to thank you for your patience with me as you taught me how to make my first ever nut and bolt from a piece of aluminum stock. Thank you still for your help and advice as I later on took on machining adapters and parts for our experimental setup. Thank you to Stan Carpenter, Rodney, Jeff Koski, Chris Cowulich, Stan Macfolley of the machine shop for turning our design sketches into useable parts of our experimental set ups. I am sure you did not mind that I ate too many of your carrots during your lunch breaks. Thank you Eric Smith for your advice and suggestions on setting up our cryogenic systems. I am grateful that you were never bored by my constant barrage of what must have been trivial questions to you.

I lived with several housemates and neighbors who were a blessing to me during my stay in Ithaca. I want to extend my heartfelt thank you to Vashali Kushan, Marcus, Irene Capous, Johannes Lischner and Annita Ngatchou-Weiss for being great housemates and neightbors. My football (soccer) team, the Elite Laser Turbo Ninja, deserves special mention. It was a privilege to be part of the team and to have played consistently with you all at the top end of the Ithaca league.

Last but not the least, I want to thank Dr. Jared B. Hertzberg for reading the drafts of this dissertation and providing positive feedback and opinions on how to improve it. Thank you to my mom, Teresa Sirri Ndukum, for proof reading the introduction and conclusion of my dissertation. She gave me a helping hand to ensure that the introduction and conclusion were at least readable if not understandable to the general public.

Finally, I wish to express my sincere thanks to the members of my examination committee; Prof Keith Schwab, Prof Dan Ralph and Prof Erich Mueller. Thank you to Prof Paul McEuen for agreeing to sit-in for Prof Dan Ralph on my B-exam date.

TABLE OF CONTENTS

LIST OF TABLES

LIST OF FIGURES

LIST OF ABBREVIATION AND SYMBOLS

SR	Superconducting (Microwave) Resonator
NR	Nanomechanical Resonator
CPW	Coplanar Waveguide
Hs-SiNx	High Stress Silicon Nitride
ω_{sr}	Angular resonant frequency of SR
L	Effective inductance of the lumped LC model of the SR
C	Effective capacitance of the lumped LC model of the SR
C_1 (C_2)	Capacitance of input (output) coupler of the lumped model
V_{in} (V_{out})	Voltage at the input (output) of the SR
V	Voltage on the centerline of the SR
κ	Linewidth (damping) of SR
κ_{ext}	External dissipation of SR
κ_j	External dissipation through port j of SR, $j = 1,2,I$
Z	Effective characteristic impedance of the lumped LC model of the SR
R_L	Impedance of load or environment
Z_j	Impedance of coupling capacitor C_j at port j, $j = 1,2$
Φ	Flux through inductor L

Q	Charge on total capacitance
$\hat{a}$	lowering operator of SR
$\hat{P}$	power operator of SR
$\hat{b}_m$	lowering operator of bath mode, m
β_m	coupling constant of interaction Hamiltonian
$\hat{a}_{in}$ $(\hat{a}_{out})$	input (output) lowering field operator
P_{in} (P_{out})	input (output) power at the device
$f[\omega]$	Fourier transform of the function $f(t)$
ω_d, Δ	drive frequency, detuning from the SR frequency
$\bar{a}_{in,j}$ $(\bar{a}_{out,j})$	average input (output) classical drive at port j, $j = 1,2,I$
$P_{in,j}$ $(P_{out,j})$	input (output) power at the device
$\bar{a}$	average classical drive inside the SR
$\hat{\zeta}_{\mathrm{j}}$ $(\hat{\mathcal{A}}_{\mathrm{j}})$	quantum noise in input (output) drive at port j, $j = 1,2,I$
$\hat{d}$	quantum noise in cavity
$\chi_{\mathrm{sr}}^{\Delta}$	cavity susceptibility at Δ detuning
$\bar{n}_p$	average number of pump quanta (photons) in SR
S_{21} (S_{11})	transmission (reflection) coefficient of the SR
$\bar{n}_j^T$	effective thermal noise entering at port j, $j = 1,2,I$

$\bar{n}_{sr}^{T}$	thermal occupation of SR
$\bar{S}_{\hat{\mathcal{A}}_j}[\omega]$	symmetric-in-frequency noise spectrum at port j, $j = 1,2,I$
ω_m	Angular resonant frequency of NR
m	Effective mass of NR
γ_m	Intrinsic linewitdth of NR
$C_{NR}(x)$	Capacitance between NR and gate of SR
C_{NR}^{0}	Equilibrium capacitance between NR and SR gate
$[\partial_x C_{NR}(0)]$	Capacitative coupling constant
d	gap separation between NR and SR gate
g	coupling constant
x_{zpf}	zero point fluctuation
$\hat{c}$	lowering operator of NR
δ_R (δ_B)	detuning of red (blue) sideband from SR resonance
χ_m	mechanical susceptibility
α_R (α_B)	Effective coupling constant for single red (blue) pump drive
χ_{sr}^{r} (χ_{sr}^{b})	SR susceptibility for the red (blue) sideband
χ_m^r (χ_m^b)	Effective mechanical susceptibility in the presence of SR backaction from the red (blue) pump
χ_{ba}^{r} (χ_{ba}^{b})	SR backaction susceptibility for the red (blue) pump drive

$\hat{\eta}$	noise associated with intrinsic mechanical damping
$\bar{n}_m^T$	number of thermal quanta in the intrinsic bath coupled to the NR
$\bar{n}_m$	number of mechanical quanta in NR
$S_{xx}[\omega]$	position spectrum of the NR
Γ_R (Γ_B)	optical scattering rate for the single red (blue) drive
$\bar{n}_{sr,R}^T$ ($\bar{n}_{sr,B}^T$)	SR noise occupation associated with the red (blue) drive
$\delta\omega_m^R$ ($\delta\omega_m^B$)	Optical frequency shift due to red (blue) pump
Γ_t^R (Γ_t^B)	net scattering rate for the single red (blue) drive
$\bar{S}_{\mathcal{A}_2}^R$ ($\bar{S}_{\mathcal{A}_2}^B$)	symmetric-in-frequency noise spectrum associated with the output field $\hat{\mathcal{A}}_2$ for the single red (blue) drive.
$\bar{n}_{eff}^R$ ($\bar{n}_{eff}^B$)	effective quanta measured in the red (blue) sideband of the output spectrum
χ_m^{br}	Effective mechanical susceptibility in the presence of SR backaction for the double pump configuration.
$\delta\omega_m^{BR}$	Optical frequency shift for the double pump case
X_1 (X_2)	cosine (sine) quadrature of the NR position.
α	effective coupling constant for double pump configuration
$\bar{n}_{BA}$	effective number of quanta associated with backaction heating
S_{X_1} (S_{X_2})	position spectral density of X_1 (X_2) quadrature of the NR

$S_{\mathrm{X}_1,meas}$	spectrum of measured quadrature, X_1
$\Delta\mathrm{X}_1^2$	position uncertainty of X_1 quadrature
n_{add}	effective quanta associated with added noise from amplifier and backaction heating (in bad cavity limit)
Z_{ch}^{CPW}	characteristic line impedance of CPW of SR
$\varepsilon_{r,eff}$	effective dielectric constant
S_P^{SA}	power spectrum of output noise measured by SA
$S_P^{SA,bgd}$	background of power spectrum measured by SA
G	net gain between output of sample and SA
P_{tr}	transmitted power measured by SA
G_{amp}	net gain between the HEMT and the SA
T_N^{HEMT}	noise temperature of the the HEMT
A_o	attenuation between the output of the sample and the input of the HEMT
I_P^{SA}	area under $S_P^{SA}[\omega]$ normalized by the transmitted power
T_m	temperature of NR
k_{eff}	effective spring constant
S_F	force bath that randomly drives NR at low temperatures <150mK

CHAPTER 1: INTRODUCTION

Since its early days, quantum mechanics has been used to accurately describe fundamental physics phenomena of microscopic systems. For this "tiny" systems it is a given that quantum effects should be observable if one makes a careful and precise measurement. There is no fundamental reason from the theoretical point of view that macroscopic systems can not behave quantum mechanically. Technological advances in data acquisition, high speed measurements, ultra high isolation of measurement systems and nanotechnology has paved the way to a new branch of Physics which studies the quantum behavior of macroscopic mechanical objects [1, 2]. Until fairly recently, there were open ended questions in this physics community about the prospect of seeing quantum mechanics in macroscopic mechanical objects. Questions like; Is it possible to make a macroscopic mechanical object behave quantum mechanically? Can a large object of ~10^{12} atoms be cooled to its quantum ground state? Is there a universal classical/quantum boundary? And if so, what are the implications.

As a first goal, a tremendous amount of research has been and is being done to cool macroscopic mechanical devices to their motional quantum ground state. This would be a definite confirmation that "quantumness" does not discrimate when it comes to size of an object. One of the main hindrance of cooling to the ground state is the fact that the temperatures required are typically lower than the base temperature of standard cryogenic fridges. To this end, researchers have developed alternate cooling techniques and have been able to cool macroscopic mechanical devices to 140 quanta [3], 63 quanta [4], 37 quanta [5], 30 quanta [6], 25 quanta [7]. Most recently at the beginning of 2010, our group has shown cooling of a 6 MHz nanomechanical

resonator down to 3.8 +/- 1.2 quanta [8] which is tantalizingly close to the ground state. We are only rivaled by the group of [9] who were able to couple their 6 GHz mechanics to a qubit and by brute force cool it to the motional ground state of the mechanics. With the qubit prepared in the ground state at a fridge temperature of 25mK, the average number of quanta on their mechanics was found to be below 0.07. This was confirmed by the fact that the coupled qubit stayed in its ground state and was not excited. The absence of any qubit excitation implies the absence of quanta in their mechanics. In our group we use a novel approach called resolved sideband cooling technique and are able to track the average occupation of a nanoresonator (NR) to near its ground state. These recent breakthrough measurements reinforce the assertion that macroscopic mechanical objects behave quantum mechanically hence opening up the field to new possibilities. Researchers in the field are making progress on demonstrating quantum limited position detection below the standard quantum limit, creating non-classical states (e.g. squeezed-states, Fock states) which ultimately lead to the creation of entangled states of the macroscopic mechanical object.

Cooling a NR to its quantum ground state can be achieved in principle by coupling it to a superconducting microwave resonator (SR) [10]. The mechanical motion of the NR in the SR can be cooled by applying a red detuned drive at exactly one mechanical frequency lower than the SR resonance [3-6, 11, 12, 13, 14]. This red signal will scatter quanta off the NR into the high density of state SR in a dynamical backaction process and cool the NR. This upconversion depends directly on the coupling strength between the NR and the SR. By increasing the strength of the red drive, one can in principle cool the NR to its ground state in the resolved sideband regime. In practice, there are a few challenges that need to be dealt with. By applying a single blue detuned drive at one mechanical frequency higher than the SR resonance, the reverse

process occurs. The blue signal will populate the NR by downconverting photons from the SR to phonons on the NR in a backaction heating process. By applying a strong red and a weak blue signal simultaneously, the disparity between the upconverted and downconverted quanta can be measured. The true signature of this disparity would be an extra quantum resulting from the blue signal compared to the red. If the strength of the double pump signals are equal, we can make quantum non-demolition measurements on one of the quadratures of motion of the NR. This measurement evades the backaction processes described above and in principle can be used to squeeze the NR to below the standard quantum limit.

In this dissertation I will describe the recent key achievements of our group towards observing quanta in macroscopic mechanics. This work is as much a product of the whole research group as it is mine. I was heavily involved in the design and fabrication of all the devices reported in this dissertation. This included the theoretical estimates, the design, the actual fabrication and inspection of the devices and sample packaging and mounting on the fridge. I took part in building the experimental set ups used for measuring the devices. Amongst other things I was in charge of designing a triangle optical table for the dilution fridge as well as the plumbing lines that connect the pump room and the top of the fridge. I machined adaptors and bracket holders used to thermalize the drive and return lines to the various stages of the interior of the dilution fridge. Each component of the fridge line was tested at 4K to ensure they were within specification before mounting on the fridge line. I was heavily involved in the many device cool downs we had to do to characterize and measure devices. A typical cool down consisted of mounting the sample box containing the device on the sample stage, sealing the inner vacuum space, pre-cooling the fridge to 77K, then to 4.2 K after whence we condense a ^{3}He-^{4}He mixture provided by Oxford Instruments^{TM} to

cool the sample stage to milli-Kelvin temperatures. I was involved in all the measurements and analysis that were made on the devices reported in this dissertation.

This dissertation is designed as follows: In Chapter 2 I model the SR as a two-sided cavity and provide a thorough and detailed calculation, using input output theory, of the microwave fields inside and outside the SR. I extend the theory to include the NR coupled to the SR and derive analytic expressions of the power spectrum at the output of the NR-SR for various pump configurations. In Chapter 3, I have described the design and material considerations for our SR and NR-SR devices. In addition, I discuss the fabrication process sequence for making the SR and NR-SR devices of this dissertation. The set ups used for diagnostic measurements at 1K and also for more elaborate measurements at mK temperatures is discussed in Chapter 4. Chapter 5 deals with the measurement methods used in characterizing the SR devices and the NR of the NR-SR devices. In Chapter 6 I report the results of our key measurements and provide some discussion in comparison to the theory provided in Chapter 2. Finally I end with a brief concluding Chapter 7 with suggestions of possible future works.

CHAPTER 2: INPUT-OUTPUT FORMALISM FOR NANOMECHANICAL RESONATOR COUPLED TO MICROWAVE RESONATOR

The quantum properties of a nanomechanical resonator (NR) can be studied by coupling it to a superconducting microwave resonator (SR). Fluctuations of the NR perturb the microwave properties of the SR and vice versa and this can be read out with the appropriate setup [10]. Thus it is essential to understand the quantum properties of the bare SR and then couple a NR to it to study the full NR-SR system. This chapter presents a quantum derivation of the basic power and noise properties of a high quality SR in section 2.1 and that of an NR-SR system in section 2.2. Section 2.1 describes the input-output theory which models a microwave resonator as a cavity coupled to a bath of harmonic oscillators [18-23]. It discusses the power coupled into and out of the cavity, and the noise spectrum obtained for a two-sided cavity. Section 2.2 extends the model to include a NR coupled to the SR.

2.1 I/O Formulation for Microwave Resonators

2.1.1 Quantization of the Microwave Field of a Microwave Resonator

A coplanar waveguide with a centerline isolated from two ground planes can be used as a microwave resonator (See Figure 2.1). In particular, using an aluminum (Al) or a niobium (Nb) center line below their superconducting transition temperature, it is possible to fabricate a high-Q SR [15, 16, 17]. The angular frequency, $\omega_{sr} = 1/\sqrt{LC_o}$, of the SR mode is determined both by the total effective capacitance, C_o and the effective inductance, L of the SR. The total capacitance $C_o = C + C_1 + C_2$ is the

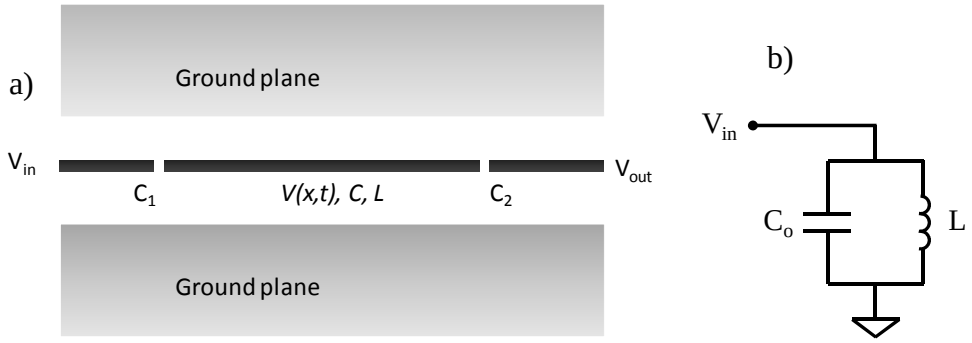

Figure 2.1 a) Physical layout of a coplanar waveguide resonator showing the center line and the adjacent ground planes. Input microwave voltage, V_{in}, creates a standing wave at resonance, V(x,t), inside the SR. Capacitors C_1 and C_2 couple the microwave into and out of the resonator. b) Equivalent LC circuit of microwave resonator

parallel combination of the transmission line, the input (port 1) and the output (port 2) capacitances. The net dissipation of the SR, $\kappa = \kappa_I + \kappa_{ext}$, is given by the sum of the internal (κ_I) and external (κ_{ext}) dissipation of the system. Furthermore, we can write $\kappa_{ext} = \kappa_1 + \kappa_2$ where $\kappa_j = \omega_{sr} Z R_L / Z_j^2$, $j = 1, 2$, is the dissipation associated with port j of the SR. Where $Z = \sqrt{L/C}$ is the characteristic impedance of the SR, $Z_j = 1/\omega C_j$ is the impedance of the coupling capacitor, C_j, at port j and R_L is the impedance of the 50-Ohm environment . The quantization of the transmission line mode of such a SR has been studied elsewhere (see for instance [20], [18], [19]). This is obtained by modeling the SR as an infinite series of parallel LC circuits, solving Hamilton's equation for this model and then quantizing the results. Below we sketch the basic derivation and results for a single LC circuit. From the equivalent parallel LC circuit, we can write the classical Hamiltonian of the SR as

$$H = \frac{\Phi^2}{2L} + \frac{Q^2}{2C_o} \tag{2.1}$$

Where Q is the charge on C_o and Φ is the net flux through the inductor L. By imposing the commutation relation $\left[\hat{Q}, \hat{\Phi}\right] = i\hbar$ we can define the SR lowering operator as

$$\hat{a} = \frac{1}{\sqrt{2\hbar}}\left[\sqrt{\omega_{sr}L}\hat{Q} + i\frac{1}{\sqrt{\omega_{sr}L}}\hat{\Phi}\right] \tag{2.2}$$

with $[\hat{a}, \hat{a}^\dagger] = 1$. The Hamiltonian of Eq. 2.1 can now be quantized in the Schrodinger picture to read

$$H_{sr} = \hbar\omega_{sr}\left(a^\dagger a + \frac{1}{2}\right) \tag{2.3}$$

Thus, given $\hat{a}$, the state of the transmission line is completely specified. The voltage, $\hat{V} = \hat{Q}/C_o$ (and hence power, $\hat{P} = \hat{V}^2/Z$), operators of the SR can be related to the mode operator, $\hat{a}$, according to the relation [18, 20]

$$\hat{V} = \sqrt{\frac{\hbar\omega_{sr}Z}{2}}\left[\hat{a} + h.c.\right] \tag{2.4}$$

2.1.2 Microwave Resonators as Cavities: Input-Output Formulation

Consider a high-Q single mode cavity (or SR) interacting with the modes of an external bath. The Hamiltonian that describes this system is given by [18], [21], [22], [23]

$$H = H_{sr} + H_{bath} + H_{int}$$

Here, H_{sr} is the Hamiltonian describing the intracavity mode $\hat{a}$, H_{bath} represents the bath and H_{int} is the interaction between the bath and the intracavity field. In this dissertation, we concentrate on a single mode linear cavity modeled as a simple harmonic oscillator (SHO) as shown above in Section 2.1.1. The bath is modeled as a

linear combination of independent SHOs with mode operators $\hat{b}_m$.The bath Hamiltonian can be written as

$$H_{bath} = \sum_m \hbar\omega_m \left(\hat{b}_m^\dagger \hat{b}_m + \frac{1}{2}\right) \tag{2.5}$$

where the bosonic bath mode operators obey $\left[\hat{b}_m\,, \hat{b}_{m'}^\dagger\right] = \delta_{m,m'}$. Physically, for our system, the bath represents all the other modes of the NR that we are not considering in addition to the surrounding thermal stage of the fridge on which the SR is mounted. Basically, it is the portion of the environment that provides a dissipative channel for photons to leak out of the SR. To linear order, the interaction between the bath mode and the intracavity mode can be written as

$$H_{int} = \sum_m i\hbar\left[\beta_m \hat{b}_m \hat{a}^\dagger - \beta_m^* \hat{a}\hat{b}_m^\dagger\right] \tag{2.6}$$

where β_m is the coupling constant. By using the rotating wave approximation, the interaction terms $\hat{a}\hat{b}_m,\ \hat{a}^\dagger\hat{b}_m^\dagger$ have been neglected in the linear coupling. These terms give rise to signals that oscillate at a higher frequency and hence are discarded.

In the Heisenberg picture, the equation of motion for $\hat{b}_m$ the bath modes is given by[‡]

$$\partial_t \hat{b}_m(t) = \frac{1}{i\hbar}\left[\hat{b}_m(t), H\right] = -i\omega_m \hat{b}_m(t) + \beta_m^* \hat{a}(t) \tag{2.7}$$

Eq. 2.7 can be solved exactly in the time domain using Green's functions[§]. The solution can be written either in terms of the initial conditions at time $t < t_0$ representing the input bath field or in terms of the final conditions at time $t_1 > t$

[‡] In Eq. 2.7, $\partial_t = \frac{d}{dt}$ is the time derivative operator.

[§] A homogeneous differential equation $D_x y(x) = z(x)$ can be solved using the Green's function $G(x;x')$ which has the special property that $D_x G(x;x') = \delta(x - x')$. If $D_x y_o(x) = 0$, then the solution of the homogeneous equation is $y(x) = y_o(x) + \int dx' G(x;x') z(x')$.

representing the output field. The complete solution of Eq. 2.7 for initial condition $t < t_0$ is given by

$$\hat{b}_m(t) = e^{-i\omega_m(t-t_0)}\hat{b}_m(t_0) + \int_{t_0}^{t} dt' e^{-i\omega_m(t-t')}\beta_m^*\hat{a}(t') \tag{2.8}$$

where the first term represents the free bath evolving over time and the second term results from the interaction between the bath and the cavity. The evolution of the bath modes can also be solved from Eq. 2.7 for future times $t > t_1$ in a similar manner to give

$$\hat{b}_m(t) = e^{-i\omega_m(t-t_1)}\hat{b}_m(t_1) - \int_{t}^{t_1} dt' e^{-i\omega_m(t-t')}\beta_m^*\hat{a}(t') \tag{2.9}$$

The equation of motion of the intracavity mode, $\hat{a}$, in the Heisenberg picture is given by

$$\partial_t\hat{a}(t) = \frac{1}{i\hbar}[\hat{a}(t), H_{sr}] - \sum_m \beta_m\hat{b}_m(t) \tag{2.10}$$

Substituting Eq. 2. 8, the solution of the bath mode in terms of the initial condition, into Eq. 2.10 leads to

$$\partial_t\hat{a} = -i\omega_{sr}\hat{a} - \sum_m e^{-i\omega_m(t-t_0)}\beta_m\hat{b}_m(t_0) - \sum_m \int_{t_0}^{t} dt' e^{-i\omega_m(t-t')}|\beta_m|^2\hat{a}(t') \tag{2.11}$$

At this point we make use of the Markov approximation that the cavity decay rate, κ, given by Fermi's golden rule[**] is independent of frequency. Using the fact that [18]

1) $\sum_m e^{-i(\omega_m-\omega_{smr})(t-t')}|\beta_m|^2 = \kappa\delta(t-t')$ and (2.12)
2) $\int_{t_0}^{t} f(t')\delta(t-t') = \frac{1}{2}f(t), t < t_0$

[**]The decay rate from a single photon excited state to a zero photon ground state is given according to Fermi's golden rule by $\kappa(\omega_{sr}) = 2\pi\sum_m|\beta_m|^2\delta(\omega_m - \omega_{sr})$

we simplify the last term of Eq. 2.11. The algebra leads to

$$\partial_t \hat{a}(t) = -i\omega_{sr}\hat{a}(t) - \frac{\kappa}{2}\hat{a}(t) - \sum_m e^{-i\omega_m(t-t_0)}\beta_m \hat{b}_m(t_0) \tag{2.13}$$

We can appropriately define the input field operator, $\hat{a}_{in}$, as

$$\hat{a}_{in}(t) = \frac{1}{\sqrt{2\pi\rho}}\sum_m e^{-i\omega_m(t-t_0)}\hat{b}_m(t_0) \tag{2.14}$$

where $\rho = \sum_m \delta(\omega_{sr} - \omega_m) = \frac{\kappa}{2\pi\beta^2}$ is the density of states and $\sqrt{|\beta_m|^2} = \beta$ is independent of frequency by the Markov approximation. Using Eq. 2.12, we can show that the input field is bosonic with $\left[\hat{a}_{in}(t), \hat{a}_{in}^\dagger(t')\right] = \delta(t-t')$ and $[\hat{a}_{in}(t), \hat{a}_{in}(t')] = 0$. Thus Eq. 2.13 simplifies to a compact form given by

$$\partial_t \hat{a}(t) = -i\omega_{sr}\hat{a}(t) - \frac{\kappa}{2}\hat{a}(t) - \sqrt{\kappa}\hat{a}_{in}(t) \tag{2.15}$$

where the last term conveniently keeps track of the input field (including noise) entering the cavity. Eq. 2.15 is the so called Quantum Langevin equation for the damped amplitude $\hat{a}(t)$ with noise in the input field. Notice that from dimensional analysis that, since $\hat{a}$ is unitless with $\langle \hat{a}^\dagger \hat{a} \rangle =$ number of photons in the cavity, then $\hat{a}_{in}$ has to have units of $\sqrt{\omega}$ with $\langle \hat{a}_{in}^\dagger(t)\hat{a}_{in}(t)\rangle = P_{in}(t)/\hbar\omega$. Where P_{in} is the input power at the SR. See [18] for more details.

Using the solution of Eq. 2.7 for future times $t > t_1$ given by Eq. 2.9 and following the same arguments above, we can write (similar to Eq. 2.14) the output field operator, $\hat{a}_{out}$, as

$$\hat{a}_{out}(t) = \frac{1}{\sqrt{2\pi\rho}}\sum_m e^{-i\omega_m(t-t_1)}\hat{b}_m(t_1) \tag{2.16}$$

The commutation relations of the output field are also bosonic with $\left[\hat{a}_{out}(t), \hat{a}_{out}^\dagger(t')\right] = \delta(t-t')$ and $[\hat{a}_{out}(t), \hat{a}_{out}(t')] = 0$. In like manner, the

equation of motion of the intracavity mode (Eq. 2.10) can be written in terms of the output field as

$$\partial_t \hat{a} = -i\omega_{sr}\hat{a} + \frac{\kappa}{2}\hat{a} - \sqrt{\kappa}\hat{a}_{out}(t) \tag{2.17}$$

Analogous to the input power, we can compute the output power, P_{out}, in terms of the output field operators using the equation $\langle \hat{a}_{out}^{\dagger}(t)\hat{a}_{out}(t)\rangle = P_{out}(t)/\hbar\omega$. Subtracting Eq. 2.17 from Eq. 2.15, we get

$$\hat{a}_{out}(t) = \hat{a}_{in}(t) + \sqrt{\kappa}\hat{a} \tag{2.18}$$

which is the expected conservation relation between the output bath field, the input bath field and the intracavity field.

The equation of motion for the intracavity mode given by Eq. 2.15 and 2.17 can be solved exactly in time domain using Green's function as described above for the bath mode. The solution in terms of the initial conditions for times $t < t_0$ (Eq. 2.15) is

$$\hat{a}(t) = e^{-(i\omega_{sr}+\kappa/2)(t-t_0)}\hat{a}(t_0) - \sqrt{\kappa}\int_{t_0}^{t} dt' e^{-(i\omega_{sr}+\kappa/2)(t-t')}\hat{a}_{in}(t') \tag{2.19}$$

while the solution in terms of the final conditions for later times $t_1 > t$ (Eq. 2.17) is

$$\hat{a}(t) = e^{-(i\omega_{sr}-\kappa/2)(t-t_1)}\hat{a}(t_1) + \sqrt{\kappa}\int_{t}^{t_1} dt' e^{-(i\omega_{sr}-\kappa/2)(t-t')}\hat{a}_{out}(t') \tag{2.20}$$

The first terms in both Eq. 2.19 and 2.20 are transient terms and describe the cavity before its interaction with the bath field. We will neglect in the limit $t_0 \longrightarrow -\infty$ ($t_1 \longrightarrow +\infty$) the initial (final) transient in Eq. 2.19 (2.20).

Eq. 2.15 and 2.17 can also be solved in the frequency domain with the help of Fourier transforms. In this dissertation, we define the Fourier components of an operator $\hat{f}$ as follows[††]

$$\hat{f}[\omega] = \int_{-\infty}^{+\infty} e^{i\omega t}\hat{f}(t)dt \ , \qquad \hat{f}^{\dagger}[\omega] = \int_{-\infty}^{+\infty} e^{i\omega t}\hat{f}^{\dagger}(t)dt \tag{2.21}$$

$$\hat{f}(t) = \frac{1}{2\pi}\int_{-\infty}^{+\infty} e^{-i\omega t}\hat{f}[\omega]d\omega, \qquad \hat{f}^{\dagger}(t) = \frac{1}{2\pi}\int_{-\infty}^{+\infty} e^{-i\omega t}\hat{f}^{\dagger}[\omega]d\omega \tag{2.22}$$

Using Eq. 2.21, we can Fourier Transform Eq. 2.15 and 2.17 and simplify to get

$$\hat{a}[\omega] = \frac{\sqrt{\kappa}}{i(\omega-\omega_{sr})-\kappa/2}\hat{a}_{in}[\omega] = \frac{\sqrt{\kappa}}{i(\omega-\omega_{sr})+\kappa/2}\hat{a}_{out}[\omega] \tag{2.23}$$

Hence we can write the relationship between the output and the input field as

$$\hat{a}_{out}[\omega] = \frac{i(\omega-\omega_{sr})+\kappa/2}{i(\omega-\omega_{sr})-\kappa/2}\hat{a}_{in}[\omega] \tag{2.24}$$

As expected, the bath fields and the intracavity field in Fourier space obey the analog commutation relation of the time domain. To see this, consider $\hat{\vartheta} \in \{\hat{a}, \hat{a}_{in}, \hat{a}_{out}\}$ then

$$\left[\hat{\vartheta}[\omega], \hat{\vartheta}^{\dagger}[\omega']\right] = \int_{-\infty}^{+\infty} dt \int_{-\infty}^{+\infty} dt' e^{i\omega t}e^{i\omega' t'}\left[\hat{\vartheta}[t], \hat{\vartheta}^{\dagger}[t']\right]$$

$$= \int_{-\infty}^{+\infty} dt \int_{-\infty}^{+\infty} dt' e^{i\omega t}e^{i\omega' t'}\delta(t-t') = \int_{-\infty}^{+\infty} dt e^{i(\omega+\omega')t} = 2\pi\delta(\omega+\omega') \tag{2.25}$$

and similarly

$$\left[\hat{\vartheta}[\omega], \hat{\vartheta}[\omega']\right] = 0 \tag{2.26}$$

At this point, it is instructive to apply this theory to the two-sided cavity that accurately models the experimental set up which forms the basis of this dissertation.

[††] Notice that this definition implies that $\hat{f}^{\dagger}[\omega] = \left(\hat{f}[-\omega]\right)^{\dagger}$.

2.1.3 A Two-Sided Cavity – Driven from one port only

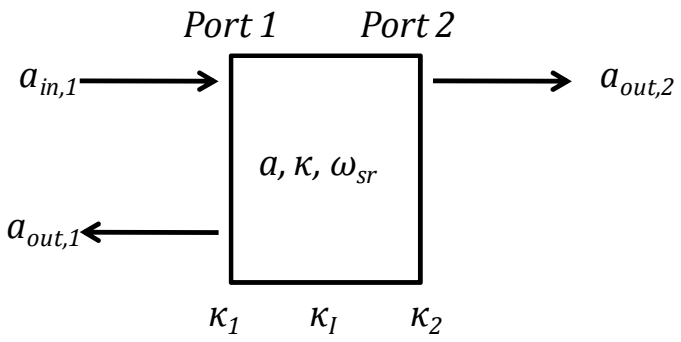

Figure 2.2 Schematic diagram of a two-sided cavity

The two-sided cavity has two physical ports, 1 and 2, and a third internal port, I, associated with internal losses. This can be used to model a half-wave SR (see Figure 2.1) used by our group to study the quantum properties of a NR. In most practical situations, the two-sided cavity is driven from one port only, say port 1, as shown in Figure 2.2. Port 2 which is a potential entry point of quantum vacuum noise is used for read-out. The external dissipation from port 1 and 2 are κ_1 and κ_2. Hence the total dissipation is $\kappa = \kappa_{ext} + \kappa_I$, where κ_I is the internal dissipation and $\kappa_{ext} = \kappa_1 + \kappa_2$ is the external dissipation of the two-sided cavity device. In the remainder of this sub-section, we go through the derivation of the expressions for the average photon occupation, the reflection and transmission coefficients and the output noise spectrum from port 2 of the SR.

The equation of motion of the intracavity mode using the initial conditions and the conservation equations are

$$\partial_t \hat{a}(t) = -i\omega_{sr}\hat{a}(t) - \frac{\kappa}{2}\hat{a}(t) - \sqrt{\kappa_1}\hat{a}_{in,1}(t) - \sqrt{\kappa_2}\hat{\zeta}_2(t) - \sqrt{\kappa_I}\hat{\zeta}_I(t) \tag{2.27}$$

$$\hat{a}_{out,1}(t) = \hat{a}_{in,1}(t) + \sqrt{\kappa_1}\hat{a}(t) \tag{2.28}$$

$$\hat{a}_{out,j}(t) = \hat{\zeta}_j(t) + \sqrt{\kappa_j}\hat{a}(t), \qquad j = 2, I \tag{2.29}$$

where the terms have their usual meaning and $\hat{\zeta}_{2(I)}(t)$ is the vacuum noise entering from port 2(I), despite the absence of a drive at these port. At low temperatures (~100s of mK) and high frequencies (~10s of GHz), vacuum noise results mainly from zero-point fluctuation effects of the electromagnetic field [24]. Driving at port 1 introduces both the classical drive and quantum noise at the port. Physically, the quantum noise is due to the electrical field fluctuations both from Johnson-Nyquist and shot noise at the input of the SR [25, 26]. At low temperatures, shot noise which is equivalent to current fluctuations resulting from the discreteness of the electrical charge dominates [27, 28]. Taking the input field at port 1 to be a detuned coherent drive at $\omega_d = \omega_{sr} + \Delta$, we can write [11]

$$\hat{a}_{in,1}(t) = e^{-i\omega_d t}\left[\bar{a}_{in,1} + \hat{\zeta}_1(t)\right] \tag{2.30}$$

consisting of a quantum noise part, $\hat{\zeta}_1$, and the classical drive $\bar{a}_{in,1}$ from a microwave source. The presence of the quantum noise in our system introduces the "quantumness" of this calculation. The expressions obtained below for the quantum noise are fully quantum mechanical as they derive from constrains set by the quantum nature of the noise [18] at the inputs of the cavity. The expressions obtained from the classical drive terms are classical as expected. Notice that we can reproduce the classical expressions below if we use the equivalent lumped circuit models of Figure 2.1 and consider the voltages at the input, inside and output of the SR device. See for instance Hertzberg's PhD dissertation [37]. Similar to Eq. 2.30, the cavity and output fields will also have the same functional form and so we write in a frame rotating at ω_d that[‡‡]

[‡‡] In the equations that follow in this section, the transformation $\omega \to \omega - \omega_{sr} - \Delta$ takes us back to the lab frame.

$$\hat{a}_{in,1}(t) = \bar{a}_{in,1} + \hat{\zeta}_1(t) \tag{2.31}$$

$$\hat{a}(t) = \bar{a} + \hat{d}(t) \tag{2.32}$$

$$\hat{a}_{out,j}(t) = \bar{a}_{out,j} + \hat{\mathcal{A}}_j(t), \qquad j = 1, 2, I \tag{2.33}$$

The relationship between the input and output bath fields and the intracavity mode for the two-sided cavity can be solved in frequency space. Fourier transforming Eq. 2.27-2.29 and using the corresponding Fourier transforms of Eq. 2.31-2.33, leads to

$$-\omega\hat{d}[\omega] = \left(i\Delta - \frac{\kappa}{2}\right)\left(\bar{a} + \hat{d}[\omega]\right) - \sqrt{\kappa_1}\bar{a}_{in,1} - \sum_{j=1,2,I}\sqrt{\kappa_j}\hat{\zeta}_j[\omega] \tag{2.34}$$

$$\bar{a}_{out,1} + \hat{\mathcal{A}}_1[\omega] = (\bar{a}_{in,1} + \hat{\zeta}_1[\omega]) + \sqrt{\kappa_1}(\bar{a} + \hat{d}[\omega]) \tag{2.35}$$

$$\bar{a}_{out,j} + \hat{\mathcal{A}}_j[\omega] = \hat{\zeta}_j[\omega] + \sqrt{\kappa_j}\left(\bar{a} + \hat{d}[\omega]\right), \qquad j = 2, I \tag{2.36}$$

From Eq. 2.34, we can separate the classical drive and the quantum noise terms to write

$$\bar{a} = \sqrt{\kappa_1}\chi_{sr}^{\Delta}[0]\bar{a}_{in,1} \tag{2.37}$$

$$\hat{d}[\omega] = \chi_{sr}^{\Delta}[\omega] \sum_{j=1,2,I}\sqrt{\kappa_j}\hat{\zeta}_j[\omega] \tag{2.38}$$

Where $\chi_{sr}^{\Delta}[\omega] = 1/[i(\omega + \Delta) - \kappa/2]$ is the cavity susceptibility at Δ detuning. Substituting into Eq. 2.35 and 2.36 and collecting terms, we get

$$\bar{a}_{out,1} = (1 + \kappa_1\chi_{sr}^{\Delta}[0])\bar{a}_{in,1} \tag{2.39}$$

$$\bar{a}_{out,2} = \sqrt{\kappa_1\kappa_2}\chi_{sr}^{\Delta}[0]\bar{a}_{in,1} \tag{2.40}$$

$$\hat{\mathcal{A}}_q[\omega] = \hat{\zeta}_q[\omega] + \sqrt{\kappa_q}\chi_{sr}^{\Delta}[\omega] \sum_{j=1,2,I}\sqrt{\kappa_j}\hat{\zeta}_j[\omega] \quad , q = 1, 2, I \tag{2.41}$$

Firstly we consider the classical equations Eq. 2.37, 2.39, 2.40, to compute the average photon population inside the cavity, $\bar{n}_p = |\bar{a}|^2$. This is given by

$$\bar{n}_p = \frac{\kappa_1}{\Delta^2 + (\kappa/2)^2}\frac{P_{in,1}}{\hbar\omega_d} = \frac{\kappa_1}{\Delta^2 + (\kappa_1 - \kappa/2)^2}\frac{P_{out,1}}{\hbar\omega_d} = \frac{1}{\kappa_2}\frac{P_{out,2}}{\hbar\omega_d} \tag{2.42}$$

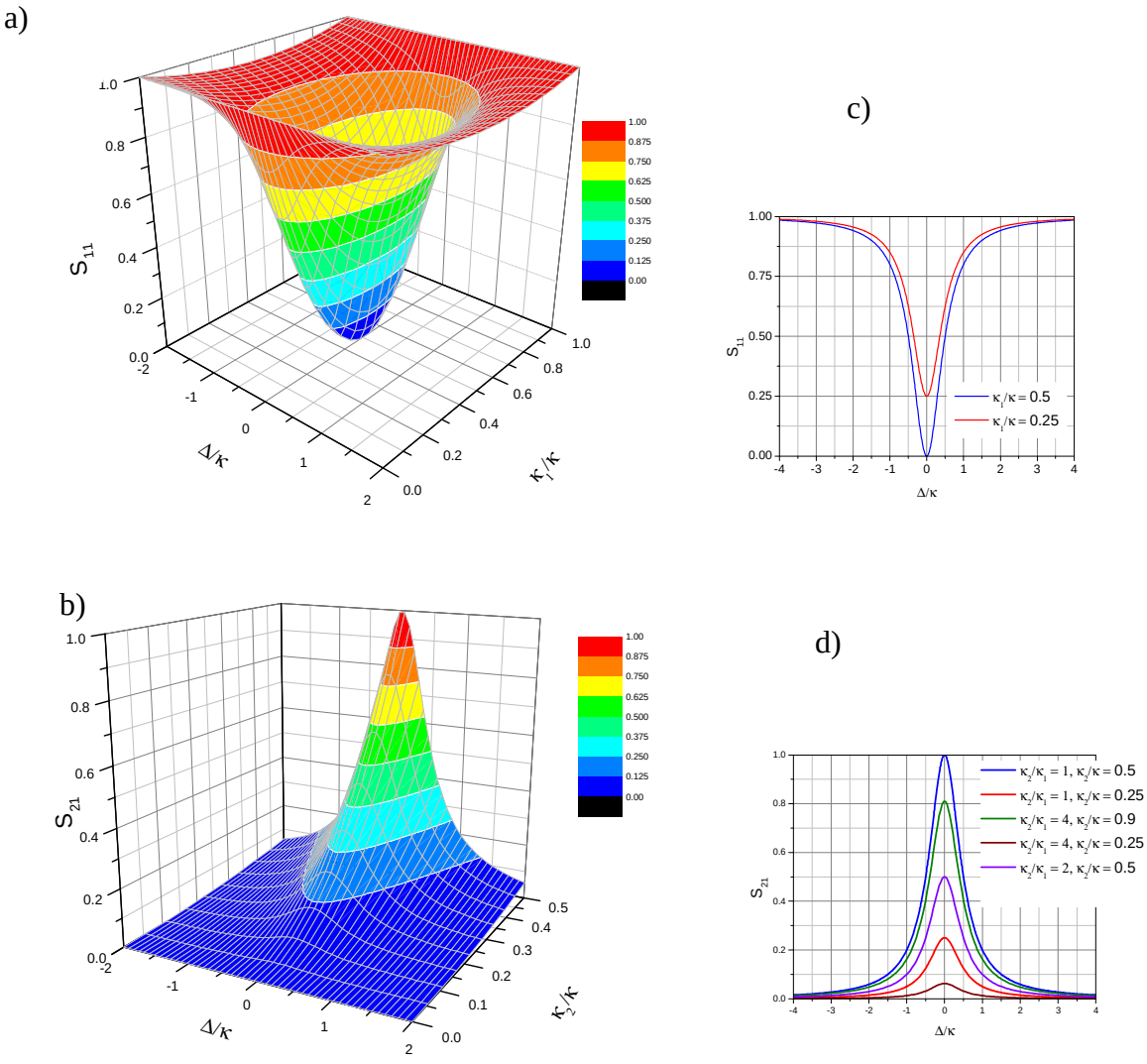

Figure 2.3 3D surface plots of a) the reflection coefficient, S_{11}, and b) the transmission coefficient S_{21}. 2D slices of c) S_{11} and d) S_{21} for various values of κ_1 and κ_2.

where $P_{in,1} = \hbar\omega_d\left|\bar{a}_{in,1}\right|^2$, $P_{out,1} = \hbar\omega_d\left|\bar{a}_{out,1}\right|^2$, $P_{out,2} = \hbar\omega_d\left|\bar{a}_{out,2}\right|^2$ are the average input power at port 1, the average output power at port 1 and 2 respectively. We can thus read off the magnitude of the reflection coefficient, S_{11}, and the transmission coefficient, S_{21}, to be

$$S_{11}(\Delta, \kappa_1, \kappa) = \frac{P_{out,1}}{P_{in,1}} = \frac{\Delta^2 + (\kappa_1 - \kappa/2)^2}{\Delta^2 + (\kappa/2)^2} \tag{2.43}$$

$$S_{21}(\Delta, \kappa_1, \kappa_2, \kappa) = \frac{P_{out,2}}{P_{in,1}} = \frac{\kappa_1\kappa_2}{\Delta^2 + (\kappa/2)^2} \tag{2.44}$$

Thus in principle, we get maximum coupling of the input field into the two-sided cavity at $\kappa_1 = \kappa_2$ and zero detuning for a high internal Q cavity. As shown in Figure 2.3, the transmission is highest for zero detuning for any combination of κ_1 and κ_2. We can in principle achieve a 100% transmission at zero detuning and $\kappa_1 = \kappa_2 = \kappa/2$. Notice that we can improve the signal to noise ratio at port 2 by making $\kappa_2 > \kappa_1$. This is because the photons in the cavity have a higher chance of leaking out of the more dissipative port, port 2. The main caveat with the unbalanced cavity is that you need to pump harder to get the same number of pump quanta in the cavity. Also worth mentioning is the fact that the transmission of the unbalanced case is always less than 100% from Eq 2.44.

We now turn our attention to the thermal noise inside the cavity resulting from the quantum noise input from the ports. The cavity will become populated due to noise entering the dissipative ports. Thermal noise entering the ports is reflected in the correlation functions given in time domain by (see references [18-32])

$$\langle\hat{\zeta}_j^\dagger(t)\hat{\zeta}_j(t')\rangle = \bar{n}_j^T\delta(t - t') \tag{2.45a}$$

$$\langle\hat{\zeta}_j(t)\hat{\zeta}_j^\dagger(t')\rangle = \left(\bar{n}_j^T + 1\right)\delta(t - t'), \quad j = 1, 2, I \tag{2.45b}$$

Using Eq. 2.21 we can write Eq. 2.45 in frequency space as

$$\langle \hat{\zeta}_j^{\dagger}[\omega]\hat{\zeta}_j[\omega']\rangle = \bar{n}_j^T 2\pi\delta(\omega+\omega') \tag{2.46a}$$

$$\langle \hat{\zeta}_j[\omega]\hat{\zeta}_j^{\dagger}[\omega']\rangle = \left(\bar{n}_j^T+1\right)2\pi\delta(\omega+\omega'), \quad j=1,2,I \tag{2.46b}$$

Here, $\bar{n}_j^T$ is the number of thermal quanta provided by the dissipative bath j, which accounts for the presence of thermal noise in the cavity. Microwave experiments use voltage amplifiers and hence the output spectrum measured is the symmetric-in-frequency noise spectrum [18, 29], $\bar{S}_{\hat{\mathcal{A}}_q}[\omega]$, for $q = 1,2,I$. This is given by

$$\bar{S}_{\hat{\mathcal{A}}_q}[\omega] \equiv \frac{1}{2}\int_{-\infty}^{+\infty}\langle\{\hat{\mathcal{A}}_q(t),\hat{\mathcal{A}}_q^{\dagger}(0)\}\rangle e^{i\omega t}dt = \frac{1}{2}\int_{-\infty}^{+\infty}\langle\{\hat{\mathcal{A}}_q[\omega],\hat{\mathcal{A}}_q^{\dagger}[\omega']\}\rangle\frac{d\omega'}{2\pi} \tag{2.47}$$

Eq. 2.47 can be simplified using Eq. 2.41 and 2.46 to get

$$\bar{S}_{\hat{\mathcal{A}}_q}[\omega] = \left(\bar{n}_q^T+\frac{1}{2}\right)+\kappa_q\left|\chi_{sr}^{\Delta}[\omega]\right|^2\kappa\left(\bar{n}_{sr}^T-\bar{n}_q^T\right) \tag{2.48}$$

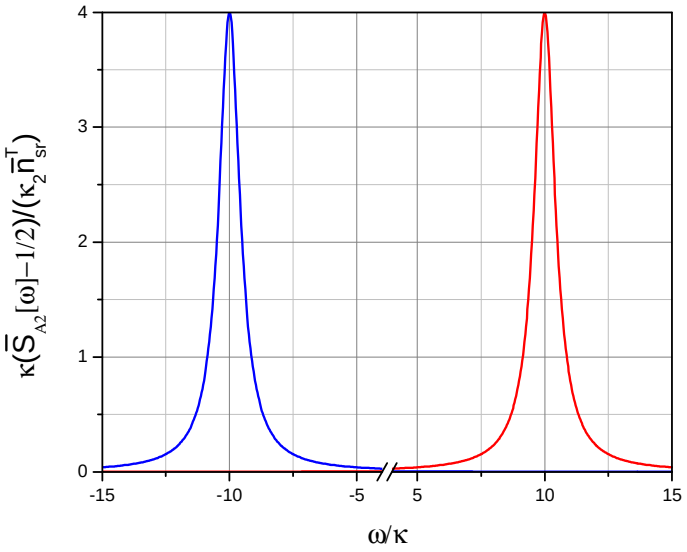

Figure 2.4 Plot of $\left(\bar{S}_{\hat{\mathcal{A}}_2}[\omega]-\frac{1}{2}\right)\kappa/(\kappa_2\bar{n}_{sr}^T)$ for $\Delta = +10\kappa$ (blue) and Δ = -10κ (red)

where $\bar{n}_{sr}^{T} = \frac{1}{\kappa}\sum_{j=1,2,I}\kappa_j \bar{n}_j^{T}$ is the thermal occupation of the cavity[§§]. In particular, using port 2 as the readout port and taking $\bar{n}_2^{T} = 0$ in the absence of any drive at this port, Eq. 2.48 takes the simple form

$$\bar{S}_{\hat{\mathcal{A}}_2}[\omega] = \frac{1}{2} + \kappa_2 \frac{\kappa}{(\omega+\Delta)^2 + \left(\frac{\kappa}{2}\right)^2}\bar{n}_{sr}^{T} \tag{2.48}$$

We see that the noise spectrum of the output field consists of a Lorentzian sitting on a white noise background representing the vacuum noise entering the cavity from port 2 (see Figure 2.4). The area under the Lorentzian above the white noise background is proportional to $\bar{n}_{sr}^{T}$, the cavity occupation and κ_2 the dissipation of port 2.

Having studied the quantum properties of the SR, we extend the formalism to include an NR coupled capacitatively to the SR.

2.2 I/O Formulation for Nanoresonator Coupled to a Microwave Resonator

The theory derived in section 2.1 above can be extended to incorporate the interaction between the SR and a NR. The NR is coupled capacitatively to the SR through nanofabrication with a gap separation usually as small as a few tens of nanometers. By applying a red detuned signal to the NR-SR system, it is possible to dynamically cool the NR by backaction. The red signal scatters quanta off the NR according to the anti-Stokes Raman scattering process and hence cools the NR. Driving the cavity at a blue frequency causes the NR to gain quanta and heat up in the Stokes process. By combining a strong red and a weak blue drive such that the resulting sidebands are separated, it is in principle possible to measure an additional quantum in the blue sideband compared to the red. The backaction effects can be

[§§] In the resolved sideband limit, we treat phase noise and thermal noise as equilavent.

evaded if the drive signals of the double pump configuration are of equal strength and the sidebands are overlapped. The quantum mechanical theory of cavity assisted backaction cooling has been described for the case where thermal occupation of the SR is negligible [11,13,14,18]. In practice, cavity occupation plays a very important role in determining the coldest temperature of the NR. In this section we will briefly revise the cooling theory and extend the discussion using the quantum noise approach to include the noise from the SR. We shall derive an equivalent expression for the NR heating due to the blue drive. Lastly we shall consider the double pump drive when the sidebands are separated and also discuss the situation when the sidebands are overlapped. In the discussion that follows, we will assume the resolved sideband limit where the NR frequency is far greater than the SR damping. We have moved the mathematical derivations of the key expressions to Appendix A to avoid crowding the physics that we want to explore.

2.2.1 NR-SR System Hamiltonian

Suppose the NR has resonance frequency ω_m, effective mass m, intrinsic linewidth γ_m, and is coupled to the SR of section 2.1 as shown in Figure 2.5 via a variable capacitance, $C_{NR}(x) \approx C_{NR}^0 - [\partial_x C_{NR}(0)]x$. Where C_{NR}^0 is the equilibrium capacitance, x is the displacement from equilibrium and $[\partial_x C_{NR}(0)] > 0$ is the capacitative coupling constant of the NR-SR system. Notice that, the capacitative coupling constant strongly depends on the equilibrium gap separation, d, between the NR and the gate of the SR; the narrower the gap, the smaller the capacitive coupling. For instance using a parallel plate capacitor to model this coupling, we can estimate, $[\partial_x C_{NR}(0)] = C_{NR}^0/d$, with $C_{NR}^0 \sim 1/d$. Compared to the SR system, the coupled NR-SR system now has a bare resonance frequency of $\omega_{sr} = 1/\sqrt{LC_\Sigma}$ where the total

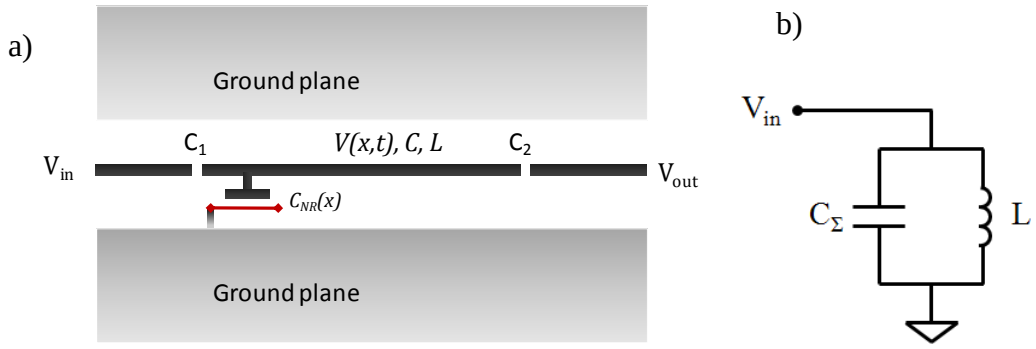

Figure 2.5 Layout and equivalent circuit of the NR-SR device.

capacitance $C_\Sigma = C_o + C_{NR}^0$. The electrostatic energy is then given by $E_C = \mathrm{Q}^2/2(\mathrm{C}_\Sigma - [\partial_x C_{NR}(0)]x)$ where Q is the equivalent charge on C_Σ. Similarly $E_L = \Phi^2/2\mathrm{L}$ is the magnetic energy where Φ is the flux through the inductor L. Consider in addition that the cavity is driven at frequencies, ω_n, *n=1,2*, with an electric potential of the form $V(t) = \sum_{n=1}^{2} 2\sqrt{2\hbar\omega_{sr}L}\mathcal{E}_n\left(e^{i\omega_n t} + c.c\right)$ where $\mathcal{E}_\mathrm{n}^2$ is proportional to the input power and will be determined more precisely in the next section (See Appendix A.1.1). Finally we shall assume for the remainder of the calculation that we are in the resolved sideband limit wherein the mechanical frequency is much larger than the SR linewidth, $\omega_m \gg \kappa$. The NR-SR system can thus be described according to the classical Hamiltonian given by [30]

$$H = \frac{\Phi^2}{2\mathrm{L}} + \frac{\mathrm{Q}^2}{2\mathrm{C}_\Sigma} + \frac{p^2}{2m} + \frac{1}{2}m\omega_m^2 x^2 + \frac{\mathrm{Q}^2}{2\mathrm{C}_\Sigma^2}[\partial_x C_{NR}(0)]x + \frac{1}{2}V(t)Q \qquad (2.49)$$

where x, p are the canonical position and momentum of the NR and Q, Φ are the canonical charge and flux of the SR. This Hamiltonian can be quantized by setting $[\hat{x}, \hat{p}] = i\hbar$ and $\left[\hat{Q}, \hat{\Phi}\right] = i\hbar$ for the NR and SR. From Eq. 2.49, we can immediately write the SR and NR lowering operators as

$$\hat{a} = \frac{1}{\sqrt{2\hbar}}\left[\sqrt{\omega_{sr}L}\hat{Q} + i\frac{1}{\sqrt{\omega_{sr}L}}\hat{\Phi}\right] \tag{2.50}$$

$$\hat{c} = \frac{1}{\sqrt{2\hbar}}\left[\sqrt{m\omega_m}\hat{x} + i\frac{1}{\sqrt{m\omega_m}}\hat{\mathrm{p}}\right] \tag{2.51}$$

Thus the Hamiltonian of the NR-SR system in the Schrodinger picture is given by

$$H_S = \hbar\omega_{sr}\left(\hat{a}^\dagger\hat{a} + \frac{1}{2}\right) + \hbar\omega_m\left(\hat{c}^\dagger\hat{c} + \frac{1}{2}\right) + \frac{1}{2}\hbar g x_{zpf}(\hat{c} + \hat{c}^\dagger)(\hat{a} + \hat{a}^\dagger)^2 + \sum_{n=1}^{2}\hbar\left(\mathcal{E}_n^* e^{i\omega_n t} + c.c\right)(\hat{a} + \hat{a}^\dagger) \tag{2.52}$$

Where $x_{zpf} = \sqrt{(\hbar/2m\omega_m)}$ is the zero point fluctuation and $g = \partial_x\omega_{sr} = \frac{1}{2}(\omega_{sr}/C_\Sigma)[\partial_x C_{NR}(0)]$ is the coupling strength. Using $H_0 = \hbar\omega_{sr}\left(\hat{a}^\dagger\hat{a} + \frac{1}{2}\right) + \hbar\omega_m\left(\hat{c}^\dagger\hat{c} + \frac{1}{2}\right)$ as the bare Hamiltonian, the interaction Hamiltonian after using the rotating wave approximation takes the form

$$H_I = \hbar g x_{zpf}\left(\hat{c}e^{-i\omega_m t} + h.c\right)\hat{a}^\dagger\hat{a} + \sum_{n=1}^{2}\hbar\left(\mathcal{E}_n^* e^{-i\Delta_n t}\hat{a} + h.c\right) \tag{2.53}$$

where $\Delta_n = \omega_{sr} - \omega_n$ is the detuning. The Heisenberg equations of motion for the SR and NR operators and the conservative equation are given by

$$\partial_t\hat{a}(t) = -igx_{zpf}\left[\hat{c}(t)e^{-i\omega_m t} + h.c\right]\hat{a}(t) - i\sum_{n=1}^{2}\mathcal{E}_n e^{i\Delta_n t} - \frac{\kappa}{2}\hat{a}(t) - \sqrt{\kappa}\hat{a}_{in}(t) \tag{2.54a}$$

$$\partial_t\hat{c}(t) = -igx_{zpf}\hat{a}^\dagger(t)\hat{a}(t)e^{i\omega_m t} - \frac{\gamma_m}{2}\hat{c}(t) - \sqrt{\gamma_m}\hat{c}_{in}(t) \tag{2.54b}$$

$$\hat{a}_{out}(t) = \hat{a}_{in}(t) + \sqrt{\kappa}\hat{a} \tag{2.54c}$$

where $\hat{a}_{in}$ is the total input noise associated with the SR damping and similarly $\hat{c}_{in}$ represents the total noise associated with the intrinsic NR damping. In the remainder of this chapter, we aim to solve Eq. 2.54 for various pump configurations.

2.2.2 Single Pump Drive

2.2.2.1 Single Red Drive: Backaction Cooling

Firstly we consider the situation where the NR-SR is driven by a single red drive with $\mathcal{E}_2 = 0$ in Eq. 2.54 a). The pump configuration is shown in Figure 2.6 a) where a single red drive mixes with the NR fluctuations to produce a sideband detuned by δ_R from the SR resonance. The single red drive leads to backaction cooling of the NR according to the anti-Stokes Raman scattering process as shown in Figure 2.6 b) and c). The incident photon, supplied by the red detuned microwave drive, absorbs a phonon from the NR in the anti-Stokes scattering process. This leads to a reduction in the phonon occupation of the NR which is equivalent to saying that the NR becomes colder. This cooling process is in competition with the finite heating from the bath (resulting from the intrinsic damping) of the NR and also the backaction heating from the SR noise. We have considered these effects in the derivations of Appendix A.1.1 where we have simplified Eq. 2.54 for the single red drive and solved for the lowering operators of the coupled NR-SR system. This leads naturally to a detailed balanced expression for the average phonon occupation of the NR.

Mechanical Occupation for the Single Red Drive

Using the expression for the lowering operator of the NR given by Eq. A.4 b' of Appendix 1.1, we can write the position spectrum of the NR for the single red drive as

$$S_{xx}[\omega] = \int_{-\infty}^{+\infty} \langle x[\omega]x[\omega'] \rangle \frac{d\omega'}{2\pi}$$
$$= x_{zpf}^2 |\chi_m^r[\omega]|^2 \left[\gamma_m(2\bar{n}_m^T + 1) + |\alpha_R|^2 |\chi_{sr}^r[\omega]|^2 \kappa\left(2\bar{n}_{sr,R}^T + 1\right)\right] \quad (2.55)$$

In Eq. 2.55, $\bar{n}_m^T$ is the number of thermal quanta in the intrinsic bath coupled to the

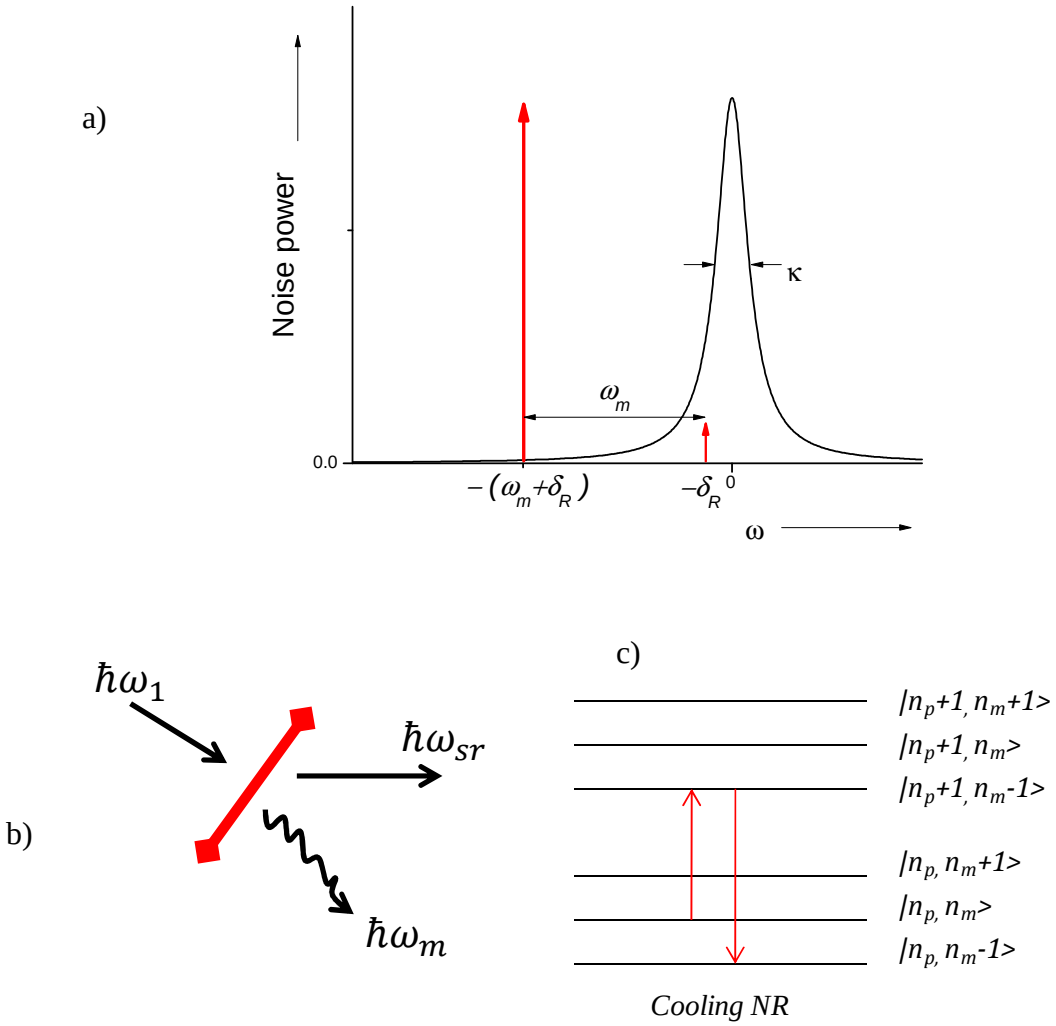

Figure 2.6 a) Schematic diagram showing the pump configuration of the single red drive (in a frame rotating at ω_{sr}). The red pump drive is such that the resulting sideband is detuned by δ_R from the microwave resonance. b) Illustration of the anti-Stoke Raman scattering where the red pump up-converts a phonon to a photon thereby cooling the mechanics in the process. c) Detailed diagram of the anti-Stoke scattering process. The red pump excites the NR-SR system from $|n_p, n_m>$ to a state with one less phonon and one more photon, $|n_p+1, n_m-1>$. This excited state readily decays to $|n_p, n_m-1>$ leaving the NR in a colder state.

NR, $\alpha_R = g x_{xpf}\sqrt{\bar{n}_p}$ is the effective coupling strength, $\chi_{sr}^{r}[\omega] = 1/\left[i(\omega - \delta_R) - \frac{\kappa}{2}\right]$ is the cavity susceptibility for the red sideband and $\bar{n}_{sr,R}^{T}$ is the effective backaction occupancy of the cavity associated with the red pump. In the good cavity limit, this backaction occupancy is approximately equal to the thermal occupation of the SR. For a high-Q NR coupled to a high-Q SR and for the resolved sideband limit ($\gamma_m \ll \kappa \ll \omega_m$), the effective mechanical susceptibility is

$$\chi_m^r[\omega] \approx \frac{1}{i(\omega + \delta\omega_m^R) - \frac{1}{2}\left(\gamma_m + \Gamma_{\mathrm{R}}(\delta_{\mathrm{R}})\right)} \tag{2.56}$$

where $\Gamma_R(\delta_R) = 4\frac{|\alpha_R|^2}{\kappa}\frac{1}{\left[1+\left(\frac{2\delta_R}{\kappa}\right)^2\right]}$ is the optomechanical scattering rate due to the red source and $\delta\omega_m^R = \Gamma_R(\delta_R)\frac{\delta_R}{\kappa}$ is the optical frequency shift. See Figure 2.7b) for a plot of the scattering rate and the frequency shift for the single red pump. Notice that optical scattering rate is directly proportional to $|\alpha_R|^2$, the square of the effective coupling constant and hence to the number of pump quanta, $\bar{n}_p$, in the SR. Integrating Eq. 2.55 and collecting terms leads to the detailed balanced expression for the mechanical occupation of the NR given by

$$\bar{n}_m = \frac{\gamma_m \bar{n}_m^T + \Gamma_R(\delta_R)\bar{n}_{sr,R}^T}{\gamma_m + \Gamma_R(\delta_R)} \tag{2.57}$$

Figure 2.7 a) captures this detailed balance between the SR, the NR and the bath; the steady-state phonon number on the NR is the weighted mean of the thermal and optomechanical phonon numbers. We see from Eq. 2.57 that by optimizing the optical scattering rate to exceed the intrinsic damping of the NR and at the same time minimizing the bath quanta, we can in principle cool the NR mode to its motional ground state in the absence of cavity occupation. Basically, the thermal occupation of

Figure 2.7 a) Detailed balance showing the SR and bath coupling to the NR. $\Gamma_{SR} = \Gamma_R, \Gamma_B, \Gamma_R - \Gamma_B$ for the single red, single blue, double pump drives. For the single red case, the NR-SR system eventually decouples from the bath when $\Gamma_R \gg \gamma_m$ leading to NR cooling. The single blue drive on the other hand heats the NR above the bath temperature. b) Plot of frequency shift of the NR frequency and scattering rate versus detuning of the red pump. c) Linewidth broadening and cooling plot of the NR with $\gamma_m = 2\pi\ 15Hz$ and $\bar{n}_m^T = 500$. The final occupation of the NR depends on the occupation of the cavity. The presence of 2 quanta in the cavity impedes further cooling of the NR as shown by the blue curve.

a)

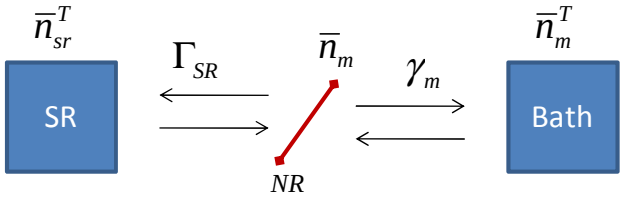
$\bar{n}_{sr}^{T}$
Γ_{SR}
$\bar{n}_{m}$
γ_{m}
$\bar{n}_{m}^{T}$
SR
Bath
NR

b)

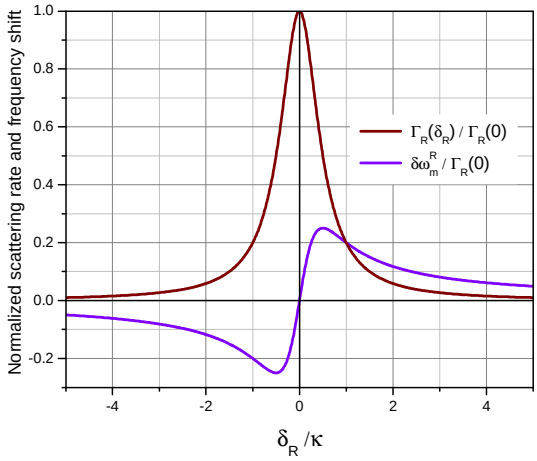
Normalized scattering rate and frequency shift
$\Gamma_R(\delta_R) / \Gamma_R(0)$
$\delta\omega_m^R / \Gamma_R(0)$
δ_R / κ

c)

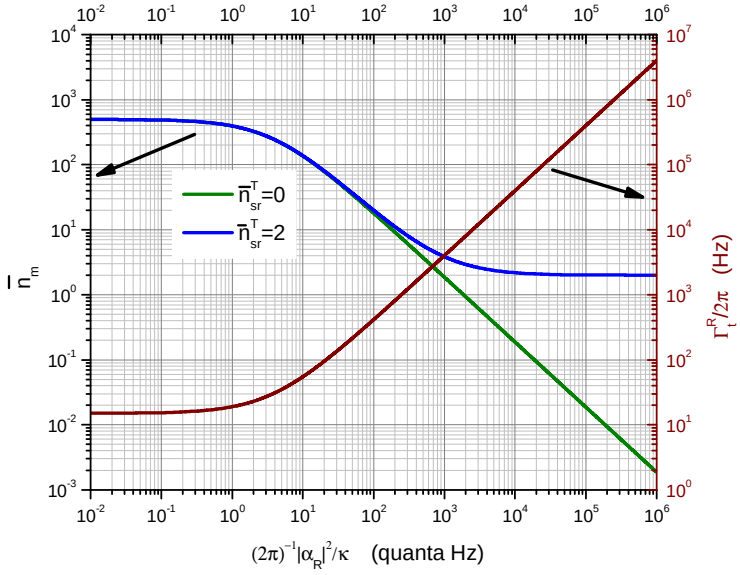
$\bar{n}_{sr}^{T}$=0
$\bar{n}_{sr}^{T}$=2
$\bar{n}_m$
$\Gamma_t^R/2\pi$ (Hz)
$(2\pi)^{-1}|\alpha_R|^2/\kappa$ (quanta Hz)

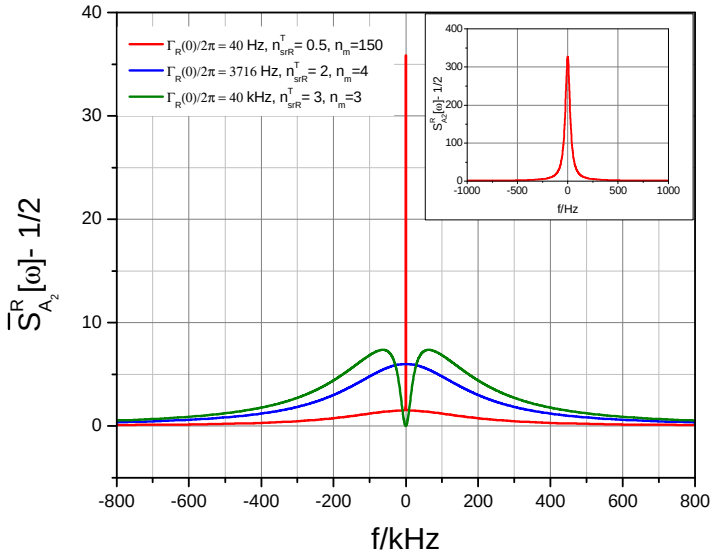

Figure 2.8 Widespan power spectrum of the red sideband tune at microwave resonance ($\delta_R = 0$), for $\kappa = 2\pi\ 400\ kHz$, $\kappa_2 = 0.75\kappa$, $\gamma_m = 2\pi\ 15 Hz$ and for various coupling strength and cavity occupation. At low pump coupling (red curve), the sideband is a lorentzian peak on the cavity background (see inset also). This peak levels off as we increase the pump strength (blue curve) and eventually becomes a dip at higher pump strength (green curve). The optical shifts were ignored when making these plots

the cavity sets the lowest number of quanta achievable. Figure 2.7 c) shows a typical linewidth broadening and cooling curve for an NR-SR system with zero and two quanta in the SR.

Output Spectrum for the Single Red Drive

We now turn our attention to the output spectrum from the single red drive at port 1 (with no drive at port 2). From Appendix 1.2, the symmetric-in-frequency noise spectrum, $\bar{S}^R_{\hat{\mathcal{A}}_2}$, associated with the output microwave field, $\hat{\mathcal{A}}_2$, leaving port 2, is given by

$$\bar{S}^R_{\hat{\mathcal{A}}_2}[\omega] \approx \frac{1}{2} + \kappa_2 \frac{\kappa}{\omega^2 + \left(\frac{\kappa}{2}\right)^2} \bar{n}^T_{sr,R} + \frac{\kappa_2}{\kappa} \frac{\Gamma_R(\delta_R)\Gamma_t^R}{(\omega + \delta_R)^2 + \left(\frac{\Gamma_t^R}{2}\right)^2} \bar{n}^R_{eff}[\omega, \delta_R] \tag{2.58}$$

Where the effective quanta measured in the red sideband is given by

$$\bar{n}^R_{eff}[\omega, \delta_R] = \bar{n}_m - 2\bar{n}^T_{sr,R}\left[cos^2\varphi_{\mathrm{R}} + \tfrac{1}{\Gamma_t^R}(\omega + \delta_R) sin2\varphi_{\mathrm{R}}\right] \tag{2.59}$$

with $tan\varphi_{\mathrm{R}} = 2\delta_R/\kappa$. Notice that due to the fact that the red sideband is detuned from the SR frequency, the backaction between the SR and the NR develops a phase difference, φ_{R}, and this distorts the shape of the Lorentzian spectrum. In the special case of perfect detuning where $\delta_R = 0$, Eq. 2.58 reduces to

$$\bar{S}^R_{\hat{\mathcal{A}}_2}[\omega] \approx \frac{1}{2} + \kappa_2 \frac{\kappa}{\omega^2 + \left(\frac{\kappa}{2}\right)^2} \bar{n}^T_{sr,R} + \frac{\kappa_2}{\kappa} \frac{\Gamma_R(0)\Gamma_t^R}{\omega^2 + \left(\frac{\Gamma_t^R}{2}\right)^2} \bar{n}^R_{eff}[\omega, 0] \tag{2.60}$$

where $\bar{n}^R_{eff}[\omega, 0] = \bar{n}_m - 2\bar{n}^T_{sr,R}$. We see that the cavity occupancy suppresses the measured quanta. This causes the mechanical sideband to change from a lorentzian peak to a dip as the cavity occupation increases. See Figure 2.8 which shows the output noise spectrum for a series of red coupling strengths and SR occupation.

2.2.2.2 Single Blue Drive: Backaction Heating, Negative Temperature

The mechanical occupation and output spectrum for a single blue drive can be similarly computed by using the same procedure of section 2.2.2.1 above. We sketch the derivation in Appendix 2.1 for $\mathcal{E}_1 = 0$ in Eq. 2.54a. Figure 2.9 a) shows a schematic sketch of the pump configuration where the blue drive creates a mechanical sideband at δ_B relative to the SR frequency. The single blue drive leads to backaction heating according to the Stokes Raman scattering process as shown in Figure 2.9 b) and c). The photon from the detuned blue drive adds an additional phonon to the NR. In addition to the optomechanical backaction heating, the finite heating from the intrinsic dissipation of the NR and the backaction heating from the cavity noise leads to an overall heating above the intrinsic thermal occupation of the bath.

Mechanical Occupation for the Single Blue Drive

From Appendix A.2.1, the position spectrum of the NR for the single blue drive is given from Eq. A.12b' by

$$S_{xx}[\omega] = \int_{-\infty}^{+\infty} \langle x[\omega]x[\omega']\rangle \frac{d\omega'}{2\pi}$$
$$= x_{zpf}^2 |\chi_m^b[\omega]|^2 \left[\gamma_m(2\bar{n}_m^T + 1) + |\alpha_B|^2 |\bar{\chi}_{sr}^b[\omega]|^2 \kappa\left(2\bar{n}_{sr,B}^T + 1\right)\right] \quad (2.61)$$

where $\alpha_B = g x_{xpf}\sqrt{\bar{n}_p}$ is the effective coupling strength, $\chi_{sr}^b[\omega] = \bar{\chi}_{sr}^{b\,*}[-\omega]$

$= 1/\left[i(\omega + \delta_B) - \frac{\kappa}{2}\right]$ is the susceptibility of the blue sideband. For the good cavity limit, $\bar{n}_{sr,B}^T$ in Eq. 2.61 is the effective backaction occupancy or equivalently the thermal occupation of the cavity due to the blue pump. In the relevant coupling limit, $\gamma_m \ll \kappa \ll \omega_m$, the effective susceptibility of the NR is given by

$$\chi_m^b[\omega] \approx \frac{1}{i(\omega + \delta\omega_m^B) - \frac{1}{2}\left(\gamma_m - \Gamma_{\mathrm{B}}(\delta_{\mathrm{B}})\right)} \quad (2.62)$$

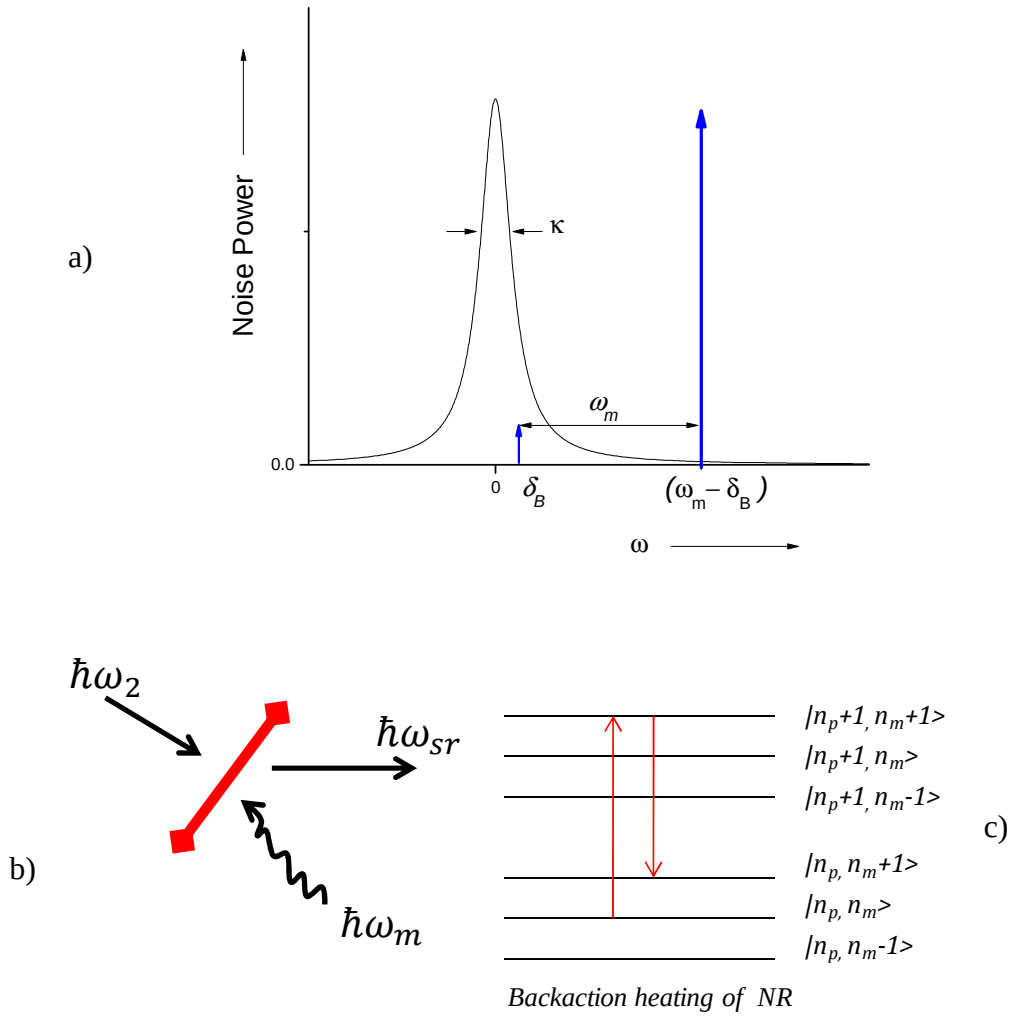

Figure 2.9 a) Pump configuration for the single blue drive with sideband detuned by δ_B. b) Sketch of Stoke Raman process where the blue drive down-converts a photon to a phonon in the backaction heating of the NR. c) Detailed diagram of the Stokes Raman scattering process. The blue pump excites the NR-SR system from $|n_p, n_m>$ to $|n_p + 1, n_m + 1>$. This excited state then decays to $|n_p, n_m + 1>$ which has one extra NR quantum than the initial state.

a)

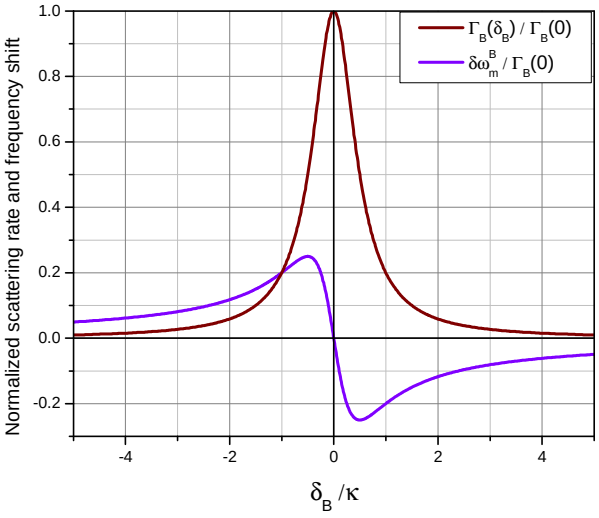

b)

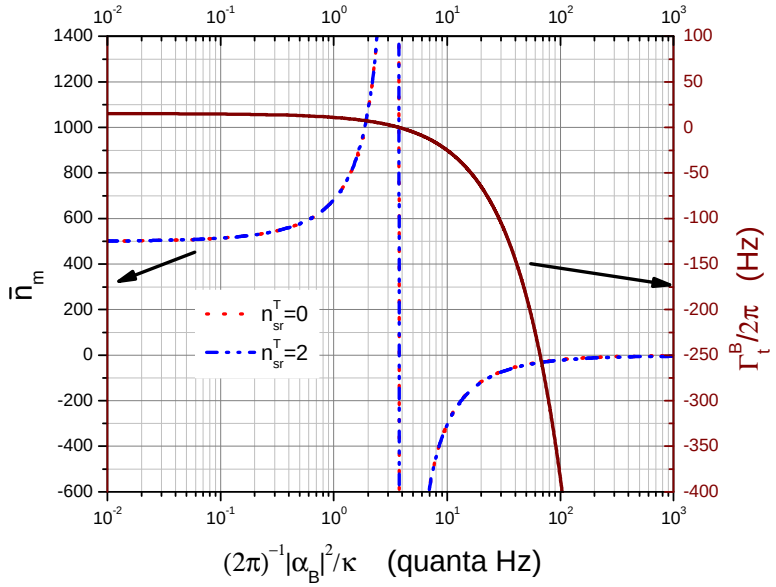

Figure 2.10 a) Plot of NR frequency shift and scattering rate versus detuning of the blue pump. b) Linewidth narrowing and backaction heating plot of the NR for $\gamma_m = 2\pi\ 15Hz$ and $\bar{n}_m^T = 500$. The NR heats up above the bath temperature and goes unstable when $\Gamma_t^B = 0$. Beyond this point, the NR is in the negative temperature regime.

where $\Gamma_B(\delta_B) = 4\frac{|\alpha_B|^2}{\kappa}\frac{1}{\left[1+\left(\frac{2\delta_B}{\kappa}\right)^2\right]}$ is the optical scattering rate due to the blue source and $\delta\omega_m^B = -\Gamma_B(\delta_B)\frac{\delta_B}{\kappa}$ is the optical frequency shift. The optomechanical scattering rate and frequency shift are plotted as shown in Figure 2.10 a). Integrating Eq. 2.61 and collecting terms leads to the detailed balanced expression for the mechanical occupation of the NR given by (see Figure 2.7 (a))

$$\bar{n}_m + 1 = \frac{\gamma_m(\bar{n}_m^T + 1) + \Gamma_B(\delta_B)\bar{n}_{sr,B}^T}{\gamma_m - \Gamma_B(\delta_B)} \tag{2.63}$$

Thus, applying a single blue pump leads to linewidth narrowing as the net scattering rate, $\Gamma_t^B = \gamma_m - \Gamma_B(\delta_B)$ is always smaller than the intrinsic dissipation of the NR. One can thus in principle heat up the NR above the bath temperature by driving at the blue frequency. We expect the NR to eventually become unstable when $\Gamma_B(\delta_B) \sim \gamma_m$. Increasing $\Gamma_B(\delta_B)$ further beyond this point will lead to a NR in the negative temperature regime. Figure 2.10 b) is a plot of the line width narrowing for the single blue pump. The NR is heated above the bath temperature to an unstable equilibrium temperature before entering into the negative temperature regime.

Output Spectrum for the Single Blue Drive

In Appendix A.2.2, we compute the symmetric-in-frequency noise spectrum, $\bar{S}_{\hat{\mathcal{A}}_2}^B$, associated with the output microwave field, $\hat{\mathcal{A}}_2$, leaving port 2, for the single blue drive. With no drive at port 2 and using the weak coupling approximation, the output noise spectrum given by Eq. A.14 simplifies to

$$\bar{S}_{\hat{\mathcal{A}}_2}^B[\omega] \approx \frac{1}{2} + \kappa_2\frac{\kappa}{\omega^2 + \left(\frac{\kappa}{2}\right)^2}\bar{n}_{sr,B}^T + \frac{\kappa_2}{\kappa}\frac{\Gamma_B(\delta_B)\Gamma_t^B}{(\omega - \delta_B)^2 + \left(\frac{\Gamma_t^B}{2}\right)^2}\bar{n}_{eff}^B[\omega, \delta_B] \tag{2.64}$$

Where the effective quanta measured in the blue sideband is given by

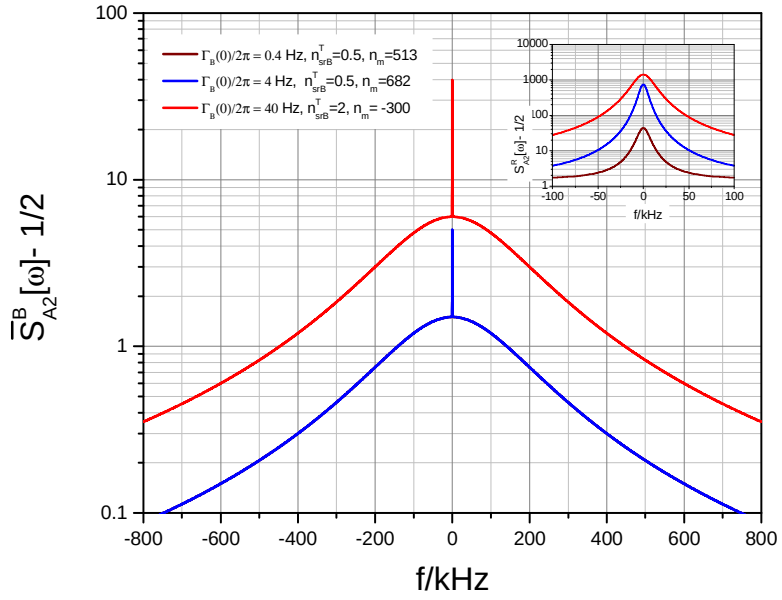

Figure 2.11 Output spectrum of the blue sideband for $\kappa = 2\pi\ 400\ kHz$, $\kappa_2 = 0.75\kappa$, $\gamma_m = 2\pi\ 15Hz$ and for various coupling strength and cavity occupation. For the blue drive, the sideband is always a lorentzian peak on the cavity noise background (see inset also).

$$\bar{n}^B_{eff}[\omega, \delta_B] = \bar{n}_m + 1 + 2\bar{n}^T_{sr,B}\left[cos^2\varphi_B - \frac{1}{\Gamma^B_t}(\omega - \delta_B)sin2\varphi_B\right] \tag{2.65}$$

with $tan\varphi_B = 2\delta_B/\kappa$. For $\delta_B = 0$, Eq. 2.64 reduces to

$$\bar{S}^B_{\hat{A}_2}[\omega] \approx \frac{1}{2} + \kappa_2 \frac{\kappa}{\omega^2 + \left(\frac{\kappa}{2}\right)^2}\bar{n}^T_{sr,B} + \frac{\kappa_2}{\kappa}\frac{\Gamma_B(0)\Gamma^B_t}{\omega^2 + \left(\frac{\Gamma^B_t}{2}\right)^2}\bar{n}^B_{eff}[\omega, 0] \tag{2.66}$$

where $\bar{n}^B_{eff}[\omega, 0] = \bar{n}_m + 1 + 2\bar{n}^T_{sr,B}$ is the observed number of quanta. Notice the extra factor of 1 in the observed quanta for the blue drive compared to the red drive case in the previous section. The cavity occupation for the blue drive always enhances the measured quanta and thus the blue sideband is always a lorentzian peak. Figure

2.11 shows series of output spectra for various blue coupling strengths and SR occupation.

2.2.3 Double Pump Drive

2.2.3.1 Double Pump Drive: Separated Sidebands

In this section, we consider the double pump configuration wherein the resulting red and blue sidebands are separated as shown in Figure 2.12. The derivation follows the same procedure of section 2.2.1.1 and 2.2.1.2 above, but we are careful to keep track of the double pump effect and modify the expressions as we go along. The expressions derived in this section hold true for any double pump strength in the relevant weak coupling limit especially the case where the blue drive is much weaker than the red. In this particular case, we are able to extract the $\bar{n}_m/(\bar{n}_m + 1)$ behavior where the

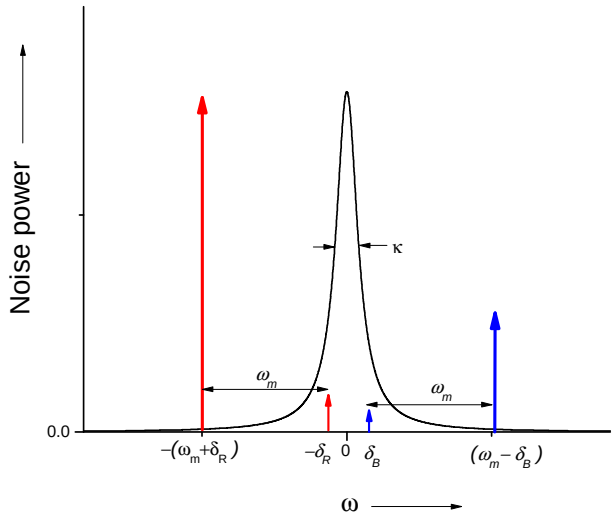

Figure 2.12 Double pump configuration for the separated sideband case

number of quanta associated with the blue sideband is one more than that associated with the red sideband. This is easily understood by considering the anti-Stokes and Stokes processes described above for the single red and single blue cases above. There will in principle be $\bar{n}_m$ quanta associated with the red sideband compared to $\bar{n}_m + 1$ for the blue sideband.

Mechanical Occupation for double pump drive with separated sidebands

We can immediately write the position spectrum of the NR from Appendix 3.1. as

$$S_{xx}[\omega] = x_{zpf}^2 |\chi_m^{br}|^2 \{\gamma_m(2\bar{n}_m^T + 1) + \Gamma_R(\delta_R)\big(2\bar{n}_{sr,R}^T + 1\big) + \Gamma_B(\delta_B)\big(2\bar{n}_{sr,B}^T + 1\big)\} \tag{2.67}$$

where the effective mechanical susceptibility is

$$\chi_m^{br}[\omega] \approx \frac{1}{i(\omega + \delta\omega_m^{BR}) - \frac{1}{2}\big(\gamma_m + \Gamma_R(\delta_R) - \Gamma_B(\delta_B)\big)} \tag{2.68}$$

in the relevant weak coupling limit. In Eq. 2.68, $\delta\omega_m^{BR} = \Gamma_R(\delta_R)\frac{\delta_R}{\kappa} - \Gamma_B(\delta_B)\frac{\delta_B}{\kappa}$ is the net frequency shift from the double pump drives. The corresponding detailed balance expression for the mechanical occupation of the NR is given by

$$\bar{n}_m = \frac{\gamma_m \bar{n}_m^T + \Gamma_{\mathrm{R}}(\delta_{\mathrm{R}})\bar{n}_{sr,R}^T + \Gamma_{\mathrm{B}}(\delta_{\mathrm{B}})\big(\bar{n}_{sr,B}^T + 1\big)}{\Gamma_{\mathrm{t}}} \tag{2.69}$$

where $\Gamma_{\mathrm{t}} = \gamma_m + \Gamma_{\mathrm{R}}(\delta_{\mathrm{R}}) - \Gamma_{\mathrm{B}}(\delta_{\mathrm{B}})$ is the net scattering rate. Notice that, for a single red pump, the mechanical occupation, $\bar{n}_m^R$, is given by $\bar{n}_m^R = \frac{1}{\gamma_m + \Gamma_{\mathrm{R}}(\delta_{\mathrm{R}})}\{\gamma_m \bar{n}_m^T + \Gamma_{\mathrm{R}}(\delta_{\mathrm{R}})\bar{n}_R^T\}$ and hence we can substitute this expression in Eq. 2.69 to write

$$\bar{n}_m + 1 = \frac{\Gamma_{\mathrm{t}}^{\mathrm{R}}(\bar{n}_m^R + 1) + \Gamma_{\mathrm{B}}(\delta_{\mathrm{B}})\bar{n}_{sr,B}^T}{\Gamma_{\mathrm{t}}^{\mathrm{R}} - \Gamma_{\mathrm{B}}(\delta_{\mathrm{B}})} \tag{2.70}$$

From Eq. 2.70, we see that we can equivalently treat the double pump case as if it was the single blue pump case with the NR coupled to a thermal bath containing $\bar{n}_m^R$

quanta having an effective dissipative rate of $\Gamma_t^R = \gamma_m + \Gamma_R(\delta_R)$. This follows immediately from Eq. 2.63 of section 2.2.2.2 for the single blue pump.

Output Spectrum for double pump drive with separated sidebands

Assuming there is no drive at the output port, and for the weak coupling regime, a few steps of algebra simplifies Eq. A.18 and A.19 of Appendix 3.2 to give the output spectrum of the red and blue sidebands respectively as

$$\bar{S}_{\hat{A}_2^r}[\omega] \approx \frac{1}{2} + \kappa_2 \frac{\kappa}{\omega^2 + \left(\frac{\kappa}{2}\right)^2} \bar{n}_{sr,R}^T + \frac{\kappa_2}{\kappa} \frac{\Gamma_R(\delta_R)\Gamma_t}{(\omega + \delta_R)^2 + \left(\frac{\Gamma_t}{2}\right)^2} \bar{n}_e^R[\omega, \delta_R] \tag{2.71}$$

$$\bar{S}_{\hat{A}_2^b}[\omega] \approx \frac{1}{2} + \kappa_2 \frac{\kappa}{\omega^2 + \left(\frac{\kappa}{2}\right)^2} \bar{n}_{sr,B}^T + \frac{\kappa_2}{\kappa} \frac{\Gamma_B(\delta_B)\Gamma_t}{(\omega - \delta_B)^2 + \left(\frac{\Gamma_t}{2}\right)^2} \bar{n}_e^B[\omega, \delta_B] \tag{2.72}$$

The effective quanta measured in the red and blue sidebands are respectively

$$\bar{n}_e^R[\omega, \delta_R] = \bar{n}_m - 2\bar{n}_{sr,R}^T \left[cos^2\varphi_R + \frac{1}{\Gamma_t}(\omega + \delta_R) sin2\varphi_R\right] \tag{2.73}$$

$$\bar{n}_e^B[\omega, \delta_B] = \bar{n}_m + 1 + 2\bar{n}_{sr,B}^T \left[cos^2\varphi_B - \frac{1}{\Gamma_t}(\omega - \delta_B) sin2\varphi_B\right] \tag{2.74}$$

As discussed above, the blue sideband has an extra quanta associated with it compared to the red. Notice also that because of the additional detuning (δ_R for red and δ_B for blue), the effective quanta have additional phase dependent terms given in Eq. 2.73 and 2.74. These will cause a distortion in the lorentzian shape of the mechanical sidebands. Figure 2.13 a) shows a plot of the red ($\delta_R = 0$) and blue ($\delta_B = 0.875\kappa$, $\kappa = 2\pi\ 400\ kHz$) sidebands resulting from pumping the NR-SR with an equivalent red drive of $\Gamma_R = 2\pi\ 10\ kHz$ and for various blue strengths $\Gamma_B(0)$. We use $\kappa_2 = 0.75\kappa$, $\bar{n}_m = 5$, $\bar{n}_{sr,R}^T = 3$ and $\bar{n}_{sr,B}^T = 0.5$ for all the plots. In Figure 2.13b) we plot only the blue sideband for similar conditions as in Figure 2.13 a). We compare the noise spectrum of the sideband for the case where we consider the backaction effects

a)

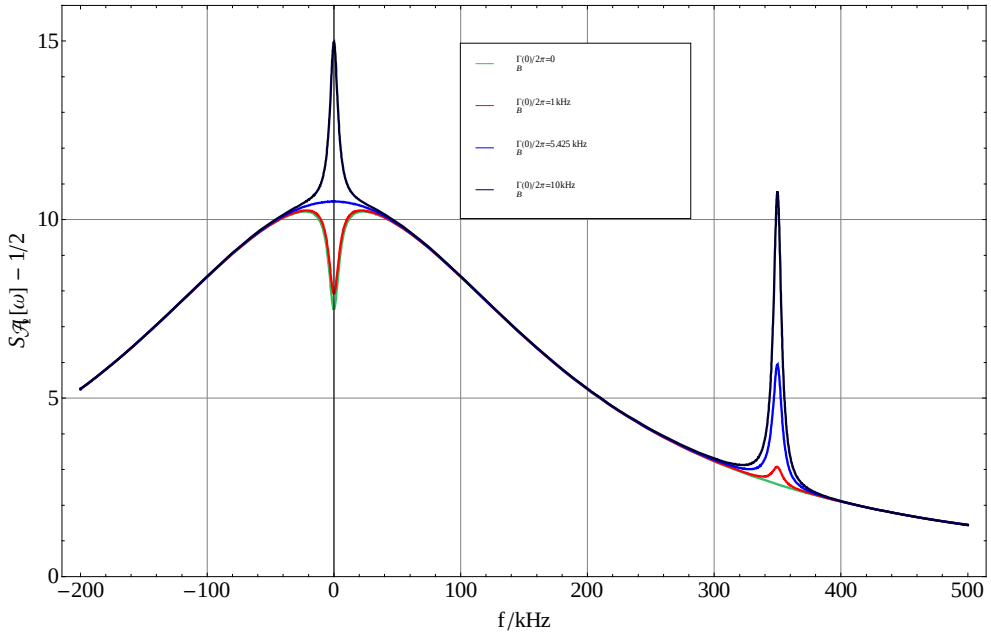

b)

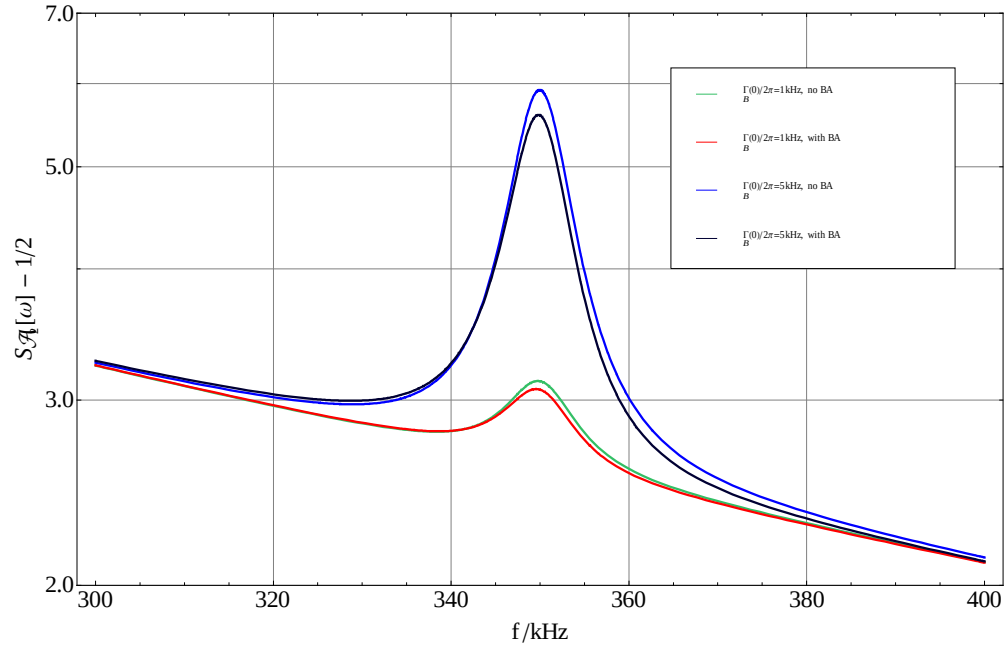

Figure 2.13 a) Output spectrum for separated sideband from double pump drive (see text for details), b) backaction (BA) at the blue sideband (see text for details).

resulting from detuning the blue to the case where we neglect the backaction effects. As hinted above, this effect causes a distortion in the lorentzian shape which becomes pronounced as we increase the strength of the blue drive.

2.2.3.2 Double Pump Drive: Overlapped Sidebands

Having considered the separated sideband case above, we briefly analyze the overlapped sideband configuration for completeness. For simplicity we look at the case where the red and blue pumps are of equal strength and the sideband resulting from the overlap is exactly on resonance with the SR as shown in Figure 2.14. In this configuration, it is in principle possible to evade the dyanmical backaction effects of the individual pumps (red cooling and blue heating). This leads to the squeezing of one of the quadratures of motion of the NR to possibly below the Standard Quantum Limit (SQL). This scheme has the key advantage that the backaction evasion (BAE) measurement is done in a Quantum Non-Demolition (QND) way as we describe below. Though we do not report measurement results for the double pump with overlapped sidebands in this dissertation, we provide theoretical expressions and sample design parameters that could be used to develop prototypical NR-SR devices for QND-BAE squeezing.

The quadratures of motion, $\hat{X}_1$ and $\hat{X}_2$, can be expressed in terms of the position operator and hence the lowering and raising operators of the NR as

$$\hat{x}(t) = \hat{X}_1(t)cos\omega_m t + \hat{X}_2(t)sin\omega_m t \tag{2.75}$$

where $\hat{X}_1(t) = x_{zpf}(c(t) + c^{\dagger}(t))$ and $\hat{X}_2(t) = -ix_{zpf}(c(t) - c^{\dagger}(t))$ in the Heisenberg picture. Notice that the quadratures are canonical conjugates, $\left[\hat{X}_1(t), \hat{X}_2(t)\right] = i2x_{zpf}^2$, with $\Delta\hat{X}_1\Delta\hat{X}_2 \geq x_{zpf}^2$. By considering the Heisenberg

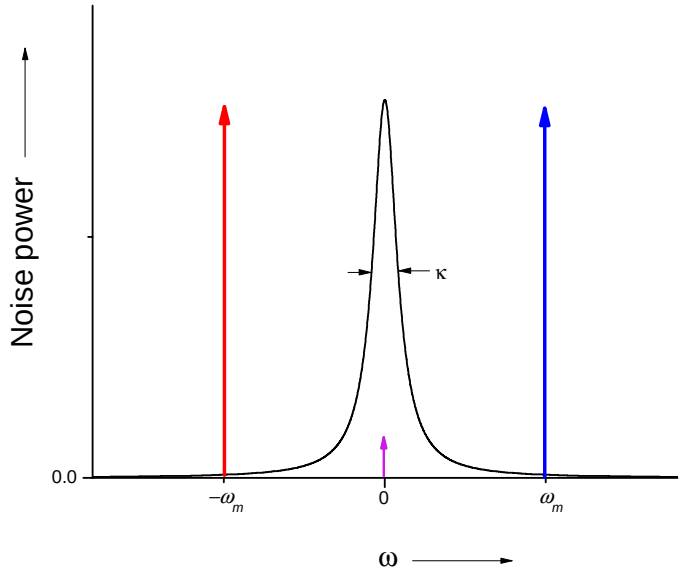

Figure 2.14 Double pump configuration for the overlapped sideband case.

equation of motion of the quadratures, we see that they are constants of motion with respect to H_o the bare Hamiltonian of the NR-SR system. If in addition, $\hat{X}_1$, commutes with the interaction Hamiltonian of our system, then we can in principle make QND measurements of $\hat{X}_1$ and squeeze this quadrature of motion. The overlapped sidebands configuration described in the beginning of this section naturally leads to such an interaction Hamiltonian. Below we adapt Clerk et al's [31] treatment to consider the QND-BAE measurement and squeezing of $\hat{X}_1$.

Position spectrum of Quadratures

From Appendix A.4.3, the position spectral densities of the quadratures are given by [31]

$$S_{X_1}[\omega] = x_{zpf}^2 |\chi_m[\omega]|^2 \gamma_m \{1 + 2(\bar{n}_m^T + \bar{n}_{bad})\} \qquad (2.76a)$$

$$S_{X_2}[\omega] = x_{zpf}^2 |\chi_m[\omega]|^2 \gamma_m \{1 + 2(\bar{n}_m^T + \bar{n}_{bad} + \bar{n}_{BA})\} \quad (2.76b)$$

where $\bar{n}_{BA} = 2\frac{\Gamma}{\gamma_m}(\bar{n}_{sr}^T + 1)$ is the effective backaction quanta heating the X_2 quadrature with $\Gamma = \Gamma_B(0) = \Gamma_R(0) = 4\,g^2 x_{zpf}^2 \bar{n}_p/\kappa$ the optomechanical strength of the individual pumps[***]. $\bar{n}_{bad} = \frac{\bar{n}_{BA}}{32}\left(\frac{\kappa}{\omega_m}\right)^2$ is the backaction heating associated with the bad cavity limit. We see from Eq. 2.76 *a*) that the X_1 quadrature is thus squeezed for the resolved sideband limit while X_2 is amplified by an extra $\bar{n}_{BA}$ quanta in Eq. 2.76 *b*).

Output Noise and Squeezing Below the SQL

The output spectrum of the microwave field leaving the SR can be computed in a similar fashion as in the separated sideband case above. This gives

$$\bar{S}_{\hat{A}_2}[\omega] = \frac{1}{2} + \kappa_2 \frac{\kappa}{\omega^2 + \left(\frac{\kappa}{2}\right)^2}\bar{n}_{sr}^T + \frac{\kappa_2}{\kappa}\frac{\gamma_m \Gamma}{\omega^2 + \left(\frac{\gamma_m}{2}\right)^2}(2\bar{n}_m^T + 1) \quad (2.77)$$

The amplifier on the output line of the measurement setup also adds noise to the measurements. Including this amplifier noise, we can write the spectrum of the measured quadrature, X_1, at the SR resonance as

$$S_{X_1,meas}[0] = 4\frac{x_{zpf}^2}{\gamma_m}\{1 + 2(\bar{n}_m^T + \bar{n}_{add})\} \quad (2.78)$$

We see in Eq. 2.78 that the measurement adds noise to the residual back action term, $\bar{n}_{bad}$, of Eq. 2.76*a*. This added noise term is given by the term $\bar{n}_{add}$ where

$$\bar{n}_{add} = \bar{n}_{bad} + \frac{\kappa}{\kappa_2}\frac{\gamma_m}{8\Gamma}\bar{n}_{amp} \quad (2.79)$$

In Eq. 2.79, $\bar{n}_{amp}$ is the number of quanta associated with the noise temperature of the amplifier. Notice from Eq. 2.78 that $\bar{n}_{add} = \frac{1}{2}\Delta X_1^2/x_{zpf}^2$ and hence the NR is

[***] Note that $\bar{n}_p$ is the average pump quanta due to a single pump. To be more precise, given that the red and blue drives are of equal strength, the average pump quanta in the SR is $2\bar{n}_p$.

Table 2.1 Device parameters for Figure 2.15b)

	Device1	Device2	Device3	Device4	Device5
$\frac{g}{2\pi}\ (\frac{kHz}{nm})$	7.5	84	80	200	1000
$\frac{\lambda}{2\pi}\ (\frac{kHz}{nm^2})$	0.15	2.1	1.7	4.7	6.8
$\frac{\kappa}{2\pi}\ (kHz)$	500	600	250	200	300
$\frac{\omega_m}{\kappa}$	11.14	10.5	20	20	20
$\frac{\kappa_2}{\kappa}$	0.3	0.15	0.75	0.75	0.75
$\frac{\omega_{sr}}{2\pi}\ (kHz)$	5	7.5	7.5	12.5	15
$\bar{n}_{amp}$	15	10	10	6	5

a)

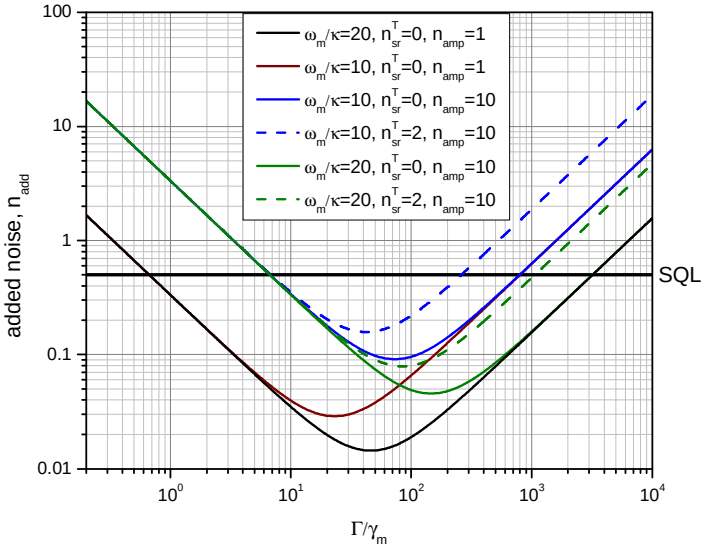

b)

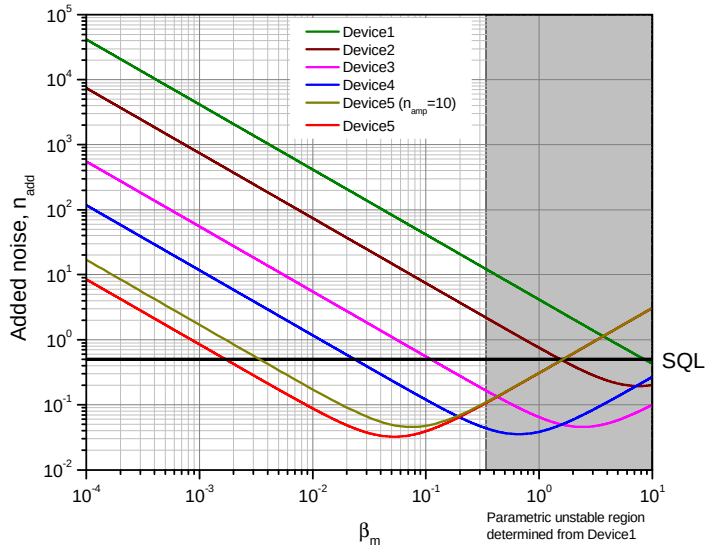

Figure 2.15 a) Added noise versus Γ/γ_m for reasonable NR-SR devices for various SR occupation, $\bar{n}_{sr}^{T}$, and amplifier noise temperatures, $\bar{n}_{amp}$. The case $\bar{n}_{amp} = 1$ corresponds to a shot-noise limited measurement. b) Added noise versus $\beta_m = 2\bar{n}_p\,\lambda x_{zpf}^2/\gamma_m$ for devices in Table 2.1.

squeezed below the SQL for $\bar{n}_{add} < \frac{1}{2}$ (See also references in [32]). Figure 2.15a) shows plots of added noise for reasonable devices in the resolved sideband limit. At low powers, increasing the double pump drive strength also increases the optomechanical strength, Γ, but not the intrinsic dissipation (which does not appreciably change in the absence of dynamical backaction effects). Thus, in the low power regime, the added noise, $\bar{n}_{add}$, and hence the uncertainty in position measurements of the X_1 quadrature reduces with increasing drive strength. At high powers, the backaction heating, $\bar{n}_{bad}$, associated with the bad cavity limit kicks in as the noise of the measurement noise floor begins to drive the NR and heat it up. In principle, as shown in Figure 2.15 *a*), careful engineering of the NR-SR can lead to QND-BAE squeezing below the SQL. This has never been demonstrated for a mechanical system and is the first step to demonstrating and creating quantum squeezed states of a mechanical device.

Empirical measurements of an all-Al NR-SR device has shown a parametric instability for the double pump configuration [33]. The onset of this instability occurs when the net frequency shift of the NR is about 30% of its intrinsic linewidth [33]. We can quantify this onset and estimate design parameters for next generation devices needed to do QND squeezing of the NR. Firstly the frequency shift at 30% of the intrinsic linewidth is mostly due to electrostatic pulling which is given by $\delta\omega_m^{elec} = \lambda x_{zpf}^2 2\bar{n}_p$, where λ is the second order coupling term of the Hamiltonian of Eq. 2.49 and $\bar{n}_p$ is the average number of pump quanta from the individual pumps (i.e. on average, there are $2\bar{n}_p$ pump quanta inside the SR). Using the empirical relationship, $\delta\omega_m^{elec} = \beta_m\gamma_m$, we can re-write Eq. 2.79 as

$$\bar{n}_{add} = \frac{1}{8}\left(\frac{g^2}{\kappa\lambda}\right)(\bar{n}_{sr}^T + 1)\left(\frac{\kappa}{\omega_m}\right)^2\beta_m + \frac{1}{\beta_m}\left(\frac{\kappa}{\kappa_2}\right)\left(\frac{\kappa\lambda}{g^2}\right)\frac{\bar{n}_{amp}}{16} \tag{2.80}$$

We can thus make estimates for design parameters of NR-SR devices for which the NR can be squeezed below the SQL. Consider the devices in Table 2.1 for instance. Device1 is the device of reference [33], Device2 is from reference [8] whereas

Device3, Device4 and Device5 are prototype designs for next generation devices which have NRs that can be squeezed by QND-BAE to below the SQL as shown in Figure 2.15 b).

CHAPTER 3: DESIGN AND FABRICATION

This chapter describes the design and fabrication recipes used in making the SR and NR-SR devices of this dissertation. We start by going through the key design parameters in section 3.1 before describing the fabrication sequence in section 3.2. This fabrication procedures build on previous work done by the group. See for instance Ph.D dissertations by Lahaye [34], Naik [35], Triutt [36], in which they describe the fabrication of a NR coupled a Single Electron Transistor (SET). More recently to this writing, Hertzberg's Ph.D. dissertation [37] covers the main points of the fabrication steps for an all Aluminum NR-SR device. In section 3.2, we shall update the fabrication procedures to include Nb based devices as well. At the end of the fabrication, the devices are wirebonded in the cleanroom unto a sample box. See Hertzberg's PhD Dissertation [37] for a description of the sample box used.

3.1 Design and Material

3.1.1 Design of Microwave Resonator

A $\lambda/2$-SR device can be implemented using a coplanar waveguide (CPW) with coupling capacitors at the input and output as shown in Figure 2.1. Turning our attention to the design of the CPW, we can write the characteristic impedance, Z_{ch}^{CPW}, in Ω of the CPW shown in Figure 3.1 as [38]

$$Z_{ch}^{CPW} = \frac{60\pi}{\sqrt{\varepsilon_{r,eff}}}\left(\frac{\mathcal{K}(k)}{\mathcal{K}(k')} + \frac{\mathcal{K}(k_1)}{\mathcal{K}(k_1')}\right)^{-1} \tag{3.1}$$

In Eq. 3.1, $\mathcal{K}$ is the complete elliptic integral of the first kind with

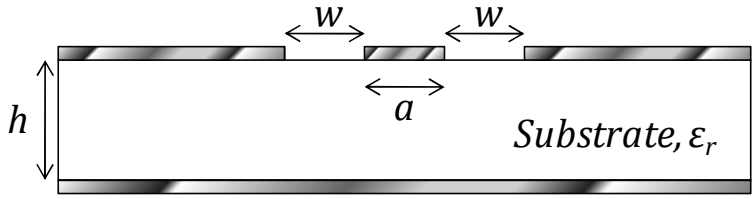

Figure 3.1 Sketch of a coplanar waveguide

$$k = tanh\left[\frac{\pi}{4}\frac{a}{h}\right]\Big/tanh\left[\frac{\pi}{4}\frac{a+2w}{h}\right], \qquad k' = \sqrt{1-k^2} \tag{3.2}$$

$$k_1 = tanh\left[\frac{\pi}{4}\frac{a}{h_1}\right]\Big/tanh\left[\frac{\pi}{4}\frac{a+2w}{h_1}\right], \qquad k_1' = \sqrt{1-k_1^2} \tag{3.3}$$

where a is the width of the center line, w is the distance between the center line and the ground plane, h is the thickness of the substrate and h_1 is the height from the metal top cover from the CPW. The effective dielectric constant, $\varepsilon_{r,eff}$, is given by

$$\varepsilon_{r,eff} = 1 + (\varepsilon_r - 1)\frac{\mathcal{K}(k)}{\mathcal{K}(k')}\left(\frac{\mathcal{K}(k)}{\mathcal{K}(k')} + \frac{\mathcal{K}(k_1)}{\mathcal{K}(k_1')}\right)^{-1} \tag{3.4}$$

where ε_r is the dielectric constant of the substrate. The coupling capacitors of the CPW determine the external dissipation from the input and output port as described in the beginning of section 2.1.1. Each coupling capacitor can be designed as an interdigitated capacitor with capacitance, C_{int}, in units of F given by [38, 39, 40]

$$C_{int} = \frac{\varepsilon_{r,eff}}{18\pi}\frac{\mathcal{K}(k_{int})}{\mathcal{K}(k_{int}')}(n-1)l_f \tag{3.5}$$

where $n \geq 2$ is the number of fingers, l_f is the length of each finger and

$$k_{int} = tan^2\left[\frac{\pi}{4}\frac{w_f}{w_f+s}\right], \qquad k_{int}' = \sqrt{1-k_{int}^2} \tag{3.6}$$

In Eq. 3.6, w_f is the width of each finger and s is the gap between fingers. Notice also that the resonant length, l, in m of the $\lambda/2$-CPW (length between the coupling capacitors) is related to the SR frequency, f_{sr}, according to the equation

$$l = \frac{1}{2}\frac{c}{\sqrt{\varepsilon_{r,eff}}}\frac{1}{f_{sr}} \tag{3.7}$$

where c is the speed of light in vacuum. Using Eq. 3.1 and 3.7 above we can thus design SR devices with various characteristic impedances and resonant frequencies. Table 3.1 shows typical values for the characteristic impedance and the interdigitated capacitance from the geometric properties of the SR. From Eq. 3.7, a *7.5GHz* SR on a high resistivity Si substrate would need 11.8mm long CPW.

Table 3.1 a) Design of typical CPW b) Design of typical interdigitated capacitor

$a/\mu m$	$w/\mu m$	Z_{ch}^{CPW}/Ω
10	16	50
4	66	115
4	106	125
2	100	141

a)

$l_f/\mu m$	$w_f/\mu m$	$s/\mu m$	C_{int}/fF
25	2	4	2.2
7	4	2	1.0
5	2	2	0.6

b)

The $\lambda/2$-CPW described above can be modeled as an open circuit $\lambda/2$-transmission line which can in turn be modeled as a parallel LC circuit [37, 41, 42]. This leads to the conversion equation between the characteristic impedance of the CPW and the capacitance of the parallel LC circuit parameters given by

$$C = \frac{\pi}{2}\frac{1}{\omega_{sr} Z_{ch}^{CPW}} \tag{3.8}$$

The characteristic impedance and hence the inductance of the LC circuit can easily be derived from Eq. 3.5 for the nth mode of the CPW [37,42]. We can write for the nth resonance that

$$\omega_n = n\omega_{sr} \tag{3.9a}$$

$$C_n = \frac{n\pi}{2}\frac{1}{\omega_{sr} Z_{ch}^{CPW}} \tag{3.9b}$$

$$L_n = \frac{2}{n\pi}\frac{Z_{ch}^{CPW}}{\omega_{sr}} \tag{3.9c}$$

$$Z_n = \frac{2}{n\pi} Z_{ch}^{CPW} \tag{3.9d}$$

3.1.2 Design of Nanomechanical Resonator

The NR used in this work is a free vibrating cantilever beam clamped at both ends. The fundamental mechanical frequency of such a flexural beam can be estimated from the dimensions and material properties of the beam. For an n-layer beam, the fundamental mechanical frequency, f_m, is given by [43]

$$f_m = \left(1.03\frac{w_m}{l_m^2}\sqrt{\frac{E_{eff}}{\rho_{eff}}}\right)\sqrt{1 + \frac{\sigma_{eff} l_m^2}{3.4 E_{eff} w_m^2}} \tag{3.10}$$

where w_m is the width of the cantilever beam in the plane of vibration, l_m is the length of the beam, ρ_{eff} is the effective density, E_{eff} is the effective Young's Modulus and σ_{eff} is the effective stress of the doubly clamped beam. The effective quantities are defined via the parameter $\vartheta \in \{\rho, \mathrm{E}, \sigma\}$ as

$$\vartheta_{eff} = \frac{1}{t}\sum_{i=1}^{n} \vartheta_i t_i \tag{3.11}$$

where t_i is the thickness along the out-of-plane direction of the i-th layer giving a total thickness of $t = \sum_{i=1}^{n} t_i$. Eq. 3.10 was used as a starting point to estimate the fundamental frequency of the cantilever beams of the NR-SR devices used in this work. Typically, we fabricate Al-NR beams that are 30μm long, 150nm wide and 100nm thick sitting on 60-70nm thick high stress silicon nitride (hs-SiNx). The hs-SiNx layer has ~1200MPa of tensile stress on it and this ensures high frequency beams which give high Q [45]. For these parameters, Eq. 3.10 predicts a resonance frequency of *6.85MHz* which is within 10-20% of what we measure in practice.

3.1.3 Physical Design Layout of NR-SR

Figure 3.2 a) shows the physical layout of a typical NR-SR device chip used in this work. Each end of the chip has a 50 Ω bonding pad that connects the center line of the NR-SR to the sample box via Al wirebonds. There are two coupling capacitors, one at each end of the CPW of the SR as shown in Figure 3.2 b). These determine the Q factor of the SR. The meandering of the centerline is necessary to accommodate the length of the CPW which is determined by the SR frequency. For the fundamental $\lambda/2$ resonance, a voltage maximum develops at the location of the coupling capacitors. We thus design and place the NR near the input coupler to ensure maximum sensitivity. The boxes on near the edge of the chips contain labeling information and alignment marks for lithography. The chip size for the devices discussed in this writing were 3.5mm x 10mm.

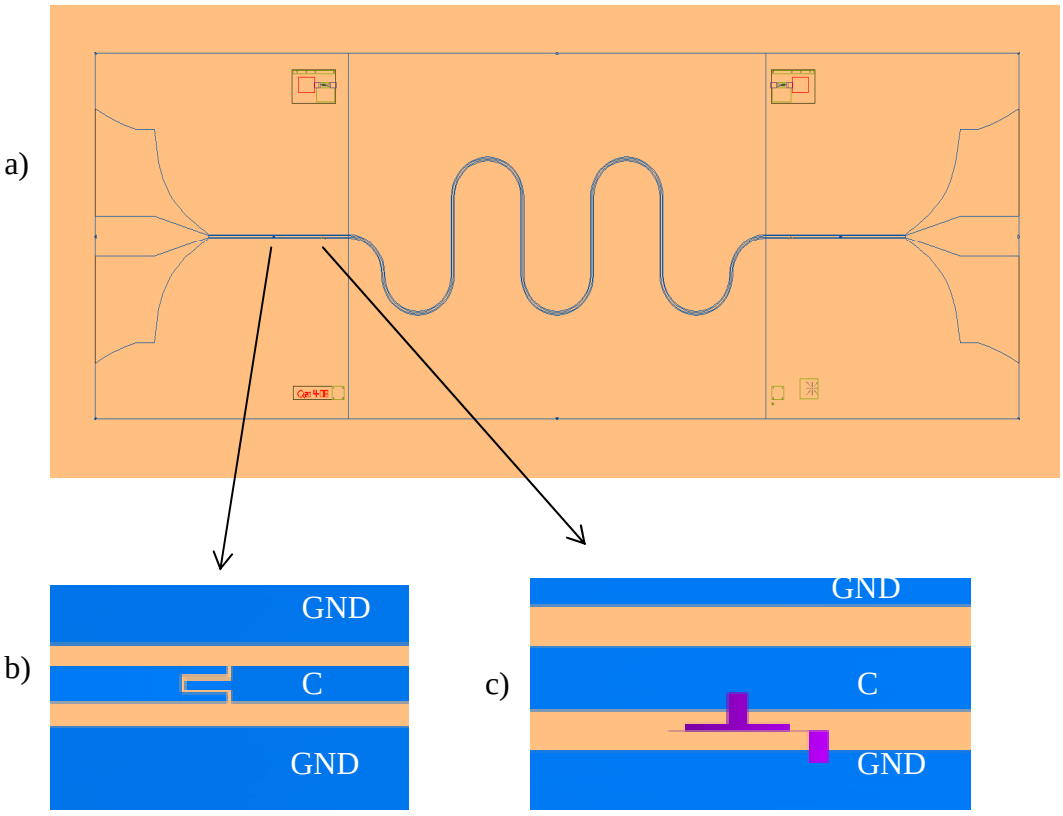

Figure 3.2 a) Physical layout of a NR-SR device chip. b) layout of a 3-finger interdigitated capacitor at the input end of the NR-SR. C is the center line and GND is the ground plane of the SR. c) layout of a grounded NR coupled capacitatively to the SR via a gate.

3.1.4 Materials used for NR-SR device

The SR and NR-SR devices are operational at low temperatures including milliKelvin (mK) temperatures of the dilution fridge. We used high resistivity Silicon (Si) as substrate for our devices to minimize dielectric loss. The main metals used were Aluminum (Al) and Niobium (Nb) with bulk superconducting properties tabulated in Table 3.2 below. Fabricating Al-SR devices is fairly straight forward and easy compared to Nb-SR devices. Thus we initially made our SR devices out of Al which has reasonable superconducting properties as shown in Table 3.2. These devices which could only be measured at mK temperatures suffered from low power handling issues. This is because, as it turned out, cooling our NR to below 10 quanta say, requires a large number of pump quanta ($\sim 10^9$) inside the SR and this is enough to cause the Al-SR to begin to go normal.

Table 3.2: Superconducting properties of bulk Aluminum and bulk Niobum taken from [44]

Material	Bulk T_c (K)	Bulk H_{c1} (G)	Coherence length, $\xi(nm)$	London length, $\lambda_L(nm)$
Aluminum	1.14	105	1600	16
Niobium	9.5	1980	38	39

We thus switched to Nb-SR devices which have the advantage that they can be tested quickly at ~1K in a 1K fridge and also that they are at least 100 times better in power handling compared to their Al counterpart. For the NR, we used mainly Al beams following in the tradition of our research group. To improve the mechanical quality factor of the NR, we made bi-layer beams with the Al sitting on high stress silicon

nitride (hs-SiNx). The use of hs-SiNx was motivated by the fact that Verbridge et al [43, 45] showed that hs-SiNx beams have phenomenally high mechanical Qs. In addition, they show that adding tensile stress to a silicon nitride nanostring improves its frequency and hence Q factor (the mechanical linewidth is unchanged). Our Al/hs-SiNx NRs consistently yielded high mechanical Qs at reasonable frequencies. We also made a handful of Nb/hs-SiNx NRs which were tested as well. In the next section we describe the fabrication sequences for the SR and NR-SR devices.

3.2 Fabrication

We have designed and fabricated high-Q NRs that are parametrically coupled to high-Q SRs. Fabrication of the devices used in this dissertation was done primarily at the Cornell Nanoscale Facilities (CNF) [46]. We briefly used the Penn State University cleanroom [47] to do electron beam lithography during one of our device fabrication run. We purchased wafers from various vendors including the CNF, SiliconQuest, Silicon Valley Microelectronics and Utrasil [48]. In the sections that follow, we describe the fabrication process firstly for the bare SR devices and then the NR-SR devices. For each section, we describe the fabrication of Al devices followed by Nb devices.

3.2.1 Fabrication of SR Devices

SR devices are fabricated on high resitivity, $\rho > 10k\Omega cm$, bare 100-Si. We have also fabricated SR devices on high resistivity Si wafers which have hs-SiNx patches on them. The fabrication of such nitride patches will be discussed in section 3.2.2.1. We have been able to make both Aluminum (Al) and Niobium (Nb) SR devices. See [15, 16, 17] for similar SR devices that have been reported in the literature.

3.2.1.1 Fabrication of Al-SR Devices

After finalizing the design of the SR device of interest, we write the SR-photomask using the CNF's DWL Heidelberg mask writer. Starting with a bare high resistivity Si wafer, we perform standard photolithography with a bilayer resist to pattern the SR

- Spin LOR5A at 5500rpm for 60sec, bake at 180^{o}C for 3-5mins
- Spin S1813 at 5500rpm for 60sec, bake at 115^{o}C for 60sec
- Expose SR-photomask pattern using the 5x-g-line stepper at 0.5sec per die.
- Develop exposed bilayer resist in MIF 300 for 60-70sec. We usually get *~500nm* of undercut for this recipe.

After optical inspection to confirm that the pattern looks good, we proceed with the deposition and lift off of the metal.

- Thermal evaporate ~300nm of Al at 4-5 Å/s at a pressure of $1 \times 10^{-7} Torr$
- Lift off (usually for more than 4hrs) in resist remover, 1165

This process sequence is shown in Figure 3.3. A scanning electron microscope (SEM) image of the input coupling capacitor at the end of fabrication is shown in Figure 3.4. After this step, the wafer can now be diced up into SR-chips and packaged for measurement.

3.2.1.2 Fabrication of Nb-SR Devices

To minimize cost, we use the same SR-photomask used for the Al-SR devices to fabricate Nb-SR devices. Since the Nb-SR devices are fabricated by a subtractive process we reverse the tone of the photoresist (PR) to create the pattern for the Nb-SR

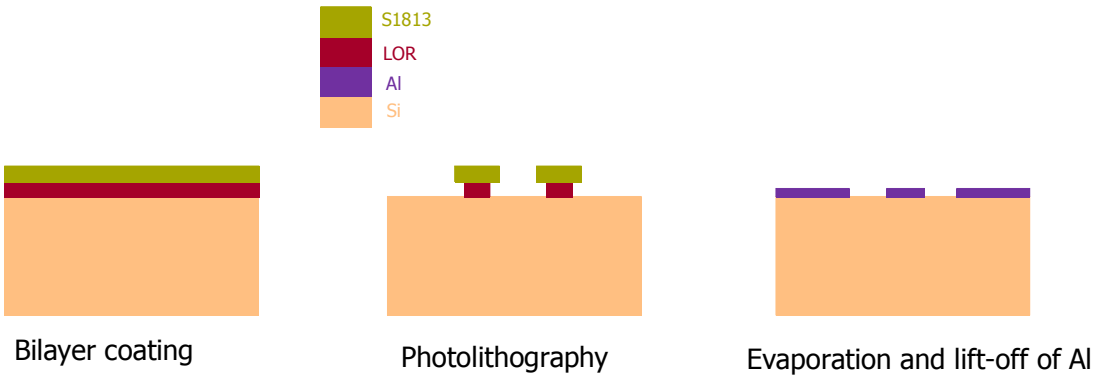

Figure 3.3 Shematic sketch of Al-SR fabrication process

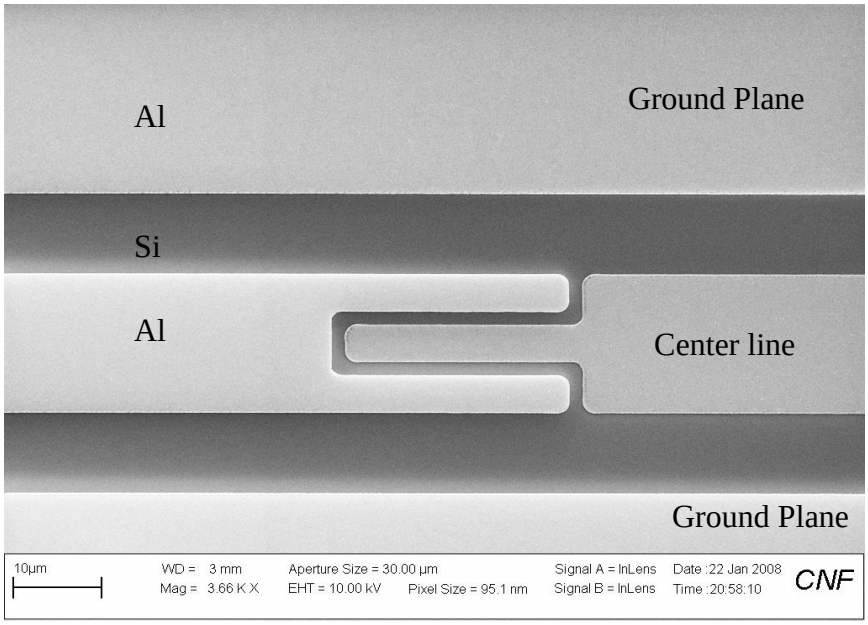

Figure 3.4 Input 3 finger interdigitated capacitor of an Al-SR device.

as described below. Firstly we sputter ~300nm of Nb on the high resistivity 100-Si wafer. Using the CVC Sputter Deposition system (base pressure $<5x10^{-7}$Torr, 2KW DC, 2.5mTorr of Ar, deposition rate ~137Å/min) at the CNF, we were able to sputter good quality Nb films with T_c in the range 7.5-8K. Later on during the project, we were fortunate to have the Nb sputtering done at NASA's Jet Propulsion Laboratory (JPL) at CalTech [49]. The T_c of the Nb films from the JPL was always in the range 8.9 - 9.5K which is comparable to bulk. With the Nb coat on the wafer, we proceed to fabricating the Nb-SR as shown schematically in Figure 3.5. Starting with standard photolithography, we pattern the Nb-SR device.

- Spin SPR 220 3.0 at 5500rpm for 60sec, bake at 115^{o}C for 90sec
- Expose SR-photomask pattern using the 5x-g-line stepper at 1.6sec per die.
- Post exposure bake the SPR at 115^{o}C for 90sec.
- Reverse the tone of the exposed SPR by baking it in 600Torr of NH_3 in the YES 58-SM oven.
- Flood expose the SPR for 60sec using the EV620 contact aligner
- Develop the SPR in MIF 300 for 70sec or in MIF 321 for 100sec.

After optical inspection to confirm that the pattern looks good, we proceed to etch the Nb.

- Etch the Nb metal using the Oxford PlasmaLab 80+ RIE System (50W, 40mTorr, 100 sccm of CF_4/10 sccm of O_2). CF_4/O_2 etches the Nb vertically with little or no undercut as seen in Figure 3.6. This etch is non-uniform across the wafer but on average etches the Nb at ~20nm/min. Doing 1-2mins O_2 descum every 4-5mins of the etch softens the hardened resist + Nb complex that forms on the walls of the SPR etch mask.
- Strip the SPR resist in 1165. See Figure 3.6 for SEM of a coupling capacitor.

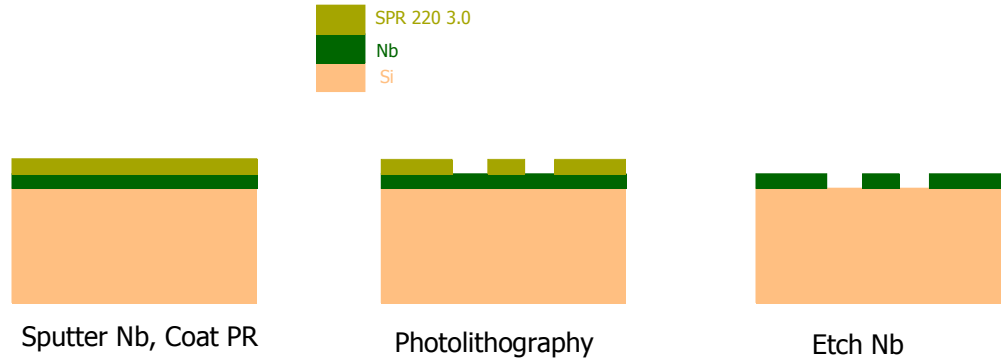

Figure 3.5 Schematic sketch of Nb-SR fabrication process

a)

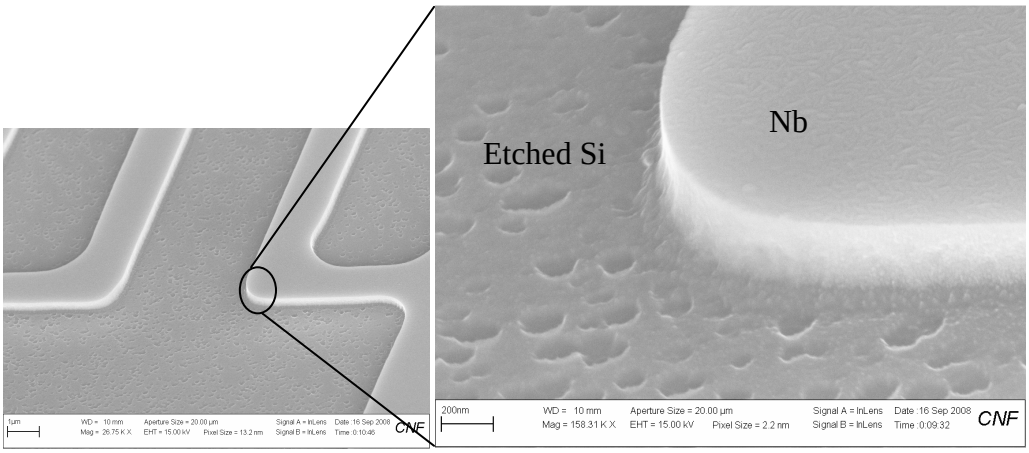

b)

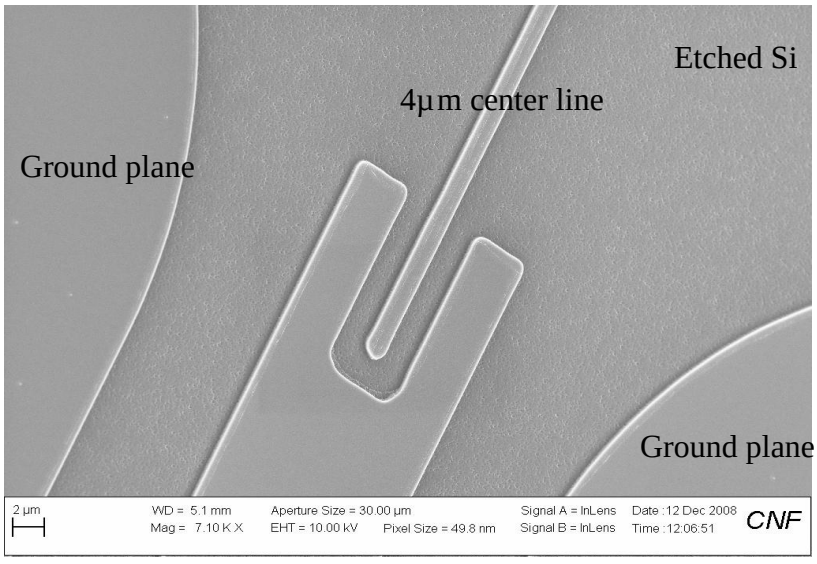

Figure 3.6 SEMs a) showing vertical etch of CF_4/O_2 and b) a coupling capacitor for a high Z Nb-SR.

After this step, the wafer is diced into SR-chips and packaged for measurement.

3.2.2 Fabrication of NR-SR devices

The NR-SR devices of this dissertation were fabricated on dielectric substrate made of hs-SiNx rectangular patches on a high resistivity 100-Si wafer. In the early stages of this project, we observed that the Qs of SR devices fabricated on hs-SiNx/Si substrate were consistently extremely low. This could be attributed to dissipative channels that exist either in the hs-SiNx, or more likely in the hs-SiN/Si interface. Thus we resorted to etching all the hs-SiNx except for patches needed for the NR beam. The nitride patches (needed for the NR beams) are patterned such that they would lie in the gap region between the ground plane and center line of the fabricated SR. That way, the SR is fabricated directly on Si (to get reasonable electrical Qs) and we still have the luxury of coupling the NR beams on the thin nitride patches (which give high mechanical Qs) to the SR. We start by outlining the fabrication recipe for creating the hs-SiNx patches on bare Si

3.2.2.1 Fabrication of hs-SiNx Patches on Si Substrate

Firstly we grow 70-100nm if hs-SiNx on a high resistivity 100-Si wafer using the low pressure chemical vapor deposition (LPCVD) furnace at the CNF (T = 775^{o}C, P=224mTorr, 98% of NH_3, 40% Dichlorosilane). Using standard photolithographic techniques we pattern a photoresist to cover the regions where the hs-SiNx patches will be formed as described below

- Spin SPR 220 3.0 at 5500rpm for 60sec, bake at 115^{o}C for 90sec
- Expose the hs-SiNx-mask pattern using the 5x-g-line stepper at 1.6sec per die.
- Post exposure bake the SPR at 115^{o}C for 90sec.
- Develop the exposed SPR in MIF 321 for 100sec or in MIF 300 for 70sec.

- After optical inspection, bake in 90^{o}C oven for at least 6-8hours

After about 8hours of bake to harden the SPR, we proceed to etch the nitride layer everywhere on the wafer except for the nitride patches.

Reactive Ion Etch (RIE)

- Use Filmetrics F40/F50-EXR to measure the thickness of hs-SiNx at the start of the etch
- Etch the hs-SiNx using the Oxford PlasmaLab 80+ RIE system (150W, 55mTorr, 50sccm CHF_3/5 sccm O_2) until only about 10-20nm thick of nitride is left. Measure the nitride film thickness periodically during the etch.

Buffered Oxide Etch (BOE)

- Use BOE (6:1) to etch the remaining 10-20nm of nitride in about 10-15mins. BOE (6:1) etches hs-SiNx very slowly at ~0.5-1nm/min.
- Rinse in DI water. A quick test to determine if all the nitride has been etched is to check if DI water wets the surface or not. Water does not wet a Si surface because Si is hydrophobic. Water wets hs-SiNx as it is hydrophilic.
- Optical inspect and use Filmetrics F40/F50-EXR to determine that all the unwanted nitride has been etched away.
- Strip the remaining SPR in 1165 at the end of the first BOE etch.
- BOE (6:1) etch to trim the hs-SiNx patch to the desired thickness of ~60-65nm
- Rinse thoroughly in water and blow dry.

3.2.2.2 Fabrication of Al-NR-SR Devices

In this section we outline the fabrication of Al-NR-SR (Al-NR coupled to Al-SR) devices. Also see Hertzberg's PhD dissertation [37]. We use the hs-SiNx patches on Si

wafer described above in Section 3.2.2.1 as substrate. Using this substrate, the fabrication of the Al-SR follows exactly the same process described in section 3.2.1.1 with the same photomask. After the completion of lift-off, we proceed to coupling the Al-NR to the Al-SR using electron beam (ebeam) lithography. The design pattern used to write the NR beams are such that the NR is usually 60-200nm from a gate which is in direct electrical contact with the center line of the SR. One end of the NR lead is connected to the ground plane of the SR.

Ebeam #1

- Spin PMMA 495 A4 at 2000rpm (~200nm) for 60sec, bake at 170^{o}C for 15mins
- Spin PMMA 950 M2 at 2000rpm (~150nm) for 60sec, bake at 170^{o}C for 15mins
- Expose NR design pattern using the Leica VB6 or the JEOL 9300 at the CNF (100kV accelerating voltage, 1nA beam current, 1200-1400 $\mu C/cm^2$ dose)
- Develop exposed bi-layer resist in MIBK:IPA = 1:3 for 90sec
- Rinse in IPA for 30sec
- After optical inspection, do a low power 8-10sec O_2 descum using the Oxford PlasmaLab 80+ RIE system (50W, 60mTorr, 50sccm of O_2)
- Evaporate 80-100nm of NR Al at 4-5Å/s at a pressure of $1 \times 10^{-7} Torr$
- Lift-off in methylene chloride : acetone ~ 1:1 for > 4hours
- Rinse in IPA
- Use the scanning electron microscope (SEM) to inspect the beams

After the SEM inspection, the wafer can now be diced into 3.5mm x 10mm chips in preparation for the second ebeam step to free the NR beams. The second ebeam step

writes a rectangular window around the beam which is later used to etch the substrate around the beam, thus releasing it.

Ebeam #2

- Spin PMMA 495 A8 at 4000rpm (~450nm) for 60sec, bake at 170^{o}C for 15mins
- Expose the hs-SiNx window design pattern using the Leica VB6 or the JEOL 9300 at the CNF (100kV accelerating voltage, 1nA beam current, 1400-1800 $\mu C/cm^2$ dose)
- Develop exposed resist in MIBK:IPA = 1:3 for 90sec
- Rinse in IPA for 30sec
- Optical inspect for alignment.

The beams are released in two consecutive RIE processes, one to vertically etch the nitride layer and the second to isotropically remove the silicon underneath the beams.

Freeing Al-beams

We mainly use the Oxford PlasmaLab 80+ RIE system to free the Al beams with the following procedure

- 2mins of vertical hs-SiNx etch (150W, 55mTorr, 50sccm CHF_3/5 sccm O_2, etch rate ~60nm/min)
- 35-60sec of isotropic Si etch (100W, 125mTorr, 60sccm SF_6, etch rate ~500-700nm/min)
- 20-30mins of low power O_2 descum to strip the residual resist (50W, 60mTorr, 50sccm O_2)
- SEM inspect the freed beams

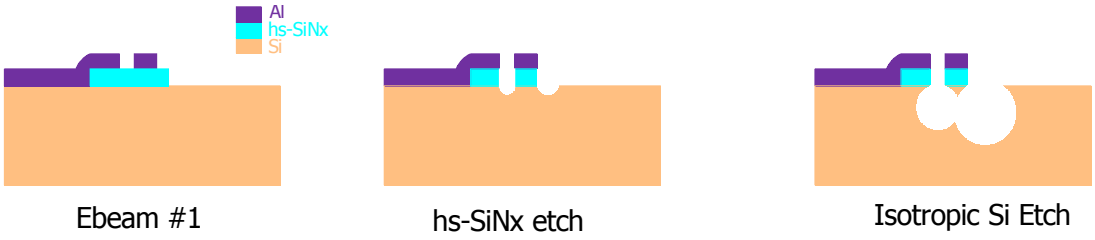

Figure 3.7 Schematic diagram of the process sequence of freeing an Al/hs-SiNx beam.

a)

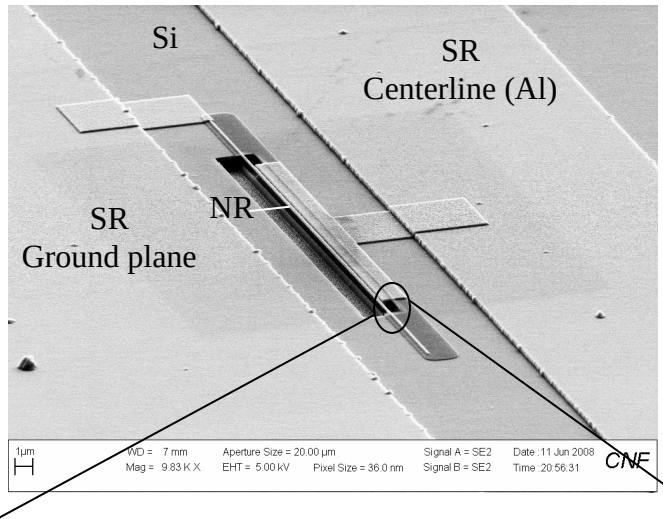

b)

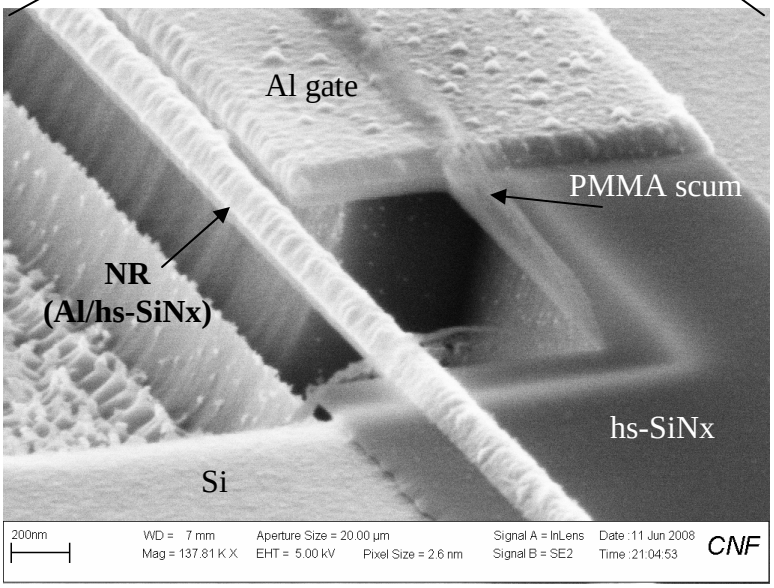

Figure 3.8 a) SEM of suspended Al-NR coupled to the Al-SR b) Notice the hs-SiNx layer underneath the Al metal of the NR and also the undercut portion of the gate at the edge of the Al-NR.

We usually break vacuum between the etch step above to optical inspect the beams. The Al is an etch mask and so the NR survives the etches. This process sequence is shown schematically in Figure 3.7. In Figure 3.8 a) we show an SEM picture of an Al-NR coupled to an Al-SR. Zooming in on the side of the freed beam, we see the composite layers that make up the NR.

Critical Point Drying

The long and potential harmful O_2 descum above to strip the resist can be avoided by doing critical point drying (CPD). Proceed with CPD after the Si etch above as follows (the chips are always in solution until the end of the CPD process).

- Strip resist in methylene chloride (or acetone)
- Rinse in IPA, rinse in methanol
- Critical point dry in methanol
- SEM inspect the freed beams

At this point, the chips are now ready for wirebonding and packaging for low temperature diagnosis and measurements.

3.2.2.3 Fabrication of Al/Nb-NR-SR Devices

We have fabricated NR-SR devices by coupling Al-NRs to Nb-SRs. Again we use the hs-SiNx patches on Si substrate as the dielectric layer. Because the hs-SiNx is susceptible to the Nb etch (CF_4/O_2), we first perform standard photolithography and Al evaporation to protect it. Al amongst other materials like Al_2O_3, SiO_2 are resistant to the CF_4/O_2 Nb etch. We use an Al etch mask because it is easier to fabricate Al. The design for the Al-etch photomask used contains a large rectangle (30µm x 80µm) that covers and protects the hs-SiNx patches on the wafer.

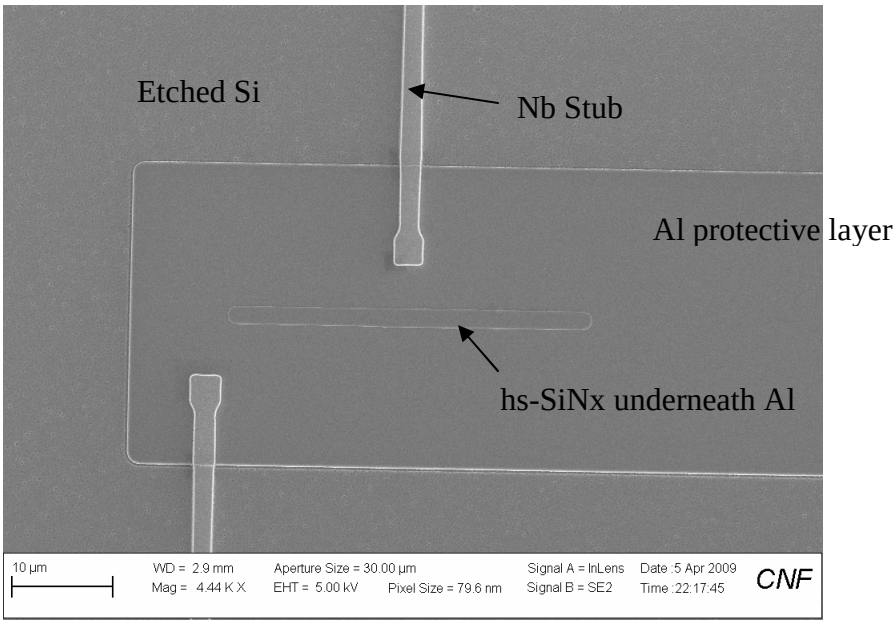

Figure 3.9 SEM of Nb stubs on Al etch mask in the gap region. Notice the hs-SiNx patch outline between the two stubs.

- Spin LOR5A at 5500rpm for 60sec, bake at 180^{o}C for 3-5mins
- Spin S1813 at 5500rpm for 60sec, bake at 115^{o}C for 60sec
- Expose Al-etch photomask using the 5x-g-line stepper at 0.5sec per die.
- Develop exposed bilayer resist in MIF 300 for 60-70sec.
- Thermal evaporate 100nm of Al at 4-5 Å/s at a pressure of $1 \times 10^{-7} Torr$
- Lift off (usually for more than 4hrs) in resist remover, 1165

At the end of this fabrication segment, the hs-SiNx is completely covered by a 30 µm x 80 µm Al etch mask for protection from the Nb etch. The next step in the fabrication sequence is the sputtering of 300nm of Nb at the CNF (base pressure <5x10^{-7}Torr, 2KW DC, 2.5mTorr of Ar, deposition rate ~137Å/min) or more preferably at NASA's JPL at CalTech. After the Nb sputtering, we proceed to etch the Nb to create SRs. The

photomask used for the SR fabrication is similar to that of section 3.2.1.2, but in addition has two stubs in the gap region between the center line and the ground plane of the SR. One stub extends from the centerline while the other extends from the ground plane. They both overlap with the Al etch mask that protects the nitride patches. Thus in the long run the Al will serve both as an etch mask as well as ensure electrical continuity between the NR and the SR in the regions where the Nb stubs overlap the Al. After finalizing the design of the photomask and writing it using the CNF's DWL Heidelberg mask writer, we fabricate the Nb SR as described in section 3.2.1.2. During the Nb etch process, care is taken to ensure that there is no persistent resist left behind. This is achieved by doing regular 1-2mins O_2 cleans to etch the hardened resist complex that forms in-situ during the Nb etch. This is essential since in the final steps we will electrically connect this Nb to the Al of the NR and also to the Al of the gate. At the end of the SR fabrication, the Nb stubs overlap the Al etch mask. Figure 3.9 shows the top view of the Nb stubs on the sacrificial Al mask in the gap region between the center line and the ground plane. With the help of standard photolithography we etch the protective Al everywhere except underneath and just around the Nb stubs.

- Spin SPR 220 3.0 at 5500rpm for 60sec, bake at 115^{o}C for 90sec.
- Expose Nb/Al overlap photomask using the 5x-g-line stepper at 1.6sec per die.
- Post exposure bake the SPR at 115^{o}C for 90sec
- Develop exposed resist in MDC: DI water ~1:1 for ~100sec.
- Rinse in DI water

After optical inspection to make sure that the patterned photoresist completely covers the Nb/Al overlap region, we proceed to remove the Al etch mask

- Etch the Al for 3.5-5mins using Al etchant (transene A)

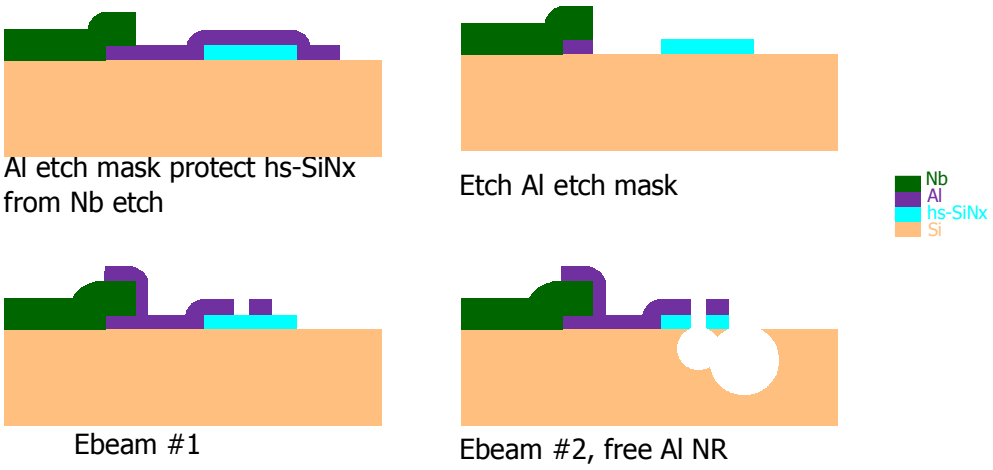

Figure 3.10 Schematic sketch of process sequence for the fabrication of Al/Nb-NR-SR deviecs

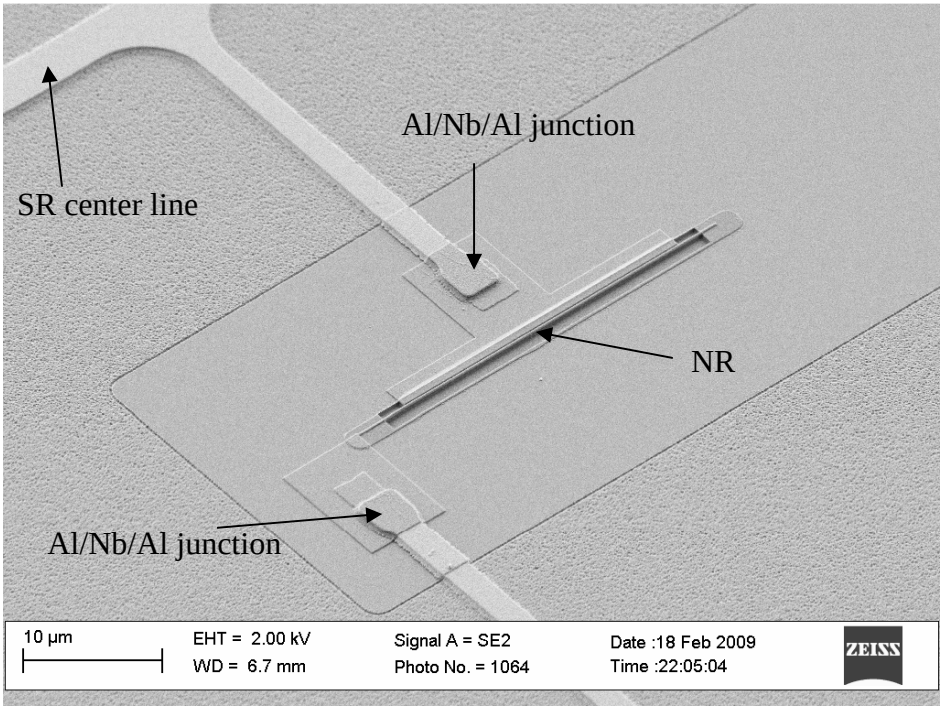

Figure 3.11 SEM showing suspended NR of a Al/Nb NR-SR device

- At the end of the etch, the hs-SiNx should be clearly visible
- Strip the remaining PR in 1165

At this point of the fabrication, each SR (of the many SRs on the wafer) now has two Nb/Al stubs on opposite sides of the hs-SiNx patch. The Al-NR can now be coupled to the SR following the same fabrication procedures of Ebeam#1, Ebeam#2, Freeing Al-beams, described above in section 3.2.2.2. A summary of the fabrication sequence is shown in Figure 3.10. Figure 3.11 shows the suspended NR of a fabricated Al/Nb-NR-SR device.

3.2.2.4 Fabrication of Nb-NR-SR Devices

We have fabricated all Nb-NR-SR devices where we use the same Nb for the NR and the SR. We sputter ~150nm of Nb on the hs-SiNx patch on a high resistivity 100-Si substrate of section 3.2.2.1. The mask used for the SR fabrication is similar to that of section 3.2.2.3, but in addition the stubs extend further to cover and protect the nitride patches. Basically, the mask consists of a 15um x 50um rectangular cover for the nitride which is in direct contact with the two stubs that extend from the center line and the ground plane. Thus in the gap region near the hs-SiNx patch, the Nb extends from the center line to the ground plane without a break. Fabrication of the Nb-SR is exactly like in section 3.2.1.2. After the Nb etch and the resist strip, the SR is mostly formed but for the Nb in the gap region covering the hs-SiNx patches. We are now ready to couple the Nb-NR to this SR by subtractively etching the rectangular Nb cover. We start by writing gated Al beams on the Nb in the gap region such that the hs-SiNx patches are directly underneath the Al beams. This can be achieved by using the recipe Ebeam #1 of section 3.2.2.2 above. The Al is resistant to the Nb etch and thus we can transfer the pattern of the gated Al-beams unto the Nb by directly etching the unwanted Nb. A photomask that exposes only the region around the hs-SiNx

patches can now be used to pattern an etch window for this etch. We describe this photolithography process below

- Spin SPR 220 3.0 at 5500rpm for 60sec, bake at 115^{o}C for 90sec.
- Expose Nb etch overlay photomask using the 5x-g-line stepper at 1.6sec per die.
- Post exposure bake at 115^{o}C for 90sec
- Develop exposed resist in MDC: DI water ~1:1 for ~100sec.
- Rinse in DI water

After optical inspection to confirm that the etch windows are well aligned, we proceed to etching the Nb using CF_4/O_2 as described in section 3.2.1.2. At the end of the etch, the exposed hs-SiNx has been partially or completely etched away and the resulting Al/Nb gated beams are ready for release. The wafer is diced up into chips and prepped for the second ebeam process. This follows the same steps of Ebeam #2 of section 3.2.2.2. In particular we use thicker PMMA (e.g. 1µm of PMMA 495 A11) in anticipation of long etches.

Freeing Al/Nb-beams

The hs-SiNx by now has been partially or completely etched, and we are mainly concerned with etching the Si substrate around the beam. Again we use the Oxford PlasmaLab 80+ RIE system to do the etches below

- 30-60sec vertical hs-SiNx etch (150W, 55mTorr, 50 sccm CHF_3/5 sccm O_2)
- 30-60sec isotropic Si etch (100W, 125mTorr, 60sccm SF_6)
- ~3mins of low power O_2 clean (50W, 60mTorr, 50sccm O_2)

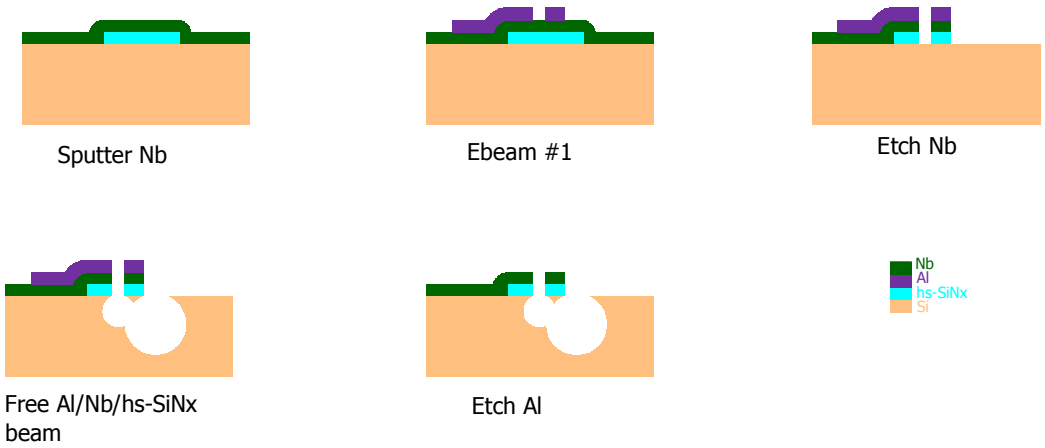

Figure 3.12 Schematic sketch of the process sequence for the fabrication of Nb-NR-SR devices.

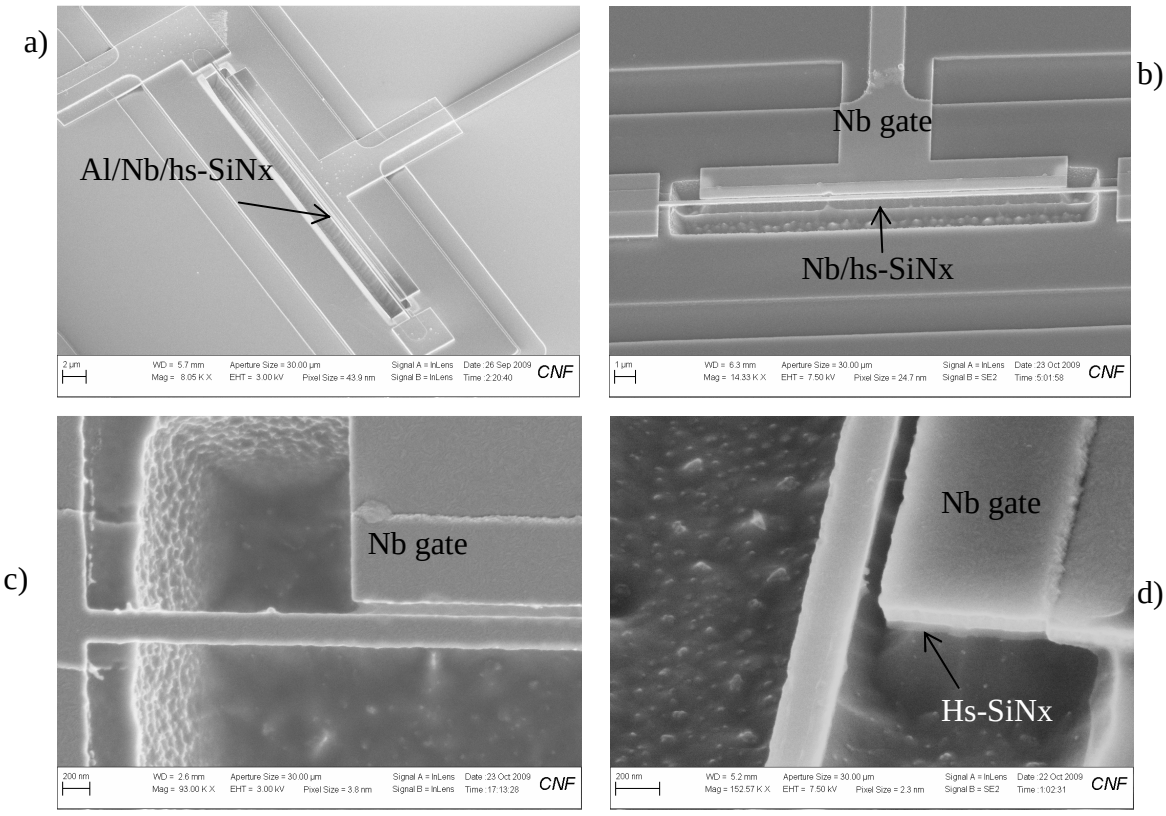

Figure 3.13 SEM of a) freed Al/Nb/hs-SiNx NR coupled to a Nb-SR, b) freed Nb/hs-SiNx NR c) magnified top view of one end of b) above, d) magnified angle view of the other end of b) showing the hs-SiNx layer underneath the Al of the gate.

The Al/Nb beams are released at this point (See Figure 3.13 (a)) and we next proceed to etch the sacrificial Al and dry the Nb beams to get functional Nb-NR-SR devices.

Al Etch and Critical Point Dry

The following fabrication steps are carried out in solution with particular care taken during chip transfer between solutions to ensure that there are no dry spots near the Nb-NR beam. At the end of the Al/Nb beam freeing process above, there is still some residual resists on the chips. We start by stripping this

- Strip resist in methylene chloride
- Rinse in IPA, then rinse in DI water
- Etch Al using Al etchant (transene A) for > 10mins
- Rinse in water, then rinse in IPA
- Rinse in methanol
- Critical point dry using methanol as solvent
- SEM inspect the freed beams.

Figure 3.13 b), c) and d) show SEM images of a suspended Nb-NR at the end of fabrication (after CPD). Notice that the NR and gate look cleaner with no persistent hardened resist after the CPD step. Compare with Figure 3.8 a) where we did not do a CPD. In Figure 3.12, we sketch a summary of the process sequence detailed above for the fabrication of Nb-NR-SR devices. At the end of the SEM inspect, the chips are ready for wirebonding and packaging for low temperature diagnosis and measurements.

CHAPTER 4: MEASUREMENT SETUP

The samples fabricated as described in Chapter 3 are tested and measured at low temperatures. We primarily use a 1K fridge for diagnostic tests and a dilution fridge unit for more elaborate measurements. The measurement set ups which includes the internal and external fridge wiring for various experiments are given below in section 4.1 for the 1K fridge and section 4.2 for the dilution fridge.

4.1 1K Fridge and Diagnostic Measurement Setup

One key advantage of using Nb in place of Al for making SR, is the fact that quick diagnostic measurements of Nb based devices can be made at 1K, before the more elaborate mK measurements. This is possible because of the high superconducting temperature of Nb (9.5K in bulk) compared to Al (1.14K in bulk). To this effect, we designed and built in-house a 1K fridge with a base temperature of ~1.3K for studying Nb based SR and NR-SR devices. The 1K fridge consists of a 4K stage, a 1K stage and a sample stage for mounting devices. See for instance [50, 51, 52] for a description of the operation of a 1K fridge. The rf wiring of the fridge consists of two microwave coaxial lines, one for the input and the other for the output signal, running from the top of the fridge at room temperature to the sample stage. UT-85 CuNi-CuNi coaxial cables connect the top of the fridge to the 1K stage while Nb-Nb coaxial lines connect the 1K stage to the sample on the sample stage. The total attenuation of the individual fridge lines from the top of the fridge to the sample stage at base temperature is ~5 +/- 2dB. Numerous manganin d.c. lines run from the top of the fridge to the sample stage. These are needed for thermometry and also for dc measurements (e.g. resistance and hence Tc measurements of Nb films). The

temperature of the fridge is measured using a calibrated LakeShore cernox (CX-1010) resistor which is mounted on the 1K stage. An Agilent Digital Multimeter (Agilent 34411A) at the top of the fridge measures the four point resistance of the cernox resistor and this is converted to temperature using the temperature calibration curve from LakeShore. The main diagnostic measurements done at 1K include S21, power handling, temperature dependence measurements of Nb-SRs and finding the mechanical frequency of the NR in Nb based NR-SR devices. In the remainder of this section, we describe the external circuitry used to study Nb devices at 1K. See [37] for the description of the sample box used in mounting samples on the 1K stage.

4.1.1 Circuit for S21 and Power Handling Measurement

The properties of a Nb-SR device, including its resonance frequency, Q factor and insertion loss, can be determined from the measurement of the transmission, S21, at various frequencies near resonance. This measurement can be achieved with the set-up shown in Figure 4.1 below. We measure S21 using a calibrated Agilent Network Analyzer (Agilent N5230A) that connects directly to the top of the fridge via blue Pasternak coaxial cables. The power handling of the SR can be determined from a Q versus power measurement. As you increase the drive power, the Q initially stays constant until it starts to drop at some threshold power. This threshold power sets the power handling of the SR. The SR can be driven directly using the Network Analyzer or the microwave source. The microwave source (Agilent E8257D) is connected via a power divider (Pasternack, PE2028) to the input line of the fridge. We use Pasternack flexible coaxial cables at the top of the fridge to connect these components.

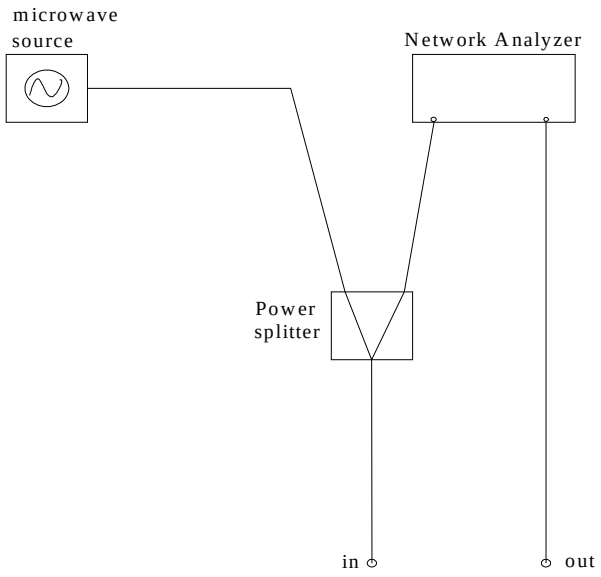

Figure 4.1 schematic set up for S21 and power handling measurement

4.1.2 Circuit for S21 and Temperature Dependent Measurement

By feeding back the thermometer reading to a heater attached to the 1K stage, we can monitor and control the temperature of the 1K stage. The setup shown in Figure 4.2 below can be used to implement this feedback. Both the thermometer (cernox resistor) and the heater which is a 1kΩ dissipative resistor, are mounted on the 1K stage. The Lockin (SRS SR830) drives a small current of ~10nA through the thermometer and measures the voltage drop across it. This is used to determine the resistance and hence temperature of the 1K stage. The voltage drop across the thermometer is fed into the measurement port of a PID (SRS, SIM900). The desired temperature of the 1K fridge can be entered into the PID which has an output port that connects directly to the heater at the 1K stage. Setting the desired temperature on the PID causes the system to

heat the 1K stage (or allow the 1K stage to cool) until the thermometer reads the same temperature (within tolerance) as the temperature set by the PID.

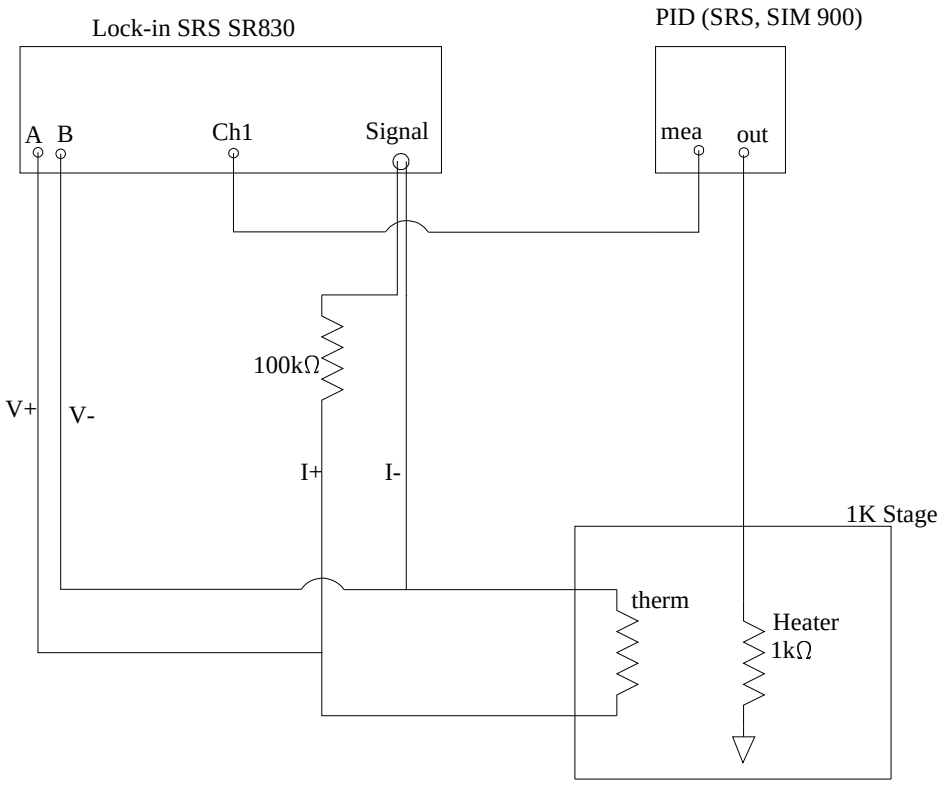

Figure 4.2 Schematic of set up for temperature dependent measurement

4.1.3 Circuit for Determining NR Frequency of NR-SR device

We have used several methods to search for the the weak mechanical sideband and hence mechanical frequency of NR devices. For instance in the early days of this project, we used magnetomotive at 4K to characterize NR devices. See Lahaye's PhD dissertation [34] for a description of the magnetometry technique. We have also used mixing techniques for NR-SR devices to find the mechanical sideband and hence NR frequency. In this technique, the NR-SR is driven at a detuned (preferably red)

frequency using a microwave source (Agilent E8257D) while sweeping the NR frequency using a Tektronix AFG3252 function generator. The output signal from the NR-SR is then mixed down using a local oscillator set at the detuned frequency of the microwave source to give the mechanical sideband. An even easier and quicker way to find the NR frequency is to modify the set up of Section 4.1.1 to have a low noise amplifier at the output of the fridge as shown in Figure 4.3 below. We use a MITEQ AFS-04700530-07-8P-4-GW low noise amplifier to amplify the weak signals of the mechanical sidebands. Using the microwave source, we drive the NR-SR preferably red detuned and observe the transmission, S21, on the network analyzer (NA). The S21 measured by the NA will show a dip in the lorentzian peak of the SR at a reasonable drive power in accordance with Eq. 2.66. The drive frequency can thus be adjusted to place the dip on the SR resonance (Eq. 2.68). This dip in the transmission with reasonable linewidth for a red drive confirms the mechanical sideband. By slowly increasing the drive strength, the mechanical linewidth should increase until it goes non-linear (into the Duffing regime). The linewidth going Duffing gives a second check that we are observing mechanical motion. Driving weakly at the blue sideband can also be used to determine the NR frequency. The main problem with the blue drive is the instability that arises at relatively low powers when the optical coupling strength becomes comparable to the intrinsic linewidth of the NR.

Diagnostic measurements at 1K ultimately lead to a device candidate for mili-Kelvin (mK) cool down. In section 4.2, we describe the internal wiring of the dilution refrigerator and the external measurement circuits used in studying the SR and NR-SR devices at mK temperature.

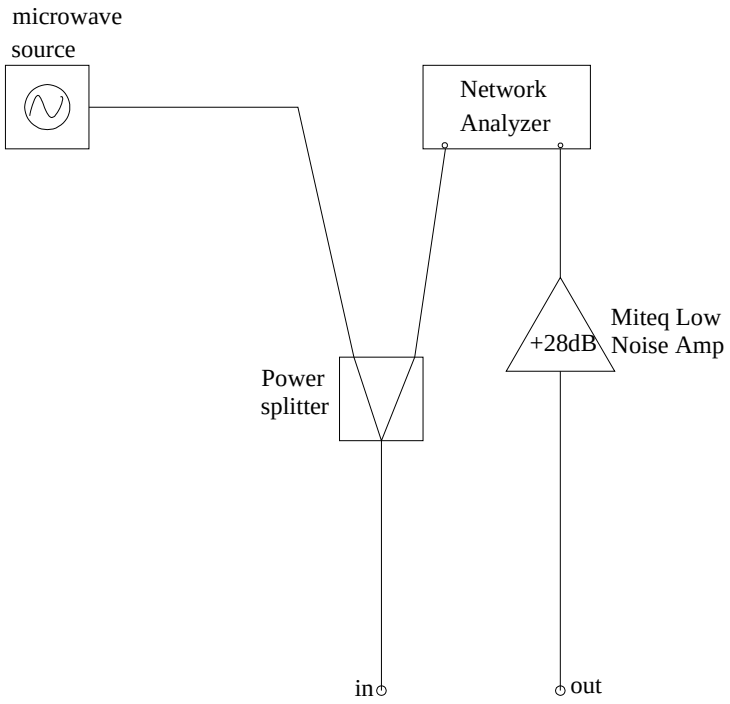

Figure 4.3 Set up used in finding the NR of a NR-SR device.

4.2 Dilution Fridge and Measurement Circuits

4.2.1 Internal Wiring of Fridge

We use the Oxford Kelvinox 400 dilution refrigerator with base temperature *<10mK* from Oxford Instruments [53] to study SR and NR-SR devices of this dissertation at *mK* temperatures. The fridge was mounted on a triangular optical table filled with lead bricks for support. The vertices of the optical table sat on three TMC air springs [54] and these provided vibration isolation. The three air springs were on top of three massive sand filled concrete pillars to support the weight of the dilution fridge and the helium-4 dewar that enclosed it. Vibration isolation from the mechanical pumps was provided by a bellows manifold on the still line at the top of the fridge. Raising and lowering the fridge for sample swap and fridge maintenance was achieved via a pulley system which uses lead bricks as counter weights. The fridge was housed in a shielded room with ~*-110dB* noise isolation between the inside and outside. The internal structure of a dilution fridge contains several key plates as described in [50, 51] for instance. During ideal operation of the fridge, these stages in descending order of temperature include the 4K plate (usually at ~ 4K), the 1K plate (usually at ~1.5K), the still plate (usually at ~ 700mK), the cold plate (usually at *50mK-100mK*), the mixing chamber plate (usually at base temperature) and the sample plate (at the same temperature as the mixing plate). The samples were wirebonded onto a sample box which was mounted on the sample plate. See Hertzberg's PhD Dissertation [37] for description of sample box. Notice that for a *7.5GHz* SR device, we expect the thermal occupation of the SR to be less than one quanta below $\hbar\,\omega_{sr}/K_B = 360mK$. Thus we were able to minimize direct heating of the cavity from the sample stage by keeping the mixing stage below this temperature. The temperatures of the plates below the 1K plates are measured using RuO resistors supplied by Oxford. An AVS-47B resistance

bridge measures the resistance and this can be converted to temperature using the calibration curves from Oxford. Feedback between the AVS-47B and a TS-530A temperature controller provides control of the temperature of the sample stage via heaters at the still and mixing stages. Given the huge gains in low temperature and cooling power of the dilution fridge over the 1K fridge, we have wired up a drive line, a low frequency line and a return line for fundamental quantum measurements of devices. We also wired ~10 auxiliary lines for diagnostic tests at mK temperatures.

Though the internal fridge wiring changed every 2-3 cool downs, we were keen to meet the following requirements every time before we cool a sample. We were careful to

- use only 50Ω microwave components to minimize any impedance mis-match and reduce any unwanted interference signals in the fridge lines.
- attenuate room temperature thermal noise from reaching the sample by using cold NiCr attenuators.
- attenuate black body radiation by using the cold attenuators above and also by covering all the open holes of the colder stages using copper tape to shield from the warmer stages of the fridge.
- make sure that the cold attenuators completely eliminated Johnson noise ($\sim K_B T$) of dissipative elements (especially from the room temperature components) at the sample.
- thermalize the inner and outer conductors of the microwave coaxial cables of the fridge lines. The outer conductors were physically bolted onto the fridge plates whereas the inner conductors were thermalized using Nb stripline coolers.
- shield the sample from stray magnetic fields in the environment.

Detailed solutions of the above have been discussed elsewhere in for instance Hertzberg's PhD dissertation [37], Lahaye's PhD dissertation [34]. We describe the basic internal wiring of the dilution fridge below.

The fridge has two main rf lines, the drive line and the return line, as well as a low frequency line for direct driving of the NR. The drive line between the top of the fridge and the 4K plate consists of a UT-85 CuNi-CuNi semirigid coax cable (Coax Co, Ltd, Japan). UT 63 CuNi-CuNi semirigid coax cable is used between the 4K plate and the cold plate. NiCr attenuators from Midwest Microwave are mounted inline at various stages to attenuate thermal noise and blackbody radiation. The cold attenuators on each stage are such that they completely eliminate the Johnson noise of the stage above. Two stripline coolers are connected at the still plate and the cold plate to thermalize the inner conductor of the coax cable of the drive line. Each stripline cooler is a Nb microstrip waveguide fabricated on high resisitivity Si. The superconducting microstrip line thermalizes the inner microwave line to the phonon temperature of the stage thus reducing electron heating at the sample. Nb-Nb coax cables connect the cold plate and the sample stage. The low frequency line which is a 0.012" diameter coax line runs from the top of the fridge at room temperature to the mixing stage. Cu powder filters connected inline at the 1K and mixing stage filter high frequency signals[34]. A bias tee (Anristsu K252) at the mixing stage couples the low frequency line to the main drive line. The return line from the sample stage contains two cryogenic circulators (Quinstar QCY-050100CM0) to isolate any spurious noise signal from the return line. Nb-Nb coax cable connect the sample stage to the 4K stage. The signal on the return line from the sample is amplified using a low noise HEMT

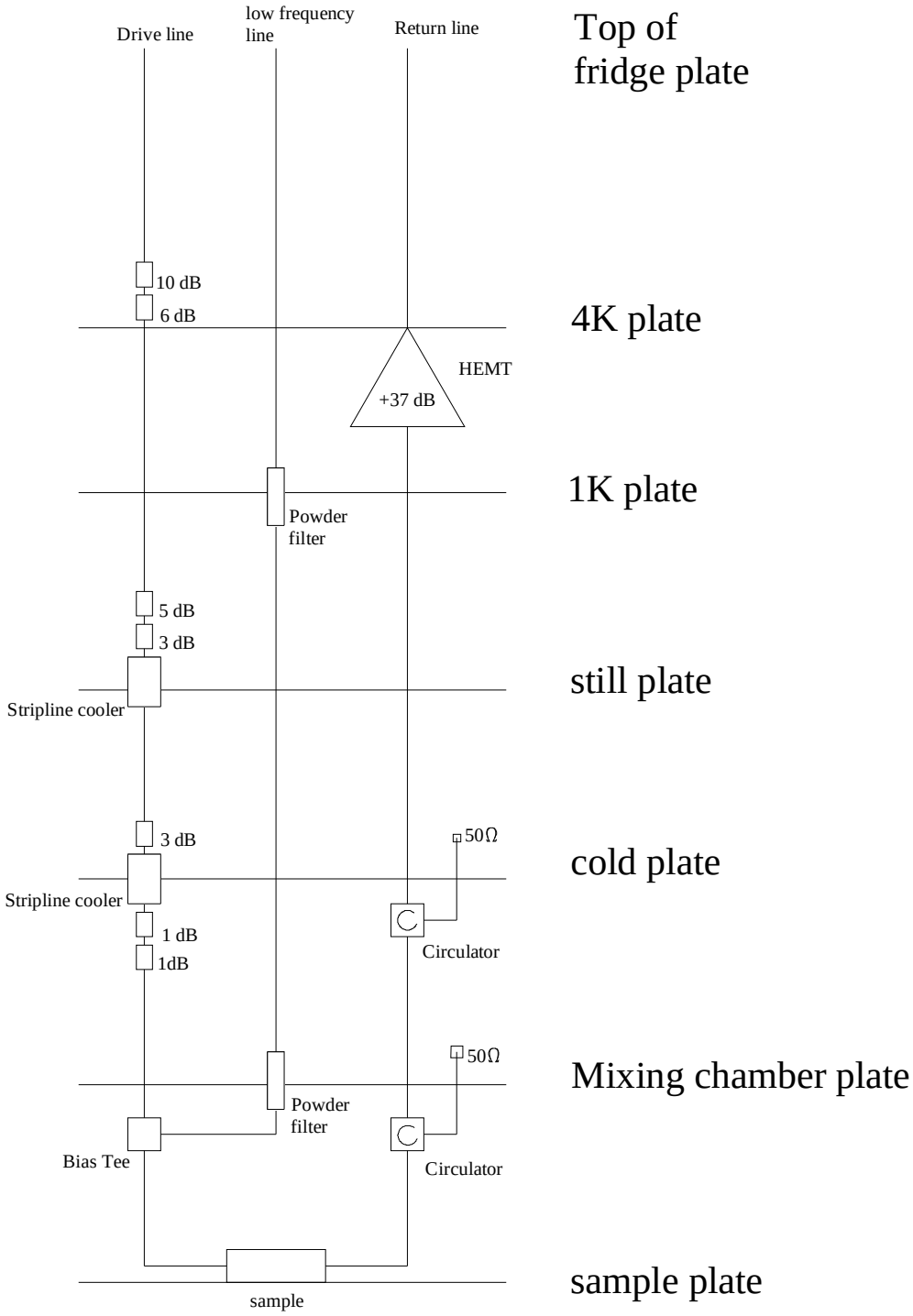

Figure 4.4 Schematic wiring diagram of fridge

amplifier (CITCRYO1-12A, S. Weinreb, CalTech). The HEMT amplifier with a noise temperature of 3.56K and a gain of ~+37dB at 7.5GHz is mounted on the 4K stage. The two circulators mentioned above prevent noise from the HEMT from reaching the sample. UT-63 CuNi-inner, CuNi-outer semirigid coax cable connect the 4K stage to the top of the fridge. The noise floor at the top of the fridge is dominated by the noise floor of the HEMT amplifier. Given a 5dB attenuation the UT63 CuNi-CuNi line between the HEMT and the top of the fridge, we expect the noise floor at the top of the fridge to be $\sim 7.8 \times 10^{-20} W/Hz$ which an equivalent noise temperature of *~5650K.* The internal wiring setup for a typical cool down is shown in Figure 4.4 above. We use a cryoperm magnetic shield can bolted at the cold plate to shield the sample at the sample stage from external magnetic field lines. Magnetic shielding is essential to avoid any field dependent dissipation arising from flux pinning or vortex creation. This type of magnetic dynamics can be enhanced by surface roughness including step edges and also due to the presence of impurities (especially magnetic impurities) in the superconducting thin film. We now turn our attention to the external circuitry used to apply a single and double pump to our NR-SR devices.

4.2.2 Measurement Circuits External to the Fridge

The circuitry at the top of the dilution fridge for measuring S_{21}, the transmission coefficient, and searching for the NR frequency of the NR-SR device is similar to that of the 1K set up in section 4.1.1 and 4.1.3. Once the NR frequency has been determined, we use the single pump circuit below to characterize it at *<1K* temperature. We routinely measure the S21 and power handling of the NR-SR to monitor any changes in dissipation of the SR over time. Below we describe the main measurement set up used for the single and double pump experiment.

4.2.2.1 Single Pump Measurement Circuit

The measurement for the single pump circuit is shown below in Figure 4.5. In this dissertation, we will solely focus on NR-SR devices that were made such that the resonance frequency of the SR was *~7.5GHz* and the NR frequency *~5-7MHz*. The primary microwave source used was the Agilent E8257D with a maximum output power of +25dBm and a maximum frequency of 20GHz. This source produces phase and amplitude noise of *~-145dBc/Hz* at *5-7MHz* from the carrier. At +25dBm drive, this will excite the SR to an occupation of more than *100* quanta which is obviously bad for cooling. This phase noise was suppressed using two TE_{011} gold-plated cylindrical copper filter cavities [55]. See Hertzberg's dissertation [37] for a detailed description of a *5GHz* filter cavity. The frequency of the filter cavity is determined by the dimensions the interior of the hollow cylinder of the cavity as well as a quartz tuning rod. The Q-factor is determined by rf coupling loops at the top of the cavity as well as the smoothness of the interior surface of the cavity. At 300K, the filter cavities are dissipative with a low Q of *~15K*. We were able to get reasonable Qs of ~30K by cooling a *7.5GHz* filter cavity down to *77K* in the presence of a helium-4 atmosphere. We were able to get *~20MHz* of tuning using the quartz rod. Connecting a 300K filter cavity in series with a 77K filter cavity improved the Q to *45K*. The insertion loss was about -9dB with an isolation (IL - S_{21}(6MHz)) of about *55dB* at 6MHz from the carrier. Given the low insertion loss, we connect a power amplifier (Mini circuit, ZVE-3W-83+) at the input of the filter cavities to boost the signal from the source. The amplifier has a gain of ~+35dB and a noise figure of 6.9dB at 7.5GHz. The 20dB total attenuation connected at the input of the amplifier is there to protect the power amplifier but also to reduce the broadband and phase noise from the source. The 3GHz high pass filter at the drive line of the fridge removes any *MHz* signals that could

potentially drive the NR. The return line of the fridge connects to a circulator (DiTom D3C-4080) and then to a MITEQ low noise amplifier (AFS3-04700530-07-8P-4-GW). The circulator prevents any spurious noise signal from the Miteq LNA from entering the fridge through the return line.

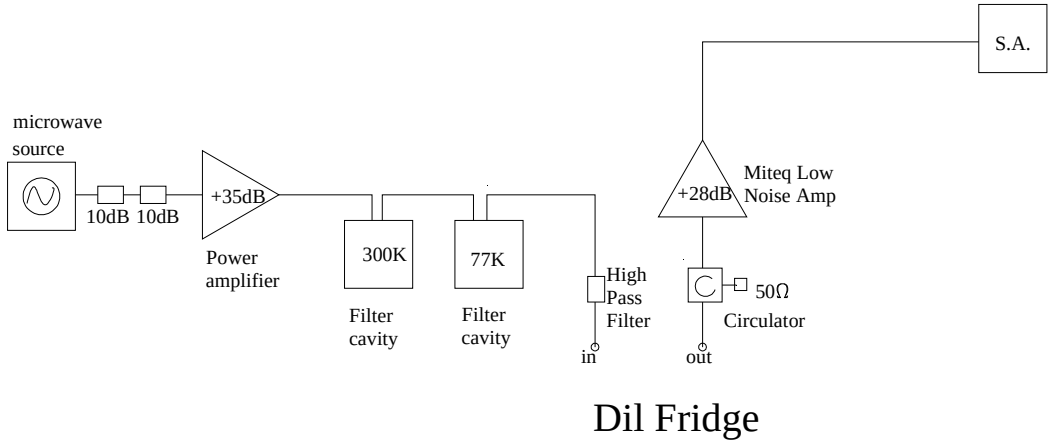

Figure 4.5 Schematic sketch of circuit used for single pump drive

Notice that the noise floor at the input of the MITEQ LNA is dominated by HEMT noise. Low loss coax cables carry the microwave signal to a spectrum analyzer (Agilent N9020A) in the control room. The noise floor at the spectrum analyzer (SA) is still dominated by the HEMT noise as expected. We measured a noise floor of -152dBm/Hz for the SA alone and a noise floor of -142dBm/Hz when the SA was connected to the fridge. The input circuit can be updated as the need arise using directional couplers, power splitters and other microwave components. For instance in studying the SR occupation we inserted a chain of noise injection amplifiers to the input line using a directional coupler. We also used the low frequency line to add *MHz* noise to heat up the NR. In the setup above, all the electronic instruments are

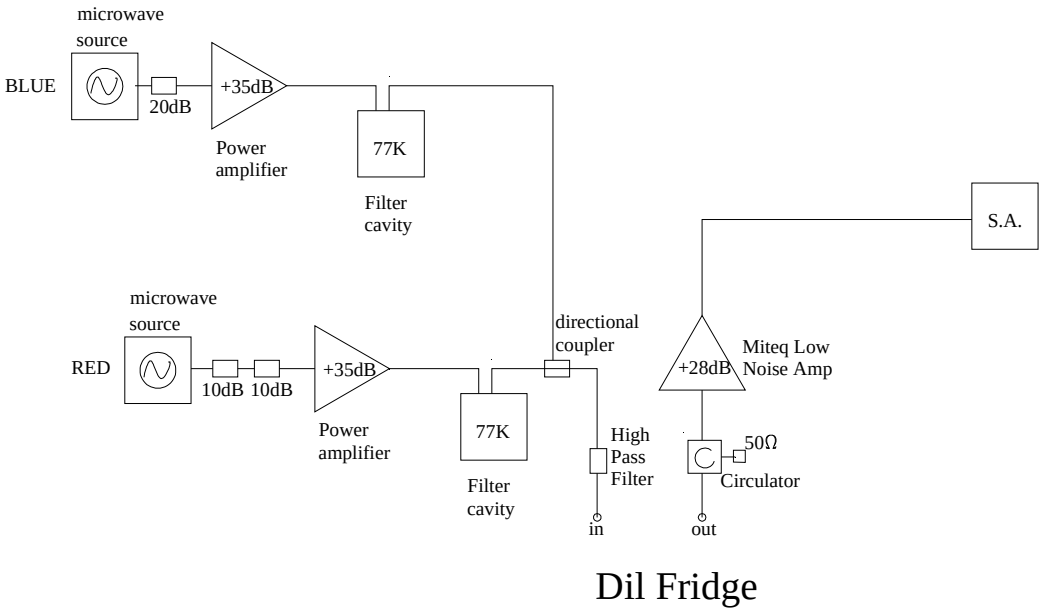

Figure 4.6 Schematic diagram of double pump measurement circuit.

synchronized to a single *10MHz* source (SRS FS725 rubidium standard). Instrumentation inside the shielded room was powered from a dc battery supply.

4.2.2.2 Double Pump Measurement Circuit

The double pump circuit is an addition to the single pump circuit as shown in the Figure 4.6. We used a second Agilent E8257D for the blue drive. Because we mostly drove the blue frequency weakly, we only needed one filter cavity at *77K* in helium-4 atmosphere. At these conditions, we measured a Q of ~32K and an isolation of 32dB at 6MHz for the blue filter cavity. We used an identical power amplifier to boost the signal from the blue source as well at the *20dB* of attenuation to reduce the phase and broadband noise from the source. The two arms of the input circuit were combined using a directional coupler to form a single input signal at the drive port of the fridge. Low loss cables were used between the filter cavity and the top of the fridge to minimize loss. The output section of the circuit is similar to that of the single pump case in section 4.2.2.1 above.

CHAPTER 5: MEASUREMENT METHOD

In this chapter we provide a brief description of how the data of our experiments were collected and analyzed to infer the quantum nature of the NR in the NR-SR. Starting with the measurement circuits of Chapter 4, we were able to characterize the SR and the NR-SR devices using the theory of Chapter 2. Firstly in section 5.1 we describe the characterization of the SR and then in Section 5.2, we discuss the NR in the NR-SR device.

5.1 Characterizing the SR

Using the circuit for the S_{21} and power handling measurement of Section 4.1.1, we can measure the transmission properties of the SR at temperatures far below the transition temperature of the SR. A typical raw data trace is shown in Figure 5.1 where we are measuring the transmission properties of a Nb-SR at 1K. From the S_{21} plot, we can determine, ω_{sr}, the angular frequency and, κ, the linewidth of the SR. We can estimate the insertion loss at the sample, $IL = S_{21}(\omega_{sr})$ from the estimate of the attenuation of the input line and also the transmission at resonance. The internal dissipation of the SR can be estimated using, from Eq. 2.44, the expression

$$\kappa_{int} = \kappa\left[1 - \frac{m+1}{2\sqrt{m}}\sqrt{S_{21}(\omega_{sr})}\right] \qquad (5.1)$$

for $m = \kappa_1/\kappa_2$. By subtracting the internal dissipation from the measured linewidth (loaded dissipation), we can estimate the external dissipation. This can be used to compute the coupling capacitors, $C_i, i = 1,2,$ according the formula $C_i = \sqrt{\kappa_i(\omega_{sr}^3 Z R_L)^{-1}}$. This gives a reasonable check between the designed and the

fabricated devices. We have designed and fabricated high quality SR devices starting with the design formulas of section 3.1.1 and we discuss our findings in Section 6.1.1. The power handling of the SR can be determined by driving the SR at various powers. The SR starts to go non-linear when the current in the center line is larger than the critical current. This is captured in Figure 5.2 where we show the variation of the Q factor with QP_{in} (which is proportional to the power circulating in the cavity) for relatively high Z Nb-SRs. The 125 Ω and 115 Ω Nb devices start to go non-linear when $QP_{in} \sim 1\text{-}2\text{x}10^{-2}$ W. Comparing the power handling of these Nb SRs to previously tested 50 Ω Al SRs shown in Figure 5.3, we see that the Nb SRs are ~100 times better in power handling.

We have also performed temperature dependent measurements on the SR using the set up of section 4.1.2 for 1K measurements and the temperature controller circuit for the dilution fridge for mK measurements. We expect a BCS-like behavior for the Al-SRs below 1K as described in Mazin's PhD dissertation [56] and also [57, 58, 59]. For a BCS superconductor, the density of thermal quasiparticles, n_{qp}, is strongly dependent on the BCS-exponent according to $n_{qp} = 2N_0\sqrt{2k_BT\Delta(0)}\exp[-\Delta(0)/k_BT]$. Where N_0 is the density of state of single-spin electron states at the Fermi level. In the BCS limit, the London penetration depth will also take the same functional form with the same strong exponential dependence. The kinetic inductance, which is the temperature dependent portion of the total inductance of the SR, is proportional to the square of the London penetration depth. The constant of proportionality is determined solely by the geometric dimensions of the SR. Suppose naively that $f_{sr} \propto 1/\sqrt{L}$ and $\kappa \propto 1/L$, then we expect an exponential dependence, of the form $\exp[-2\Delta(0)/k_BT]$, between both f_{sr}^{-2} and κ with temperature. We expect a modified exponential behavior for the Nb-SRs given that Nb is type II superconductor [59, 60, 61]. Figure 5.4 shows

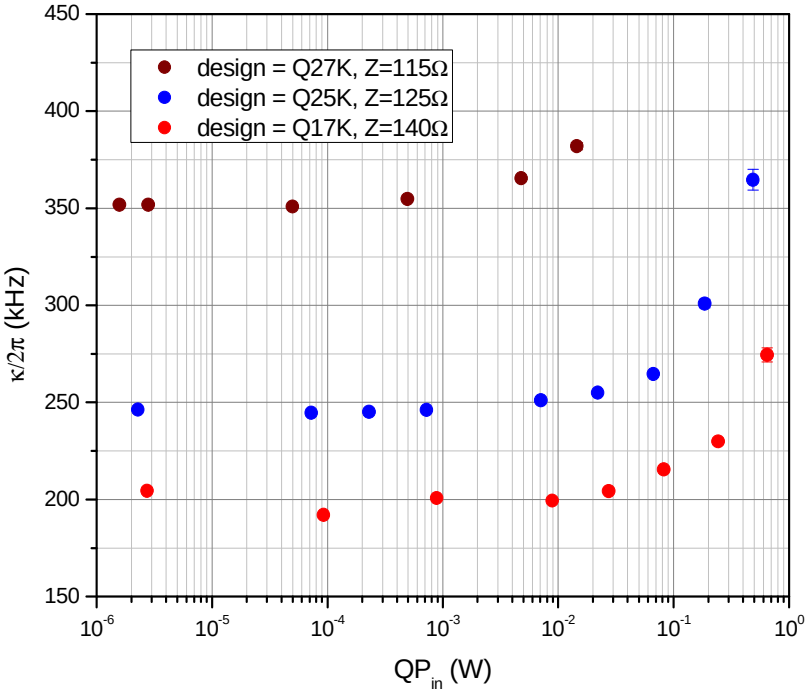

Figure 5.2 Power handling of various high impedance Nb-SR devices measured at ~1K

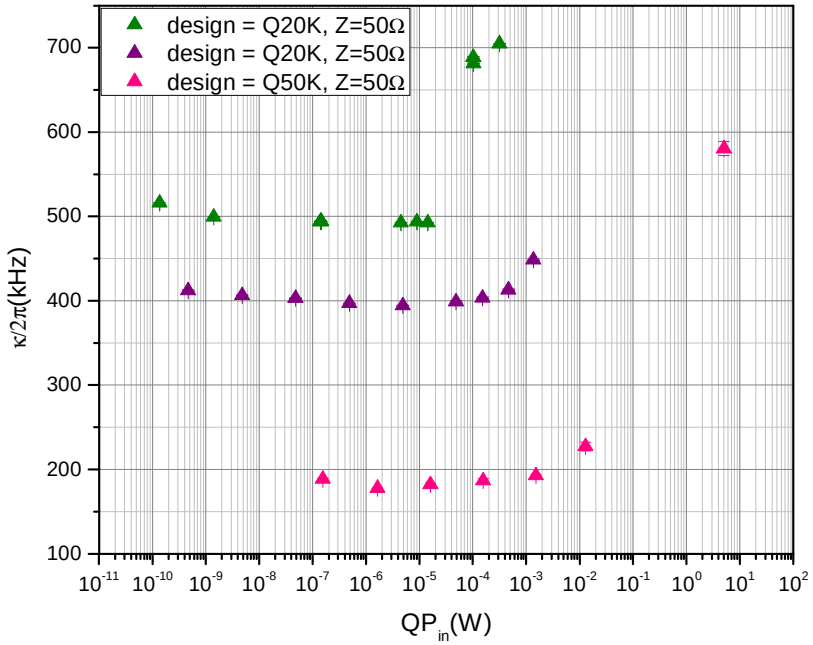

Figure 5.3 Power handling of 50Ω Al-SR measured at 20mK

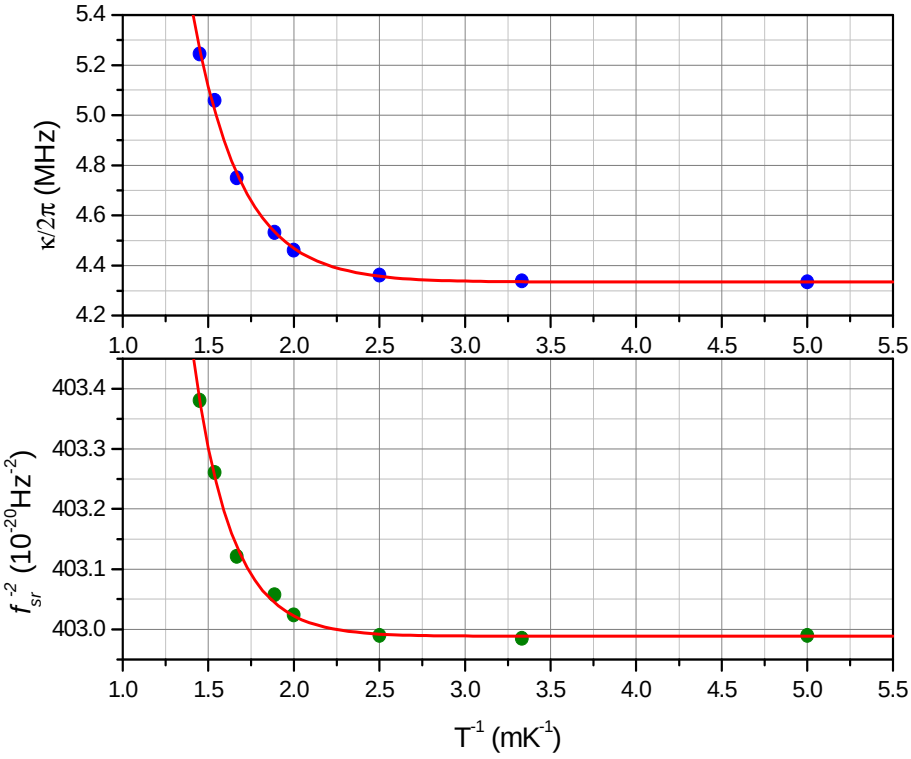

Figure 5.4 Temperature dependent study of a 50 Ω Al-SR. The fit lines are determined from BCS theory for a type I superconductor like Al. The exponential fits give a T_c=1.18K for this Q=1K Al-SR device.

a typical temperature dependence plot for a 50 Ω Al-SR device. The fit lines from BCS theory give a T_c = 1.18K which is within 5% of the bulk value.

5.2 Characterizing the NR of the NR-SR

After characterizing and upgrading the SR devices as described above, we proceeded to fabricating NR-SR devices with optimized SRs. We use the measurement set up of section 4.1.3 to find and study the mechanical resonance at 1K. We typically measure a mechanical resonance between 5.5-6.5MHz for a 30um long, 150nm wide and

160nm thick Al/hs-SiNx NR. The intrinsic mechanical dissipation at 1K is usually around 300Hz. By driving the NR-SR red detuned, we can broaden the mechanical linewidth even at 1K. This can be used to get a rough estimate g, the coupling constant given in Eq. 2.52. The attenuation of the 1K fridge lines cannot be determined to better than 2dB in precision due to losses that exist the rf joint contacts. Thus diagnostic measurements at 1K only give us a good sense of what to expect at *mK* temperatures. We find the mechanics at dilution fridge temperatures using the same set up of Section 4.1.3. At a base temperature of *~20mK*, we consistently see mechanical linewidths of ~15-20Hz for Al/hs-SiNx NRs. Once we determine the mechanical frequency at mK temperatures, we proceed to characterizing the NR using thermal noise.

Using a low power red drive at exactly one mechanical frequency, we measure the mechanical sideband that results from thermal noise and trace it on the Agilent N9020A spectrum analyzer (SA). This measurement can be achieved by using the set up of Figure 4.5 where we connect the microwave source directly to the input of the fridge. At low drive powers, phase noise from the source and cavity noise of the SR are negligible. Figure 5.5 shows a typical power spectrum of the output noise measured by the SA. The noise spectrum measured at the SA, $S_P^{SA}[\omega]$, is given by

$$S_P^{SA}[\omega] = G\left[S_P[\omega] + S_P^{bgd}\right] \tag{5.2}$$

where G is the net gain between the output of the sample and the SA and S_P^{bgd} is the background noise spectrum at the output of the sample. $S_P[\omega]$ is the power spectrum at the output of the sample and is given from Eq. 2.60 by

$$\frac{S_P[\omega]}{\hbar\omega_R} = \bar{S}^R_{\hat{\mathcal{A}}_2}[\omega] \approx \frac{1}{2} + \kappa_2 \frac{\kappa}{\omega^2 + \left(\frac{\kappa}{2}\right)^2}\bar{n}_{sr}^T + \frac{2g^2}{\kappa^2}\frac{P_{out}}{\hbar\omega_R}\frac{\bar{n}_{eff}^R}{\bar{n}_m + \frac{1}{2}}S_x[\omega] \tag{5.3}$$

where ω_R is the angular frequency of the red drive and $\bar{n}_{eff}^R = \bar{n}_m - 2\bar{n}_{sr}^T$. P_{out} is

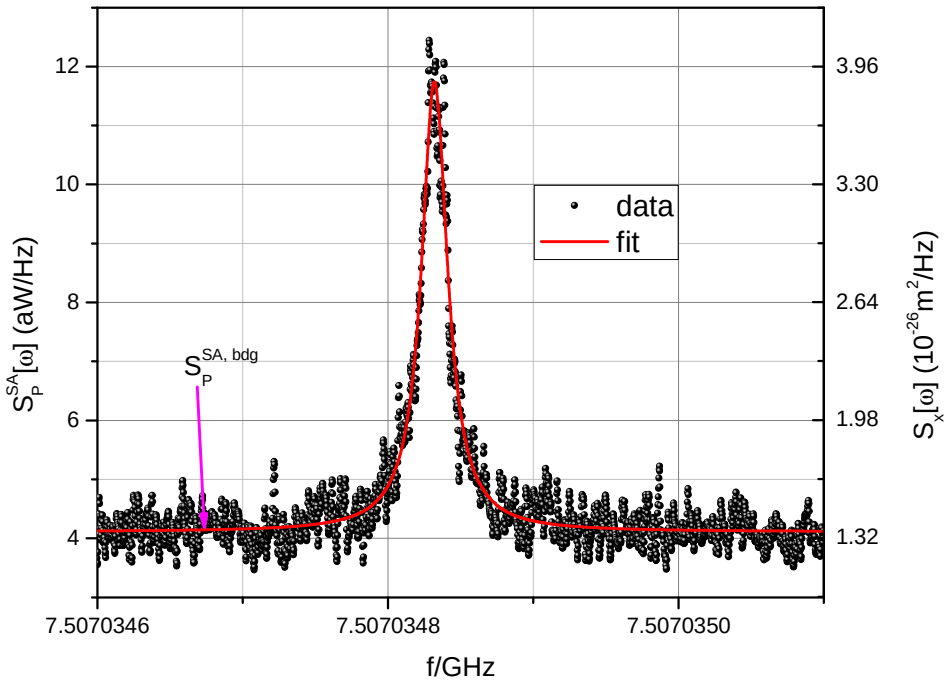

Figure 5.5 Thermal noise response of the NR of an NR-SR device. The Lorentzian fit accurately describes the noise spectrum.

given by Eq. 2.42 and is the average output power at the output (port 2) of the NR-SR. Thus the red transmitted power, P_{tr}, measured at the SA can be written as

$$P_{tr} = G[\omega_R]P_{out} = G[\omega_R]\bar{n}_p\hbar\omega_R\kappa_2 \tag{5.4}$$

We proceed to describe how to extract the gain, G, the dissipation at the output port, κ_2 and the SR occupation factor, $\bar{n}_{sr}^T$ needed in the above equations.

We can estimate the net gain between the output of the NR-SR and the SA from the noise floor measured at the SA, $S_P^{SA,bdg}$(see Figure 5.5). The HEMT amplifier noise dominates the noise floor background at the SA. Accordingly, we write $S_P^{SA,bdg} = G_{amp}K_BT_N^{HEMT}$ (in SI units) where G_{amp}~10^5 is the net gain between

the input of the HEMT and the SA and $T_N^{HEMT} = 3.56 \pm 1K$[†††] (at *7.5GHz*) is the noise temperature of the HEMT. Thus we can write $G = G_{amp}A_o$ (in SI units) where A_o is the attenuation between the output of the sample and the input of the HEMT. This attenuation is determined mainly by two cryogenic circulators (see Figure 4.4). Using previous insertion loss measurements of these circulators at *4K*, we estimate $A_o = 0.83$ (in SI units). We have empirically observed that the gain varies with frequency possibly due to resonances resulting from the fridge line. It is important to correct for this frequency dependence during data analysis especially for high power measurements with broad linewidths. This is achieved by first masking the cavity

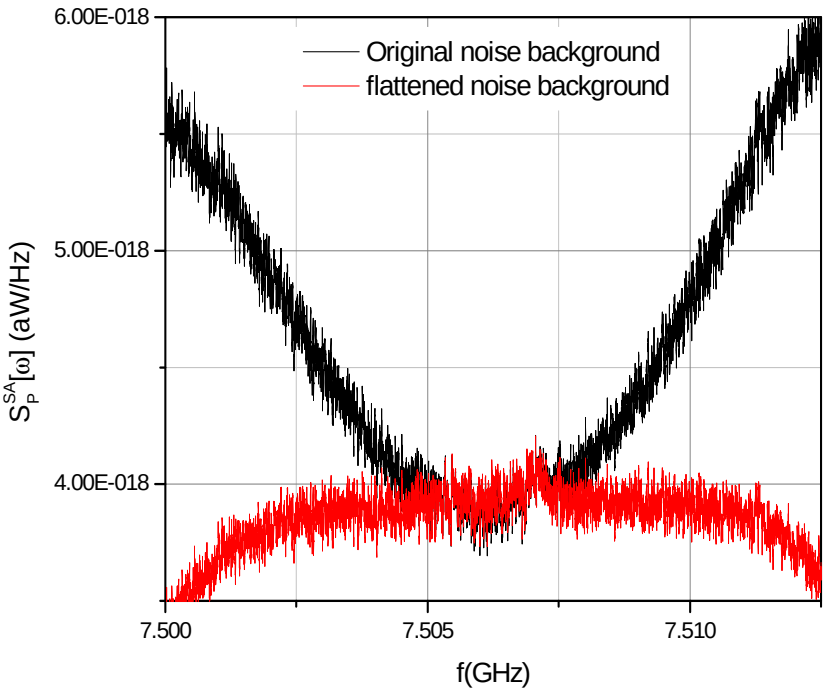

Figure 5.6 Wide span spectrum showing frequency dependence of gain. The flattened spectrum in depicted in red.

[†††] Vendor (S. Weinreb, CalTech) specifications of our CITCRYO1-12A HEMT low noise amplifier

lorentzian, then fitting the noise background near the cavity resonance with a polynomial fit and then finally flattening out the background. Figure 5.6 shows the original noise background plotted together with the flattened background we use in data analysis. Given the description above on how to measure the gain, we proceed to describe the thermal characterization of the NR.

The intrinsic properties of the NR in the NR-SR system can be studied by using a low power red drive at various fridge temperatures. A low drive power guarantees that there are no backaction effects acting on the NR which should be thermalized at the fridge temperature. Thus we are directly measuring the thermal noise response of the mechanics at the fridge temperature. Figure 5.7 and Figure 5.8 show a typical plot of the frequency and intrinsic linewidth of the NR with temperature of the fridge. For this particular device, consisting of an Al/hs-SiNx NR, we find that the frequency of the mechanics is logarithmic in temperature with a linear-log slope of 90.8$\pm$ 1.3. All the NRs that we have measured to date show the same logarithmic dependence between frequency and temperature for a low drive. At moderate temperatures (above ~20K), the frequency of the NR should change with temperature mostly because of the tension created due to the different thermal expansion rates of Al, hs_SiNx and Si. Below ~20K however, the thermal expansion coefficients of most materials saturate (see for instance [62]) and hence the logarithmic dependence at low temperature must be due to a different phenomena. From Figure 5.8, we see that the linewidth, which represents the intrinsic dissipation, is linear with fridge temperature, with a slope of 110.4 $\pm$ 0.3 Hz/K, from the base temperature of the fridge up to a cross over temperature T_{C2}~550 mK. This linear dependence is universal for all the NRs that we have measured to date. We usually observe additional linewidth narrowing below ~150mK resulting from NR ring-up

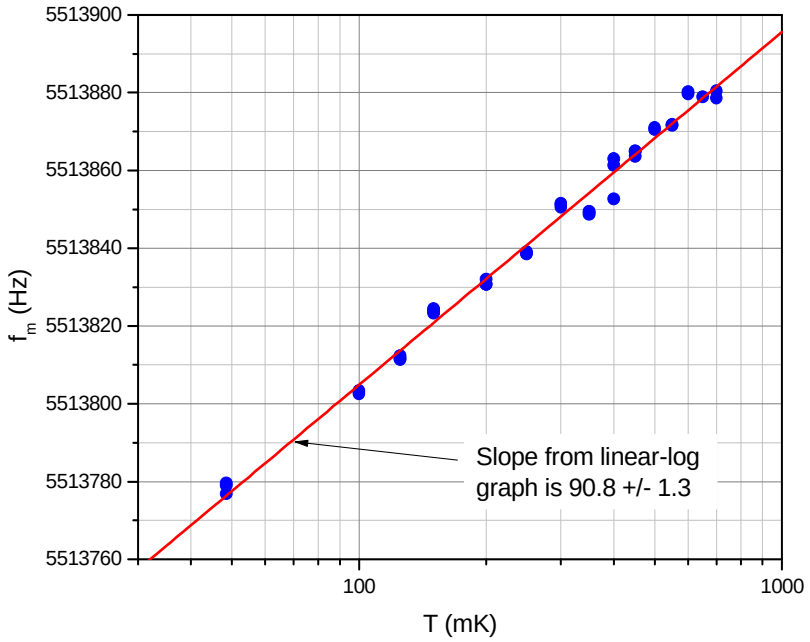

Figure 5.7 NR frequency versus temperature showing logarithmic behavior which predicts the presence of TLS in the NR.

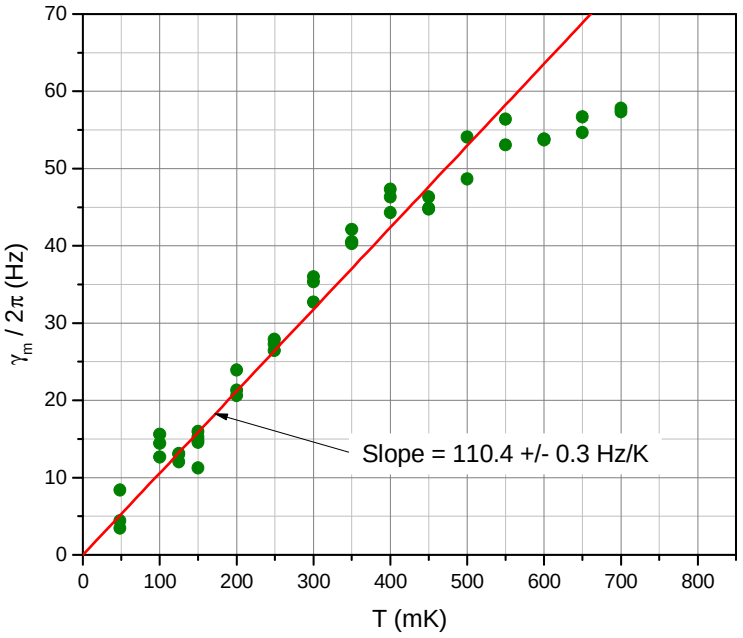

Figure 5.8 The intrinsic dissipation of the NR versus temperature is linear up to ~550mK indicating TLS action. Beyond this roll off temperature, the NR properties are closely described by bulk equations.

effects. The origin of this ring-up effect is not yet completely understood but is equivalent to random "kicking" of the NR by a force bath of up to ~10^{-18}N/$\sqrt{Hz}$ at the lowest temperatures. Above the cross over temperature (550mK) in Figure 5.8, the intrinsic damping continues to increase linearly but with a smaller slope of 39 ± 7 Hz/K. At mK temperatures, intrinsic dissipation can result from thermoelastic, clamping, electron-phonon coupling and/or TLS effects. We expect clamping losses (~ w/l^3) for our 30μm long NR to be small and independent of temperature [63, [64], 65]. Thermoelastic damping is negligible at high frequency and low temperature (see for instance [66]). We can also neglect losses resulting from electron-phonon scattering due to the short mean free path of the electrons (see for instance [67]). This leads us to believe that loss associated with two level systems (TLS) in our NR is the dominant source of damping.

The linear dependence of frequency and linewidth with Temperature is very similar to that reported by [68] where they study TLS in high frequency polycrystalline (metallic) Al NRs which have physical dimensions comparable to the NR of this dissertation. Similar results have also been reported for amorphous insulators [69, 70, 71, 72], amorphous metals [73, 74] and (polycrystalline) metals [75, 76]. At low temperatures, the sound velocity changes logarithmically with temperature according to [77]

$$\frac{\delta\omega}{\omega_{NR}} = Cln\left(\frac{T}{T_0}\right) \tag{5.5}$$

In Eq. (5.5), $C = n_{TLS}\xi^2/E$ is a dimensionless parameter that characterizes the interactions between the two level systems and also between the two level systems and the sound waves. Where n_{TLS} is the density of states of the TLS, ξ is the interaction constant and E is the Young's modulus of the material. For our NR in Figure 5.7, we get C~ 0.2 x 10^{-4} which is consistent with C ~ 10^{-3}-10^{-4} obtained for most armouphous

materials [78]. The intrinsic dissipation of the NR which is characterized by the relaxation rate of the TLS, Γ_{TLS}, is more sensitive to temperature. This has been described in [77] and is given by

$$\gamma_m(T) = \begin{cases} C\Gamma_{\mathrm{TLS}}(\mathrm{T}), & \omega > \Gamma_{\mathrm{TLS}}(\mathrm{T}) \\ C\omega, & \omega < \Gamma_{\mathrm{TLS}}(\mathrm{T}) \end{cases} \tag{5.6}$$

From our measurement, we note that we are in the high frequency regime where $\omega > \Gamma_{\mathrm{TLS}}(\mathrm{T})$ and $\Gamma_{\mathrm{TLS}}(\mathrm{T}) \sim \mathrm{T}$. This gives an interaction time of more than ~ 0.2 µs for temperatures below 550mK of the TLS in the NR of Figure 5.8. In general, the relaxation of the TLS can either be mediated by electrons or phonons or both. For electron mechanisms, the TLS relaxation rate is given by $\hbar\Gamma_{TLS} = 2\pi\ (N_0U)^2 k_B T$ where N_0 is the electron density of state and U is the interaction with the TLS. For our NR at 550mK, we get $N_0U < 0.009$ which is smaller than the value expected for TLS in metals ($N_0U \sim 0.1 - 1$ from [69]). This suggests that the TLS relaxation of our NR is predominantly mediated by phonons (see also [68]). Below 550mK, the phonon wavelength in our Al/hs_SiNx structure should be more than $0.25\mu m$ making our NR beams essentially 1D. Our earlier measurements[‡‡‡] of frequency versus length for various Al/hs_SiNx NRs showed a near-linear phonon spectrum ($\omega \sim \kappa$). Note that this is expected for our high tensioned NRs as given by Eq. 3.10 in the high stress regime (Recall that our NR consists of ~100nm thick Al on < 100nm thick 1200MPa stressed silicon nitride). A linear phonon spectrum (or equivalently a constant phonon density of state) in our 1D system leads to a phonon mediated TLS relaxation rate of $\hbar\Gamma_{TLS} \sim (a^2/w_m t)k_B T$ where a is the effective lattice constant of the 1D NR, w_m is the width and t is the thickness of the NR. The room temperature lattice constant of Al is ~4 Å, that of Si is ~5 Å and the bond length of alpha-Si_3N_4 is ~ 2 Å. Using a ~ 2 - 4 Å as a reasonable value for the effective lattice constant of the bi-layer Al/hs-SiNx

[‡‡‡] From unpublished data of frequency versus length of 10 - 40um long Al/hs-SiNx beams.

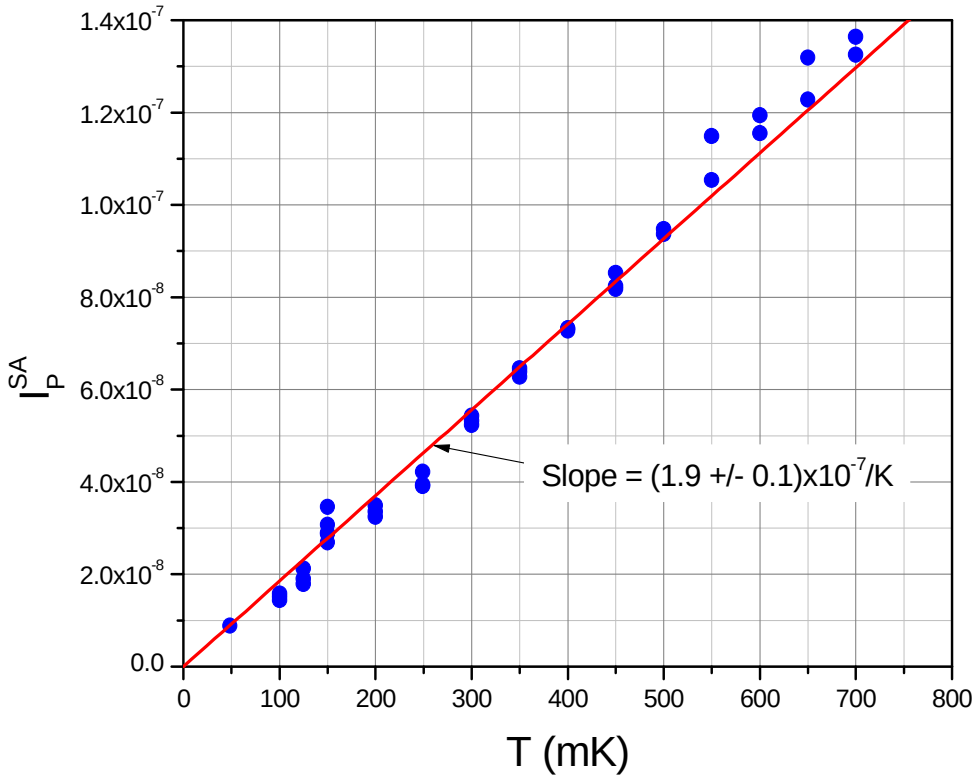

Figure 5.9 Thermal calibration relating temperature (quanta) and the normalized area under the noise spectrum.

structure, we get $(a^2/w_m t)$ ~ 1 – 3 x 10^{-6} for the NR in Figure 5.8. Taking this into account in the above expression for the phonon mediated process leads to relaxation rates that are of the right order of magnitude in the high frequency regime of Eq. 5.6. We thus conclude that phonon mediated TLS in our system are a potential channel for damping. We also believe that they may contribute to the SR occupation that we see in our high drive measurements. For our NR, the TLS most likely originate from the hs_SiNx substrate, the Al-hs_SiNx interface as well as smooth dislocation kinks on the metal of the NR. Isolating and studying TLS dynamic would be the most direct approach to understand and possibly reduce the damping of our NR. In addition, studying the effect of superconductivity on the TLS relaxation rates as well as the

interaction of TLS with the photons (and other noise sources) inside our SR could shed light on the uncharacteristic SR occupation that we observe.

We now turn our attention to the calibration of the thermal noise of the NR. At low drive powers, we can make the approximation $\bar{n}_{eff}^{R} \sim \bar{n}_{m}^{T} \gg \bar{n}_{sr}^{T}$ in Eq. 5.3 to write

$$\frac{S_P^{SA}[\omega]}{P_{tr}} = \frac{G[\omega_{sr}]S_P[\omega]}{G[\omega_R]P_{out}} = \frac{G[\omega_{sr}]}{G[\omega_R]}\frac{2g^2}{\kappa^2}S_x[\omega] \tag{5.7}$$

Integrating Eq. 5.7, we get

$$I_P^{SA} = \frac{G[\omega_{sr}]}{G[\omega_R]}\frac{4g^2x_{zpf}^2}{\kappa^2}\bar{n}_m^T \approx \frac{G[\omega_{sr}]}{G[\omega_R]}\frac{2g^2}{\kappa^2}\frac{k_B}{k_{eff}}T_m \tag{5.8}$$

where $I_P^{SA} = \frac{1}{2\pi}\int_{-\infty}^{+\infty} S_P^{SA}[\omega]/P_{tr}\, d\omega$ is the area under the lorentzian noise spectrum divided by the transmitted power measured at the SA, k_B is the Boltzmann constant, k_{eff} is the effective spring constant and T_m is the temperature of the NR. Eq. 5.8 shows how the NR follows the equipartition theorem and can be used to determine the thermal calibration[§§§]. By measuring the area under the noise spectra for various fridge temperatures, we can determine the calibration between the measured noise spectra and the number of quanta in the NR. Figure 5.9 shows a sample plot of I_P^{SA} for various fridge temperatures. The slope calibrates the area under the noise spectrum to the number of thermal quanta in the NR and hence to the NR temperature. If the NR is in thermal contact with the fridge, then the temperature of the NR is given by the temperature of the fridge. This can be used to compute the coupling strength, g, given in Eq. 5.8. We can now use this thermal calibration to determine the NR occupation for any noise spectra as we show next.

[§§§] As expected, this is the same thermal calibration constant obtained for the single blue and for the double pump drives as well. See Hertzberg's PhD Dissertation [37] for empirical thermal calibration measurements for various pump configurations.

The noise spectrum will take the form of Eq. 5.3 as we increase the drive power. Integrating the noise spectrum in the same manner as above, we get

$$I_P^{SA} = \frac{G[\omega_{sr}]}{G[\omega_R]}\left\{\frac{\bar{n}_{sr}^T}{\bar{n}_p} + \frac{4g^2 x_{zpf}^2}{\kappa^2}\bar{n}_{eff}^R\right\} \tag{5.9}$$

The first term in Eq. 5.9 is always negligible as long as $\bar{n}_m^T \gg \bar{n}_{sr}^T$ for low powers and $\bar{n}_p \gg \bar{n}_{sr}^T$ otherwise. These conditions are easily met in our experiment. Eq. 5.9 thus has the same thermal calibration constant as Eq. 5.8 relating the effective number of NR quanta to I_P^{SA} the area under the noise spectrum divided by the transmitted power measured at the SA. Thus the thermal calibration determined at low powers can be used for any power. We now proceed to describe how we estimate the dissipation from the output port and the cavity occupation factor.

To determine the dissipation from the output port, we consider the power in the mechanical sideband from Eq. 5.3 (in its original form given by Eq. 2.60). The power in the mechanical sideband measured at the SA is given by

$$\frac{1}{G[\omega_{sr}]}\int_{-\infty}^{+\infty}\frac{S_P^{SA}[\omega]}{\hbar\omega_R}\frac{\mathrm{d}\omega}{2\pi} = \kappa_2\bar{n}_{sr}^T + \frac{\kappa_2}{\kappa}\Gamma_R\bar{n}_{eff}^R \tag{5.10}$$

where $\bar{n}_{eff}^R$ can be determined from the thermal calibration and $\Gamma_R = \Gamma_t^R - \gamma_m$ from the linewidth broadening data. For any particular dataset of the output spectrum, the first term on the right hand side of Eq. 5.10 can be determined by masking out the mechanical sideband (second term in Eq. 5.10) and computing the area under the remaining spectrum, given the net gain, G, of the return line. Note that the area of the noise power spectrum given on the left hand side can also be estimated using the noise power at the SR resonance. This can be done by making use of the fact that for a lorentzian shaped sideband, $\int_{-\infty}^{+\infty} S_P^{SA}[\omega]\,\mathrm{d}\omega = S_P^{SA}[\omega_{sr}]\,\kappa/4$. We could in principle compute the total integral of Eq. 5.10, subtract off the SR contribution given by the

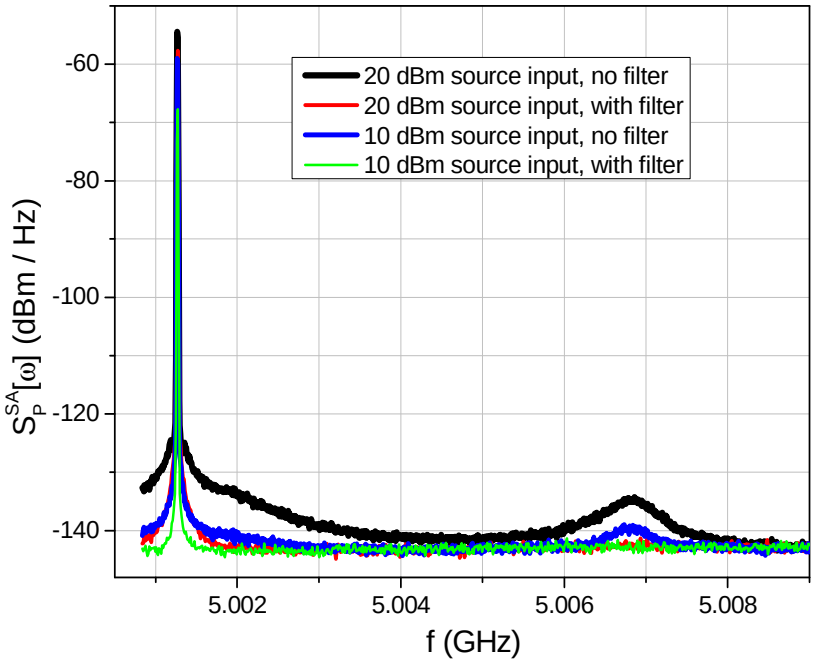

Figure 5.10 Phase noise ring-up of the SR from a red detuned signal. The green and red traces are filtered and do not ring-up the cavity. Taken from [37]

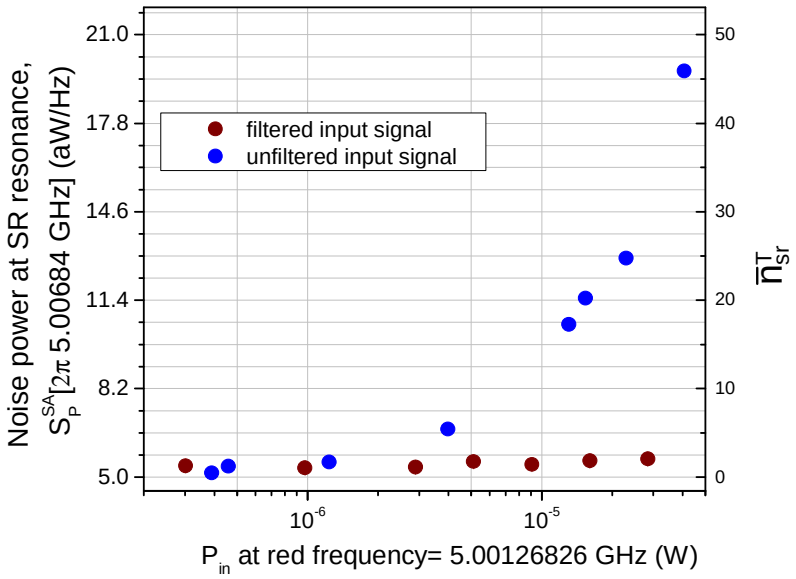

Figure 5.11 Noise associated with the cavity ring-up can be subtracted from the measurement noise floor to determine the number of quanta in the SR. Adapted from [37]

first term determined above and then extract κ_2 from the remainder using the known values of Γ_R and $\bar{n}_{eff}^R$. A more reasonable approach would be to consider the low and moderate power regime for which $\bar{n}_{eff}^R \sim \bar{n}_m$. At these powers, the cavity occupation is negligible and the first term in Eq. 5.10 can be ignored. By considering only the second term, we can now compute κ_2. Since the SR has good power handling properties, we expect κ_{int} to remain constant up to the highest powers where the cavity occupation starts to become important. We can thus determine the SR contribution given by the first term of Eq. 5.10 in the same manner described above from whence we compute $\bar{n}_{sr}^T$. We illustrate this by considering the phase noise ring-up of the *5GHz* device we used in [33] which had a total dissipation, $\kappa = 2\pi\ 494kHz$.

Phase noise inherent to commercial microwave sources will ring-up the SR as predicted by Eq. 2.60, 5.3 as shown in Figure 5.10 [37]. As discussed earlier in section 4.2.2, the phase noise can be greatly suppressed by using high-Q microwave filter cavities. Using low and moderate powers, we were able to estimate the fractional energy emitted at the output port of the SR to be $\kappa_2/\kappa = 0.3$. By subtracting off the noise spectra associated with the SR ring up from the noise floor of the measurement (mostly from the HEMT noise), we determine the number of cavity quanta from Eq. 5.10 as shown on Figure 5.11.

CHAPTER 6: RESULTS AND DISCUSSION

Having described the theory, fabrication, measurement circuits and methods used to study SR and NR-SR devices, we are finally ready to present the key results obtained from our measurements. We report firstly results obtained from 1K characterization measurements of Nb-SR devices in section 6.1. We have fabricated and tested undercoupled and over coupled SR devices at 1K. We have measured SR linewidths as low as 50 kHz for the undercoupled samples at the base temperature of the 1K fridge. This corresponds to a Q factor of a little under ~10^5. We have measured Q's in the range of 2 x 10^4 to 7 x 10^4 for balanced SR devices with identical coupling capacitors. Starting with these empirical results we have designed, fabricated and tested unbalanced SR devices with linewidths as low as 200kHz at 1K. We observe an exponential dependence of the linewidth, the frequency and hence the Q with temperature of the fridge. In section 6.2 and 6.3 we report results for various NR-SR devices. For a single red drive in section 6.2, we have seen substantial NR linewidth broadening from ~15 Hz to an excess of 30kHz for two Al/Nb-NR-SR samples and from ~45 Hz to an excess of 30kHz for a first generation Nb-NR-SR device. For our best Al/Nb-NR-SR device, we were able cool the NR from ~480 quanta to minimum of 3.8+/- 1.3 with ~10^9 pump quanta in the SR. With this low occupation, the NR is supposed to be about 20% of the time in the ground state. Further cooling was impeded by the presence of thermal quanta in the SR and also due to bath heating of the NR. For the Nb-NR-SR device, we observed cooling from ~600 quanta to ~22 quanta at 10^9 pump quanta in the cavity. This low cooling rate, compared to our best Al/Nb-NR-SR device, was due to a marked increased in the bath heating rate despite a lower thermal occupation of the SR for the same number of pump quanta. With our second Al/Nb-NR-SR samples we have performed preliminary

double pump measurements to detect the disparity between the red and blue drive in section 6.3. With the resulting sidebands from the two drives separated we can compare the number of quanta in the two sidebands. We do see that for 10 or more quanta, the occupation of the red sideband compared to the blue sideband follows the expected $\bar{n}_m/(\bar{n}_m + 1)$ behavior. For lower than 10 quanta, where the SR occupation becomes substantial compared to the NR occupation, the measurements results are inconclusive.

6.1 Results of 1K Diagnostic Measurements

We have fabricated and tested SR and NR-SR devices at ~1K using a 1K fridge. At the end of sample fabrication of Chapter 3, the devices are wirebonded unto a sample box and mounted on the sample stage of the fridge. See Hertzberg's PhD Dissertation [37] for a description of the sample box used. The diagnostic tests were mainly 1) to characterize the SR to determine Q and insertion loss and 2) to sift and select good candidates for mK cool down. We have tested both high-Q, balanced and unbalanced Nb-SR devices at 1K. The balanced SR is designed such that the coupling capacitors are identical. In this case there is a probability of $1/2$ for the photon in the SR to leak out from either the input or output port of the SR. The unbalanced SR is designed such that the input (port 1) is undercoupled compared to the output (port 2). For the unbalanced devices of this dissertation, $\kappa_2 = 4\kappa_1$ by design. In that case, there is a $4/5$ chance for the photon leak out through the output port of the SR. Thus, for the same number of pump photons in the SR, the transmitted power of the unbalanced cavity is greater than that of the balanced cavity. The main caveat is that we need to pump harder at the input of the unbalanced cavity to get the same number of pump quanta compared to the balanced cavity. The characterization measurements done at

1K were mostly of Nb-based SR devices. 1K measurements of devices which had Al/Nb junctions (like the Al/Nb-NR-SR devices of section 3.2.2.3) consistently gave relatively low Qs of $<10^4$ for devices designed to give Qs of $\sim 3x10^4$. This dissipation is associated to the presence of normal Al that provides a channel for loss through quasiparticles. Devices with Al/Nb junction usually recover some of their Q at *mK* temperatures in the dilution fridge. Using the design formulas of section 3.11 we have made and tested several all-Nb devices with reasonable Qs in the range $10^3 - 10^5$. For comparison, see for instance [15,16,17] where SR of the similar designs have been reported.

Table 6.1 Measured Qs of balanced SRs with 10.5um long coupling capacitor fingers. The SR impedance and resonance frequency are 115 Ω and 7.5 GHz respectively.

Device	Gap spacing between capacitor fingers /μm	Measured Q /10^3	Effective capacitance /fF
D1	4	23	1.8
D2	5	36	0.8
D3	6	52	0.67
D4	7	70	0.57

Table 6.2 Empirical estimates and measured Qs of unbalanced SRs using values from Table 6.1. The SR impedance and resonance frequency are 115 Ω and 7.5 GHz respectively.

Device	Gap spacing of input capacitor, C_1 /μm	Gap spacing of output capacitor, C_2 /μm	Estimate of loaded Q /10^3	Measured Q /10^3
D5	4	2	11.1	12.2
D6	6	3	25	16.5, 20
D7	7	3.5	32.6	30, 35

a)

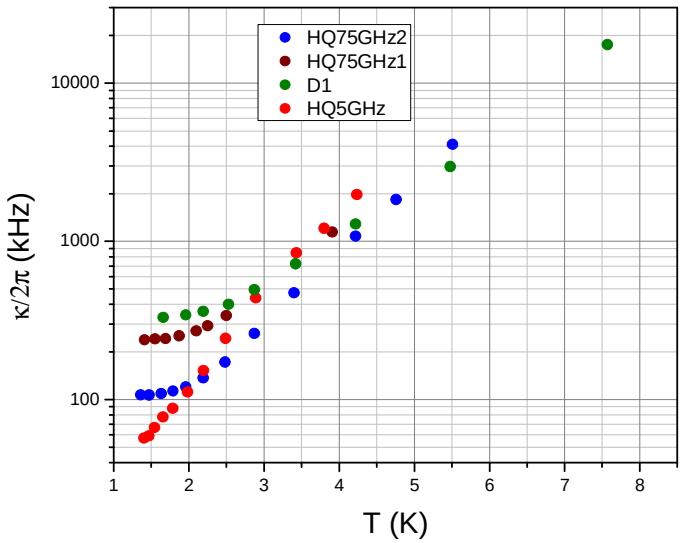

b)

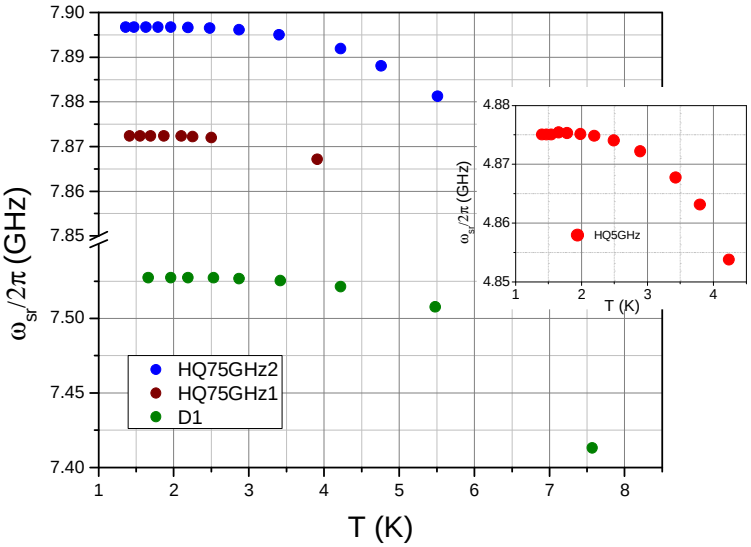

Figure 6.1 a) Linewidth and b) SR frequency dependence versus temperature for sample D1 and three undercoupled samples discussed in text

The coupling capacitors are “C-shaped” interdigitated capacitors with three fingers as seen in Figure 3.4 of section 3.2.1.2. In Table 6.1 we have indicated the measured Q of 4 balanced SR with resonant frequency ~7.5GHz and characteristic impedance (of CPW) of 115 Ohm. We found that at the base temperature of the fridge, the measured Qs were of the same order but smaller in magnitude compared to the estimated Q from the design formula. Given that the measured IL at the input of the SR was small (usually <~1dB), we concluded that this discrepancy was due to the fact that the design formulas did not accurately describe the capacitors of our design. The design formulas, for instance, do not include radiation losses which start to become important for the geometric dimensions of > 50 ohm waveguide [79]. Empirically we observed that the measured quality factor was proportional to the square of the gap spacing between the fingers of the coupling capacitor. Using the measured Qs of these balanced SRs, we were able to estimate the effective coupling capacitance of the input (and hence output), from whence we were able to make empirical design estimates for unbalanced SRs. We found as shown in Table 6.2 that the measured Qs were always within 20-30% of the empirically estimated Q. Internal loading and fabrication-design disparity could account for this discrepancy. The devices shown in Table 6.1 and Table 6.2 were made from Nb from NASA’s JPL at CalTech. These high quality films consistently gave a d.c. transition temperature between *8.8 - 9.5K*. In Figure 6.1 and Figure 6.2 we show the temperature dependence of the linewidth, the frequency, the quality factor and the insertion loss with temperature for the device D1 in Table 6.1 and also three undercoupled SRs. As expected we get an exponential dependence between the frequency and the linewidth with temperature reminiscence of a type II superconductor like Nb. The linewidths start to saturate below 2K for all the SRs. This saturation is determined by the external and the internal loading of the SR. Figure 6.1 shows balanced undercoupled samples including sample D1 of Table 6.1. The

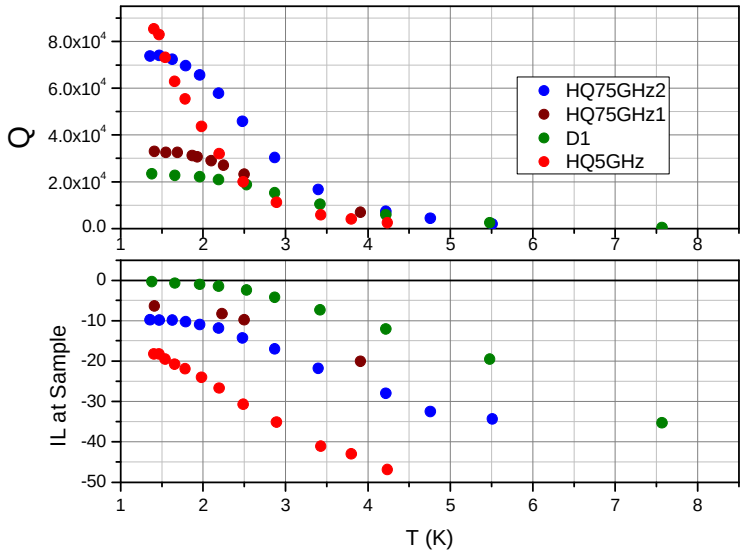

Figure 6.2 Q (upper panel) and IL (lower panel) of undercoupled samples and sample D1. See main text for more discussion

capacitor for the undercoupled samples is a straight gap between the center line of the SR and the centerline of the waveguide external to the SR. This gap is 8µm, 15µm for 115 ohm HQ75GHz1, HQ75GHz2 samples and 5µm for the 50 ohm HQ5GHz sample. These undercoupled samples give high Qs in excess of $3x10^4$ with IL < -5dB at the sample at the sample as shown in Figure 6.2. The unbalanced SR in Figure 6.3 and Figure 6.4 show that the loaded Q saturates below 2K at values determined from the measured Q of D1 and the other devices, D2, D3, D4 of Table 6.2. Based on these promising diagnostic results, we proceeded to fabricating SR devices of desired Q (e.g. D7 to get Q = 30K) that were later coupled to a NR to make NR-SR candidates for *mK* cooldown.

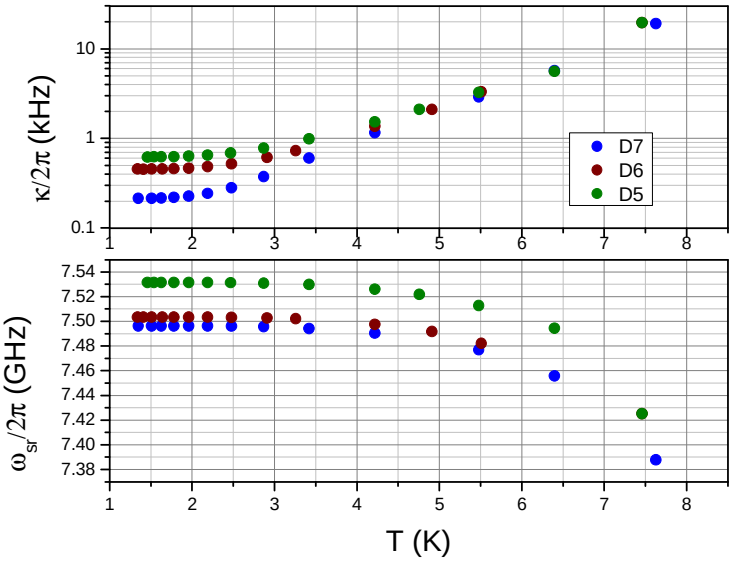

Figure 6.3 Linewidth (upper panel) and SR frequency (lower panel) for unbalanced samples D5, D6 and D7.

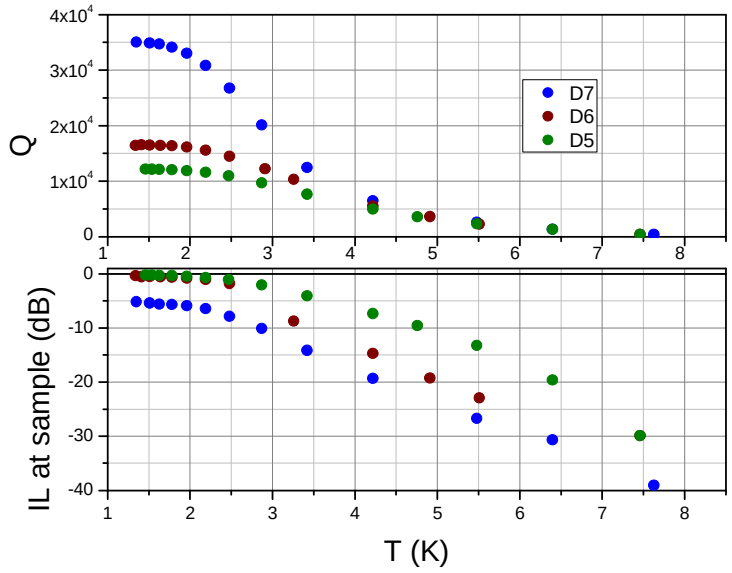

Figure 6.4 Q (upper panel) and IL (lower panel) for the samples of Figure 6.3

In the first part of the project, we used magnetomotive technique to empirically determine the relationship between the mechanical frequency of gated-NRs and their physical dimensions (especially length). Given that the coupling strength depends on the length of the gate, it is advantageous to fabricate long NR. We were able to make $30\mu m$ long beams with narrow gaps of *~75nm* between the beam and the gate. These beams were found to vibrate with fundamental frequency in the range *5.5-6.5MHz*. Longer beams consistently snapped to the gate for the same gap spacing. Given this and the diagnostic measurements for the SR described above, we made a series of NR-SR devices to study the quantum nature of the NR. In section 6.2 we describe the backaction cooling resulting from a single red drive for two such devices. In section 6.3 we turn our attention to the double pump drive with separated sideband measurement results of a third device. Please see Hertzberg's PhD [37] dissertation for backaction heating results from a single blue pump for an all Al-NR-SR device.

6.2 Single Red Pump Measurement Results

In this section, we devote our attention to the backaction cooling results obtained by driving the NR-SR device with a single red tone at $\omega_{sr} - \omega_m$, the red frequency. The measurements were done at *mK* temperatures in a dilution fridge using a measurement circuit similar to the one described in section 4.2.2.1. We report below the measurement results for two NR-SR devices.

6.2.1 Cooling to <5 Quanta with an Al/Nb-NR-SR Device

Using the fabrication process of section 3.2.2.3, we have fabricated a balanced Al/Nb-NR-SR device (Sample1) with the geometric parameters given in Table 6.3 below. In

Table 6.3 Device parameters from geometry and rf measurements of Sample1, the balanced Al/Nb-NR-SR device

Geometry of fabricated device:	
$a = 4\mu m$	width of SR center line
$w = 100\mu m$	distance between SR centerline and ground plane
$t_{Nb} = 345nm$	thickness of Nb on SR
$l_m = 30\mu m$	length of NR
$l_g = 26\mu m$	length of gate of NR
$w_m = 170nm$	width of NR
$t_{SiN} = 60nm$	thickness of hs-SiNx
$t_{Al} = 80nm$	thickness of Al
$d = 75nm$	gap between gate and NR
Derived from geometry:	
$Z_{ch}^{CPW} = 126\Omega$	characteristic impedance of CPW that forms SR
$m = 2 \pm 0.2\ pg$	effective mass of NR
$k_{eff} = 3.2 \pm 0.3\ N/m$	effective spring constant of NR
$x_{zpf} = 26 \pm 2\ fm$	zero-point motion of the NR
Determined from RF measurement:	
$\omega_{sr} = 2\pi\ 7.479048GHz$	SR resonant frequency
$\kappa = 2\pi\ 600kHz$	SR damping rate
$\omega_m = 2\pi\ 6.316\ MHz$	NR resonant frequency
Derived from RF measurement	
$C = 260fF$	effective SR capacitance
$L = 1.7nH$	effective SR inductance
$g = 2\pi\ (84 \pm 5)\ kHz/nm$	coupling constant
$\lambda = 2\pi\ (2.1 \pm 0.7)\ kHz/nm^{-2}$	second order non-linear coupling constant
$[\partial_x C_{NR}(0)] = (5.84 \pm 0.06)aF/nm$	NR capacitance per unit length
$C_{NR}^0 = 438 \pm 30\ aF$	capacitance between NR and SR

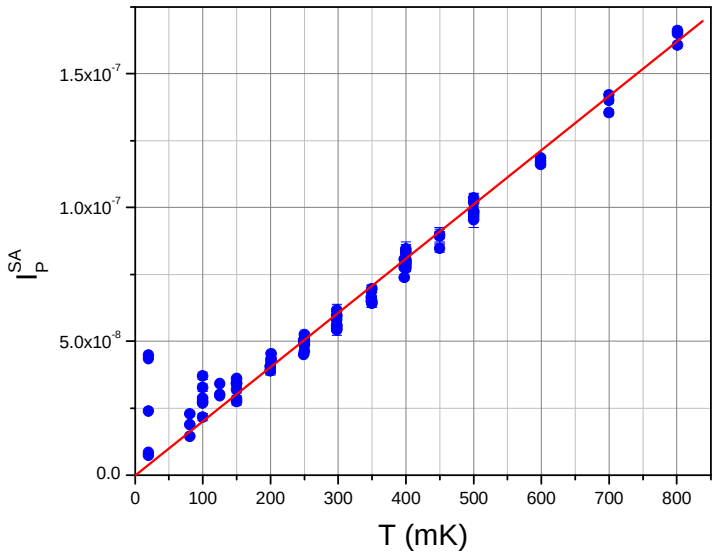

Figure 6.5 Thermal calibration of Sample1. Notice the ring up in the thermal noise at low temperatures <150mK

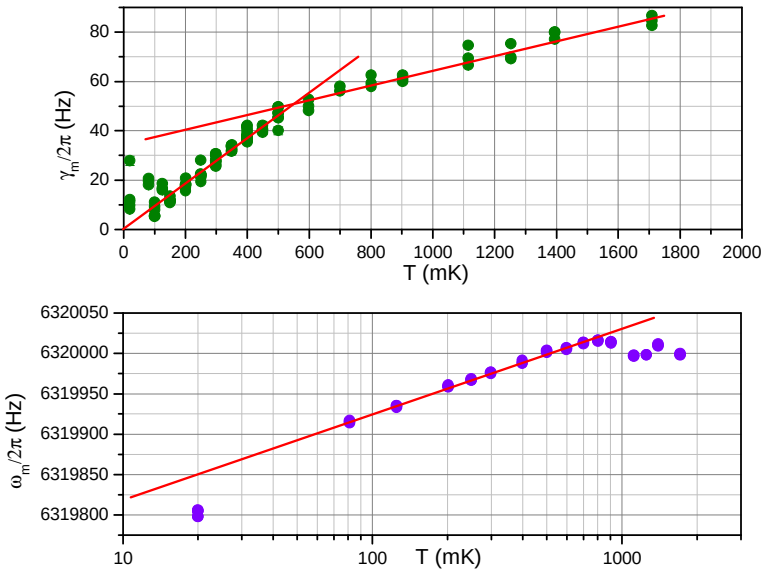

Figure 6.6 NR linewidth (upper panel) and frequency (lower panel) versus temp of Sample1. For the linewidth plot, the sharper slope for $T<T_{C2}$ = 550mK is 100±0.2 Hz/K and the shallower slope representing bulk properties is 30±0.1 Hz/K. The slope from the linear-log frequency plot is 105±1.3 for $T<T_{C1}$ = 800mK.

calculating the parameters derived from the geometry, we assumed a $\pm 5nm$ error in all the dimensions. A separate measurement showed that a 100nm film of Al had a compressive stress of ~ -100MPa when deposited on a 100-Si wafer. We naively estimate a net tensile stress of ~500MPa on the Al/hs-SiNx NR. This stress is large enough to improve the intrinsic Al frequency and hence mechanical Q of the NR. The measurement circuit used for studying the cooling of the NR of this device is similar to that of section 4.2.2.1 but without the power amplifier and the 20dB attenuator in the input line. The RF properties obtained at *mK* temperatures of Sample1 are also given in Table 6.3. By applying a weak red drive at the red frequency at various fridge temperatures and measuring the mechanical sideband at the SA, we obtain the thermal calibration curve for Sample1 as shown in Figure 6.5. The thermal calibration constant with respect to temperature given by Eq. 5.8 is obtained from the slope of the graph to be $1.75 \times 10^{-7}/K$. From this value we estimate the coupling strength $g = 2\pi\ (84 \pm 5)\ kHz/nm$ and hence the capacitance per unit length of the NR, $[\partial_x C_{NR}(0)] = (5.84 \pm 0.06) aF/nm$. Assuming the capacitance is linear to first order with a gap of *75nm*, then $C_{NR}^0 = (438 \pm 30)\ aF$. This is of the same order of magnitude of the value obtained ($\sim 283aF$) when using the physical dimensions of the NR capacitor in the parallel plate formula. At low temperatures (*<150mK*) we see a ring-up in the thermal noise as shown in Figure 6.5. The NR decouples from the fridge at this lower temperatures and appears to be randomly driven by a force bath of up to $\sqrt{S_F} = \sqrt{4k_B m\gamma_m T_m} \sim 10^{-18} N/\sqrt{Hz}$. This low temperature noise has been observed in all the NR-SR devices we have measured to date and also is reported for similar systems [80]. This noise, whose origin is still unclear, restricts the starting temperature of our cooling experiments to *~150mK*. By identifying and minimizing this anomalous behavior, we should in principle be able to get an additional factor of ~7.5 in cooling by starting at a bath temperature of *20mK*. With the NR-SR thermalized at *~150mK*

we proceed to cooling the NR. Figure 6.6 shows the variation of the NR frequency and the NR linewidth with temperature. The mechanical frequency is logarithmic in temperature whereas the linewidth is linear. These plots suggest the presence of phonon mediated TLS in our Al based NR as discussed in Section 5.2. In particular we obtain similar slopes 100 ± 0.2 Hz/K for the linewidth versus temperature plot and 105 ± 1.3 for the frequency versus temperature plot (see Figure 6.6). These values are comparable to those obtained for the NR of section 5.2. Thus we get $C \sim 0.2 \times 10^{-4}$ (see Eq. 5.5 and 5.6) which is reasonable value similar to what we had before in section 5.2. Note that in both cases, the fabrication process of the NR, consisting of Al/hs_SiNx, was similar and hence the consistency in the values above. We also note from Figure 6.6 that the linewidth has a cross over temperature of T_{C2}~550mK (similar to Figure 5.8) whereas the frequency plot has a cross over that T_{C2}~800mK. A cross over temperature is expected when the TLS relaxation rate becomes comparable to the mechanical frequency (see equation 5.6 or any good text on TLS e.g [67-77]). It is not completely clear why the cross over temperature from the frequency and linewidth plots differ. We now proceed to describe the cooling of our NR achieved by increasing the red drive.

The backaction cooling of the NR motion is achieved by increasing the strength of the red drive. Given the thermal calibration, we can now quantify the cooling of the NR as we increase the red drive signal. The noise measured above the HEMT noise at the SA is accurately described by Eq. 2.68 as shown in Figure 6.7. At low drive powers of $< 10^6$ pump quanta where $\bar{n}_{eff}^{R} \approx \bar{n}_m \gg \bar{n}_{sr}^{T}$, the mechanical sideband is a lorentzian peak piercing through the noise background set by the HEMT amplifier. We compute the average mechanical occupation of the NR from the area under the lorentzian peak using the thermal calibration and Eq 5.9. At moderately high

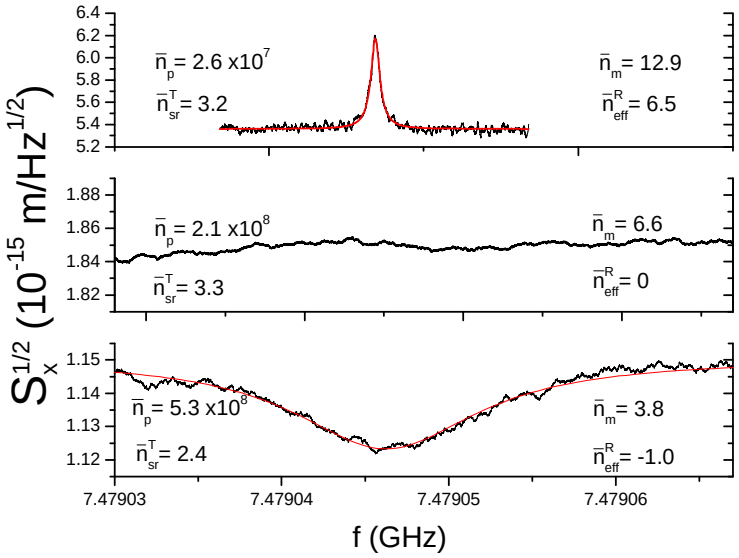

Figure 6.7 Position spectrum of the NR at various pump powers, $\bar{n}_p$. The mechanical sideband is a Lorentzian peak (top panel) at low drive. The sideband goes flat at $\bar{n}_p = 2.1 \times 10^8$ pump quanta due to SR occupation (middle panel). Increasing $\bar{n}_p$ creates a Lorentzian dip for the mechanical sideband at high powers

to very high powers, the SR occupation becomes significant due to the introduction of thermal noise from the dissipative ports of the NR-SR. As discussed in section 5.2, we determine the SR occupation, $\bar{n}^T_{sr}$, by masking out the mechanical sideband and fitting the lorentzian shape of the SR resonance. Or equivalently we determine the SR occupation from the SR noise spectrum on resonance by using the fact that $\int_{-\infty}^{+\infty} S_P^{SA}[\omega]\,\mathrm{d}\omega = S_P^{SA}[\omega_{sr}]\,\kappa/4$. We use the thermal calibration constant obtained above to determine the effective NR quanta, $\bar{n}^R_{eff}$, as given in Eq. 5.9. The actual number of NR quanta is given by $\bar{n}_m = \bar{n}^R_{eff} + 2\bar{n}^T_{sr}$. The linewidth of the NR increases linearly with the drive power as expected. The main cooling result for this device is given in Figure 6.8. Starting from a stable bath temperature of

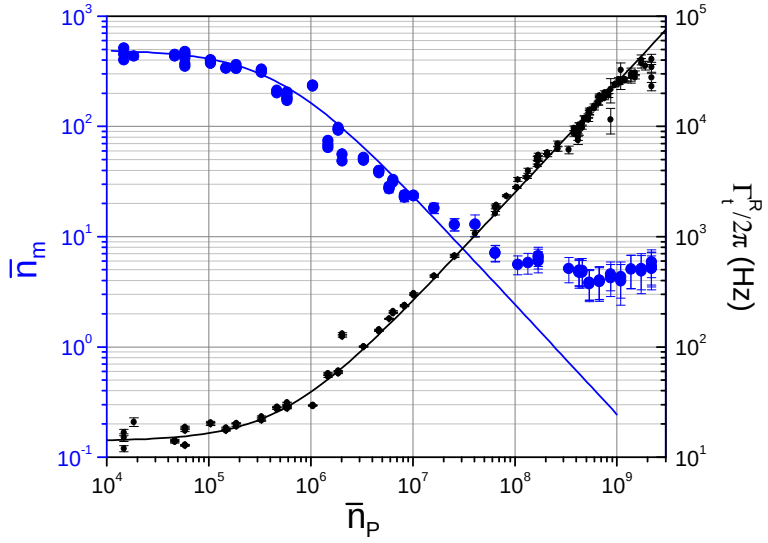

Figure 6.8 NR linewidth broadening and cooling versus pump strength. The solid black line is the linear fit for the linewidth broadening. The blue solid line is obtained by assuming a constant bath temperature and no SR occupation.

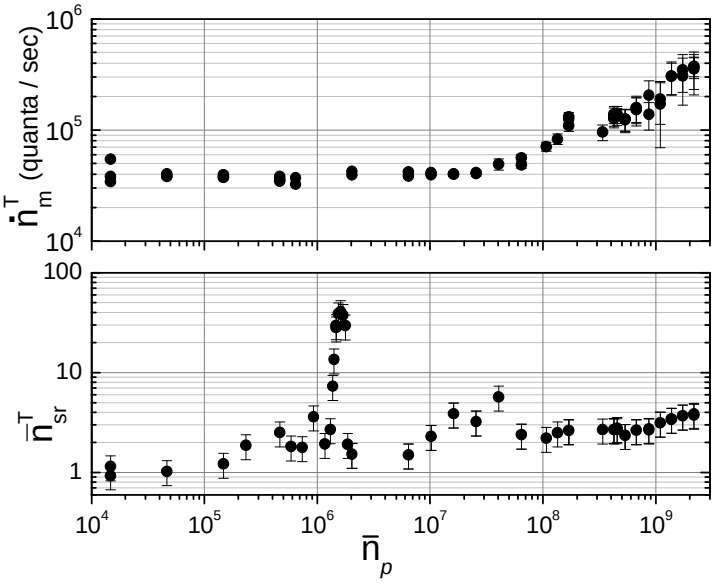

Figure 6.9 NR heating rate (top panel) and SR occupation (bottom panel) versus pump strength. The bath starts to heat the NR above $\bar{n}_p = 3 \times 10^7$ pump quanta.

$146mK$ ($\bar{n}_m^T = 480$) we observe the NR linewidth broaden linearly with pump quanta from as low as $\sim 15Hz$ to an excess of $30kHz$. The minimum NR occupation seen is 3.8 ± 1.3 when the pump power is 5.3×10^8 and the SR has 2.4 quanta in it. For this occupation factor, the probability of finding the NR in its ground state is thus 21%. Being able to achieve cooling below 10 quanta is a major result as it paves the way for future experiments that probe the quantum nature of macroscopic NRs with at least 10^{12} atoms in our case. Cooling the NR further is impeded by two key factors which we address below.

The NR occupation plateaus due to the increased bath heating rate, $\partial_t \bar{n}_m^T = \gamma_m \bar{n}_m^T = \Gamma_t^R \bar{n}_m - \Gamma_R \bar{n}_{sr}^T$ and the presence of quanta in the SR. Figure 6.9 shows a plot of the bath heating rate and the SR cavity occupation versus pump quanta. The origin of these heating effects is not completely understood. The bath heating rate is fairly constant as expected below 3×10^7 pump quanta in the cavity. Beyond this pump power, the bath begins to heat the mechanics. This could be due to the presence of dissipative normal-state quasiparticles and or TLS in the NR at these high powers. The SR occupation shows a spike at 1.5×10^6 pump quanta and also a steady rise at $> 10^8$ quanta. This cannot be due to the phase noise from the source as we expect the two filter cavities inline (as shown in Figure 4.5) to completely filter it. We initially speculated that the spike might be a superconducting transition of the Al-NR when a critical current flows through it. We thus made Nb-NRs which are in principle ~ 200 better in power handling and observed, to our chagrin, that the spike persisted and was at ~ 3-4 x 10^6 as discussed in the next section. In the last paragraph below we discuss the estimates of the external dissipation and the power handling of the SR of this device.

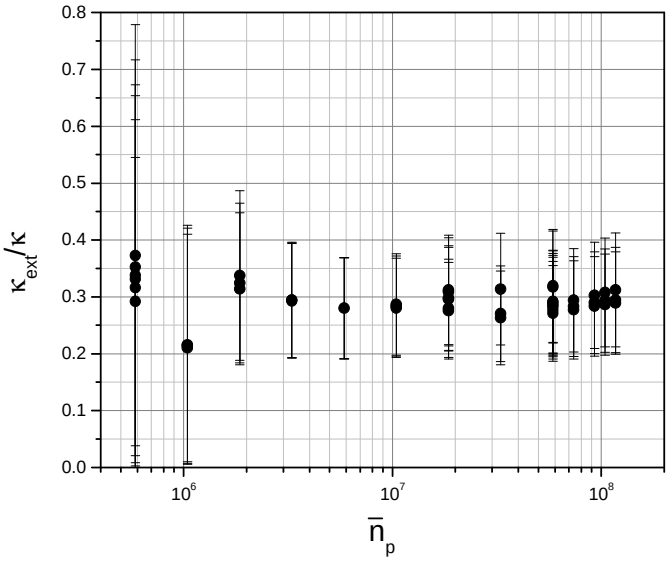

Figure 6.10 Plot of estimate of external dissipation of the SR of Sample1

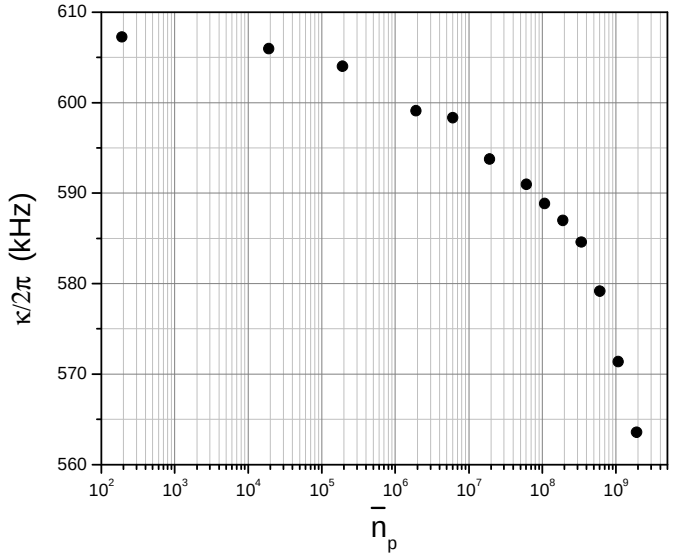

Figure 6.11 Power handling of Sample1 showing linewidth narrow at high pump strengths

Given the noise spectrum data of the cooling plot of Figure 6.8, we extract the external dissipation, κ_{ext}, of the balanced SR using Eq. 5.9. For this device, as shown in Figure 6.10, we got $\kappa_{ext} = (0.28 \pm 0.08)\kappa$ where most of the error quoted is from the error in measuring the gain of the return line to the SA. This means the SR is internally loaded with $\kappa_{int} \approx 0.72\kappa$. This is lower than expected from the design estimated from the 1K diagnostic measurements of section 6.1. One could speculate that the long RIE etches needed to release the Al-NR could go a long way to degrade the metals (Al, Nb), substrate and hence the Q of the SR. Minimizing the internal loss will reduce the SR occupation resulting from thermal noise entering through the internal port of the NR-SR. Figure 6.11 shows a plot of the linewidth of the SR obtained from the S21 measurement for the input powers used for cooling the NR. We observe that the linewidth narrows by ~10% at the highest power compared to the low powers. A direct measurement of the transmitted red power gives a linear dependence to the input red power. The ~10% is small compared to the error from the gain of the return line (30 - 40%) and thus we neglected this linewidth narrowing in analyzing the cooling data above.

6.2.2 Cooling a Nb-NR-SR device

In this section we describe the cooling results obtained for a first generation Nb-NR-SR device, Sample2. The key motivation to make an all-Nb device was to minimize the SR occupation. In principle, an all-Nb device with no contact junctions should have lower internal dissipation and a better power handling than Sample1, the Al/Nb-device described in section 6.2.1 above. Table 6.4 shows the geometric and rf properties of Sample2, the unbalanced Nb-NR-SR device of this section. Compared to the Sample1, the NR of Sample2 is ~3.5 more massive and ~1.5 times farther from the gate. The 150nm of Nb deposited at JPL CalTech was compressive with ~-180

Table 6.4 Geometric and rf properties of Sample2, the unbalanced Nb-NR-SR device

Geometry of fabricated device:

$a = 4\mu m$	width of SR center line
$w = 66\mu m$	distance between SR centerline and ground plane
$t_{Nb} = 150nm$	thickness of Nb on SR
$l_m = 20\mu m$	length of Nb-NR
$l_g = 18\mu m$	length of gate of NR
$w_m = 250nm$	width of NR
$t_{SiN} = 65nm$	thickness of hs-SiNx
$t_{Nb} = 150nm$	thickness of Nb
$d = 110nm$	gap between gate and NR

Derived from geometry:

$Z_{ch}^{CPW} = 115\Omega$	characteristic impedance of CPW that forms SR
$m = 7.3 \pm 0.7\ pg$	effective mass of NR
$k_{eff} = 7.8 \pm 1.1\ N/m$	effective spring constant of NR
$x_{zpf} = 15 \pm 2\ fm$	zero-point motion of the NR

Determined from RF measurement:

$\omega_{sr} = 2\pi\ 7.447625GHz$	SR resonant frequency
$\kappa = 2\pi\ 340kHz$	SR damping rate
$\omega_m = 2\pi\ 5.18835\ MHz$	NR resonant frequency

Derived from RF measurement

$C = 287fF$	effective SR capacitance
$L = 1.6nH$	effective SR inductance
$g = 2\pi\ (47 \pm 7)\ kHz/nm$	coupling constant
$[\partial_x C_{NR}(0)] = (3.6 \pm 0.5)aF/nm$	NR capacitance per unit length
$C_{NR}^0 = 396 \pm 55\ aF$	capacitance between NR and SR

MPa of stress. This would mean that the composite Nb/hs-SiNx NR would have a net ~200MPa of tensile stress. This is ~2.5 times less tensile stress compared to the NR of Sample1. We do measure for Sample2 a lower mechanical frequency but still have a stiffer NR compared to the Sample1. The CPW of this SR is designed to have a characteristic impedance of 115Ω with the output coupling capacitor designed to have two times the capacitance of the input. We used the same measurement procedures as those used to measure Sample1 to study Sample2, the Nb-NR-SR device.

By applying a weak red drive, we obtain a thermal calibration curve as shown in Figure 6.12 of $7.0 \times 10^{-7}/K$. From this thermal calibration, we determine a coupling constant of $g = 2\pi\ (47 \pm 7)\ kHz/nm$ which gave an NR capacitance (assume linear to first order) of $C_{NR}^{0} = 396 \pm 55\ aF$. The anomalous low temperature heating is also evident for the Nb-NR-SR device. Figure 6.13 shows the temperature dependence of the NR linewidth and the frequency with temperature. Again we see a linear dependence of the NR linewidth and a logarithmic dependence of the frequency with temperature. As discussed in section 5.2, this is indicative of phonon mediated TLS in our Nb based NR. We obtain a slope of 290 ± 12 Hz/K for the linewidth plot and a 279 ± 5 for the frequency plot (see Figure 6.13). The slopes are of comparable values as expected and give a C-value (see Eq. 5.5 and 5.6) of C ~ 0.5 x 10^{-4}. This is ~ 2.5 times larger than the value we obtained for our Al based NR (in Figure 5.7 and 5.8 and also Sample 1 in Figures 6.6). Starting with the fact that $C = n_{TLS}\xi^2/E$, we can compare the TLS in our Nb based NR to those in our Al based NR. Given that the Young's Modulus of bulk Nb is ~1.5 times that of bulk Al and assuming that this ratio remains constant at low temperatures, we thus expect the product $n_{TLS}\xi^2$ for Nb to be ~4 times that for Al. Thus our Nb based NR has a lot more TLS which have a larger interaction strength compared to our Al based NR. To make any firm quantitative

conclusions, we need to study the TLS in NR's made of hs-SiNx in this low temperature regime. Note that [72] have shown that hs_SiNx membranes have lower dissipation (Q^{-1}) compared to their low stress counterpart which in turn have lower dissipation (Q^{-1}) compared to a-Si and a-SiO_2. Their hs_SiNx membrane was cooled down to ~2K. Though we can see a somewhat general trend, we cannot make any firm conclusion about the dissipation of hs_SiNx beams below ~1K. We do appreciate from their paper the importance of stress on the dissipation (Q^{-1}) of the membrane. The dissipation of their low stress membrane was consistently >100 times that of their hs_SiNx membrane over the whole temperature range. We do expect therefore that that by improving the tensile stress of our Nb NR of Sample 2 (currently 2.5 times less tensile stress compared to Al NR of Sample 1) we should get less damping (γ_m) for the same 5-6MHz frequency resonator. This can be done quite simply by adjusting the sputtering parameters (e.g the Ar flow rate and or the beam voltage). We also notice, from our SEM study, that the surface structure of good (electrical) quality Nb films consist of "rice-like" grains (possibly 3D grains) packed on the surface compared to the smoother surface of Al. Each rice-like grain is an ellipse with a long axis of ~100nm and a short axis of ~30nm. These rice-like structures may introduce dislocation kinks which is a source of TLS. The stress and the grain structure of the Nb could possibly explain the larger dissipation of our Nb NRs compared to our Al NR. We now turn our attention to describing the cooling result for Sample 2 consisting of a Nb-SR coupled to a Nb-NR.

By increasing the red drive we were able to cool the Nb-NR as expected from a starting temperature of $\sim 150mK$. Firstly, using the cooling dataset, we estimate the dissipation from the output port from Eq. 5.10 to be $\kappa_2 = 0.75\kappa$ which is equivalent to a low internal dissipation of $\kappa_{int} = 0.0625\kappa$. This is ~11.5 times smaller than that of

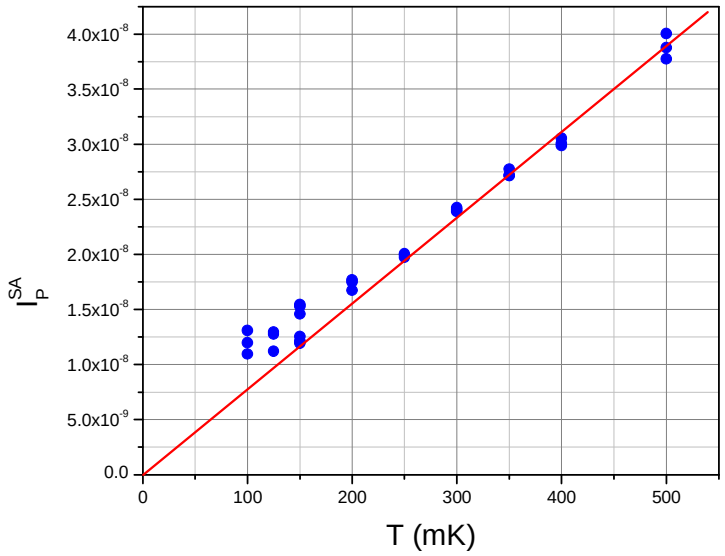

Figure 6.12 Thermal calibration of Sample2

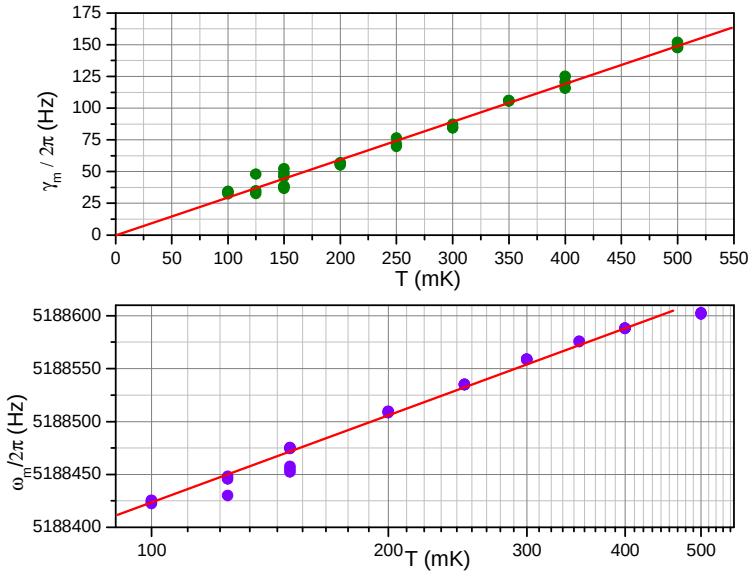

Figure 6.13 NR linewidth (top panel) and frequency (bottom panel) versus temperature for Sample2. The slope of the linewidth plot is 290 ± 12 Hz/K. The slope of the linear-log frequency plot is 279 ± 5.

Sample1. On the other hand, the intrinsic linewidth of the NR was found to be 45-50Hz which is at least 3 times larger that of Sample1. This could be due to the reduced tensile stress of the Nb/hs-SiNx NR. The cooling data trace was taken at $150mK$ where the fridge was stable and the NR was not experiencing the low temperature noise ring-up.

The backaction cooling data for this sample is shown in Figure 6.14 where we have been able to cool the NR from ~ 560 quanta to ~ 22 quanta. The linewidth was found to broaden from $45Hz$ at the low powers to $\sim 30kHz$ at the highest powers. From the linewidth data, we expect a cooling factor of ~ 600. This is ~ 23 times the cooling factor we get from the measured quanta. This suggests that there is an underlying process that is heating the NR in competition with the backaction cooling. To quantify this, we use the fit parameters of the linear linewidth data to simulate the cooling curve for a fixed bath temperature of ~600 quanta (see Figure 6.14). We see a marked deviation of the simulated curve from the cooling data at the high pump strengths. At the highest pump quanta occupation of 10^9 quanta, the NR is heated by an extra 20 quanta despite the fact that there is only about one SR quanta in the cavity. In Figure 6.15 we notice that the bath heating rate starts to increase at ~10^6 pump quanta which is at the same power where extra heating of the NR kicks in. This is worse than Sample1 where bath heating became significant at ~3x10^7 pump quanta. We also observe that there is consistently less SR quanta at the highest power for this Nb device compared to Sample1. For instance, there is only ~1 SR quanta at 10^9 pump quanta for Sample2 compared to ~2 SR quanta for Sample1 for the same pump strength. This could be due to the improved internal Q of the Nb sample. Also evident is the prominent spike between $10^6 - 10^7$ pump quanta which was seen in the previous measurements of Sample1 in Figure 6.9. The origin of this spike is not clear

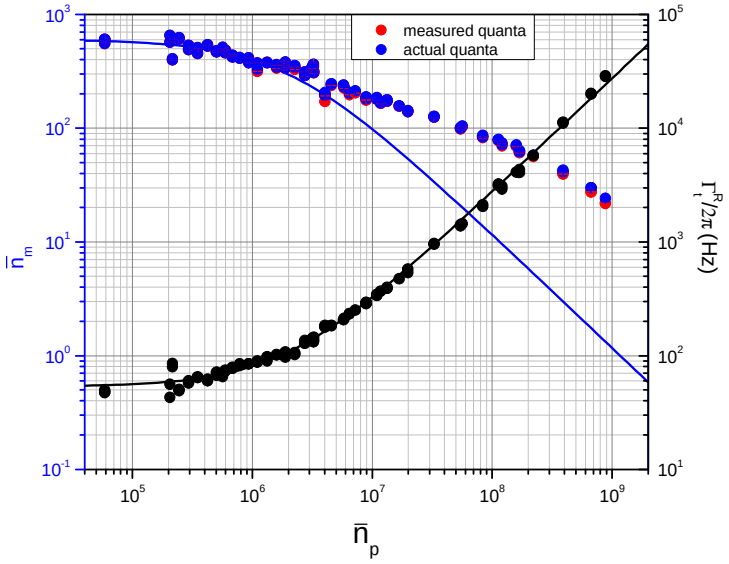

Figure 6.14 NR cooling and linewidth broadening for Sample2. Using the fit parameters of the linear linewidth broadening data, we simulate the cooling curve given by the blue line. Beyond $\bar{n}_p = 2 \times 10^6$ pump quanta, the NR is heated above the cooling curve.

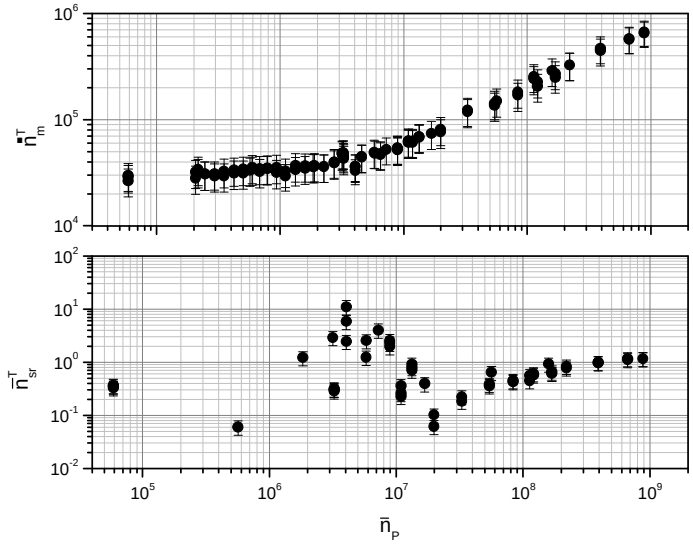

Figure 6.15 NR bath heating rate (top panel) and SR occupation (bottom panel) versus pump strength. The bath heating rate starts to increase at $\bar{n}_p = 2 \times 10^6$ pump quanta. The SR occupation still features a spike at $\bar{n}_p = 4 \times 10^6$.

and could be an artifact of the fridge wiring or spurious noise signal from the Agilent sources not leaving out the possibility of issues with the NR-SR samples. At the highest powers the SR occupation increases and this is consistent with other similar devices. Next generation all-Nb devices for which the NR is less dissipative, has a longer beam with a narrower gap between the NR and the SR and for which the SR resonance is at a higher frequency and still has a high internal Q will go a long way to get better cooling results for Nb-NR-SR.

6.3 Double Pump Measurement Results

We have studied the occupation of the mechanical sidebands resulting from driving the NR-SR at both the red and blue frequencies. In this section we only report findings for the case where the resulting sidebands are separated as depicted in the schematic sketch of Figure 2.12. The overlapped sideband case described in section 2.2.3.2 which can be used to do QND-BAE measurements of a single quadrature below the SQL is a next generation project. Please see Hertzberg's PhD dissertation [37] and [33] for BAE measurement results for an all-Al NR-SR device. In [33] we show BAE measurements of a single quadrature of motion with precision as low as four times the zero-point-fluctuation. The measurement circuit we use for the double pump measurement is described in section 4.2.2.2 which is a modification of the single pump circuit of section 4.2.2.1. We use an unbalanced Al/Nb-NR-SR device with geometric and rf properties given in Table 6.5. We initially describe the measurement results for a single red drive and then later in the section include the results from the double pump drive.

Table 6.5 Geometric and rf properties Sample3, the unbalanced Al/Nb-NR-SR device used for the double pump experiment.

Geometry of fabricated device:	
$a = 4\mu m$	width of SR center line
$w = 66\mu m$	distance between SR centerline and ground plane
$t_{Nb} = 300nm$	thickness of Nb on SR
$l_m = 30\mu m$	length of NR
$l_g = 26\mu m$	length of gate of NR
$w_m = 165nm$	width of NR
$t_{SiN} = 70nm$	thickness of hs-SiNx
$t_{Al} = 100nm$	thickness of Al
$d = 75nm$	gap between gate and NR
Derived from geometry:	
$Z_{ch}^{CPW} = 115\Omega$	characteristic impedance of CPW that forms SR
$m = 2.4 \pm 0.5\ pg$	effective mass of NR
$k_{eff} = 2.9 \pm 0.6\ N/m$	effective spring constant of NR
$x_{zpf} = 25 \pm 2.5\ fm$	zero-point motion of the NR
Determined from RF measurement:	
$\omega_{sr} = 2\pi\ 7.507031GHz$	SR resonant frequency
$\kappa = 2\pi\ 410kHz$	SR damping rate
$\kappa_2 = 0.25\kappa$	External damping through port 2
$\omega_m = 2\pi\ 5.513823\ MHz$	NR resonant frequency
Derived from RF measurement	
$C = 287fF$	effective SR capacitance
$L = 1.6nH$	effective SR inductance
$g = 2\pi\ (56 \pm 7)\ kHz/nm$	coupling constant
$[\partial_x C_{NR}(0)] = (4.3 \pm 0.5)aF/nm$	NR capacitance per unit length
$C_{NR}^0 = 323 \pm 40\ aF$	capacitance between NR and SR

With the device mounted on the sample plate of the dilution fridge, we obtain the thermal calibration by driving weakly at the red frequency as in section 6.2 above. The thermal calibration plots obtained for this device are given in Figure 5.7-Figure 5.9 of section 5.2. We refer the reader to section 5.2 where we have already discussed these plots. Basically, these thermal noise graphs indicate that there are phonon mediated TLS in our Al NR of Sample3. The thermal calibration constant obtained from the slope of the graph of Figure 5.9 is $(1.9 \pm 0.1) \times 10^{-7}/K$ and this gives a coupling constant of $g = 2\pi\ (56 \pm 7)\ kHz/nm$. For a linear capacitance, we estimate the NR capacitance to be $C_{NR}^{0} = 323 \pm 40\ aF$ from the capacitance length density of $[\partial_x C_{NR}(0)] = (4.3 \pm 0.5) aF/nm$. Again, this value is of the right order of magnitude compared to the value obtained from the parallel plate estimate of the NR capacitance. For the rest of the measurements reported, the fridge was set at 150 mK where the NR was in thermal contact with the sample stage. Cooling of the NR is achieved as discussed earlier by increasing the red drive.

The backaction cooling curves for the device is shown in Figure 6.16. The NR linewidth broadens from $\sim 17Hz$ up to more than $60kHz$. The NR occupation on the other hand cools from 560 quanta at the bath starting temperature to ~ 5 quanta at 10^9 pump quanta with 2.5 quanta in the SR. The presence of quanta in the SR combined with the high bath heating rate at high powers as shown in Figure 6.17 impede further cooling of the NR. This has been discussed above for Sample1 and Sample2. The cavity occupation for this sample did not have the prominent spike at $\sim 10^6$ pump quanta seen in Sample1 and Sample2. We do not currently understand the dynamics causing the anomalous spike in the SR occupation. We do observe as before an increase in the number of SR quanta with pump quanta at the highest drive powers.

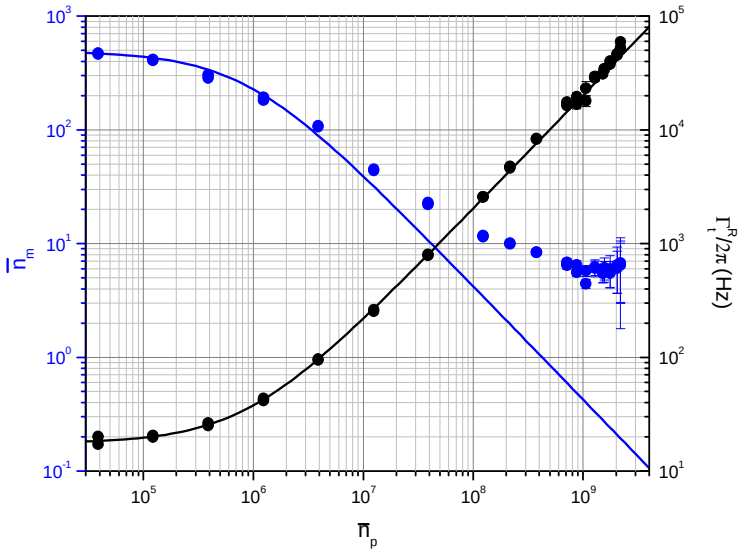

Figure 6.16 Cooling and linewidth broadening plot for Sample3

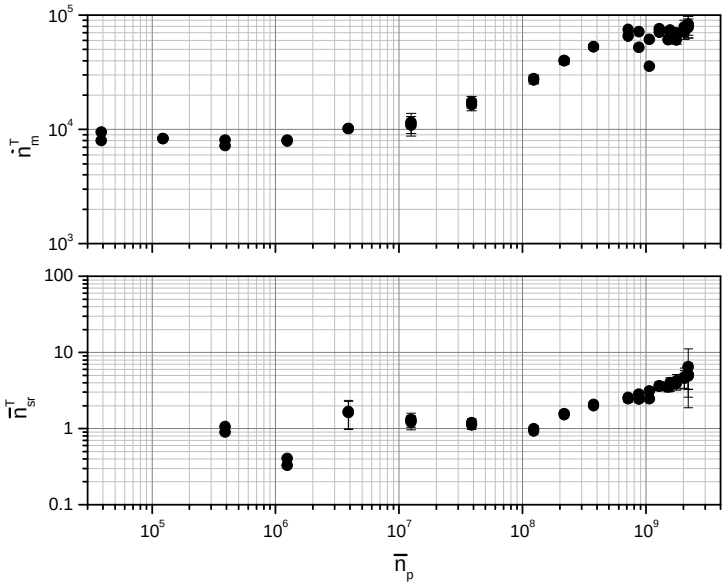

Figure 6.17 NR heating rate and SR occupation for Sample3

Driving the cavity far off-resonance at $\sim 5GHz$ and also at $\sim 250KHz$, we observe a similar behavior of the SR occupation. The phase noise from the source for these lower frequency drive signals were filtered appropriately eliminating the possibility of phase noise heating. The consistent behavior of the SR occupation both qualitatively and quantitatively for the three different drive frequencies let to the logical suspicion that a component on the drive line of the fridge was causing this power dependent behavior. This led us to consider the possibility of ohmic dissipation from the cold NiCr attenuators of the dilution fridge input line. They are only 10s to 100s of microns in diameter and are up to 10s of centimeters in length. This tight tolerance in physical dimension imply that for the highest powers applied, the inner conductor of the attenuators near the sample plate are not well thermalized. Thus as a first attempt to tackle this problem, we swapped the attenuators with lengths of Stainless-Stainless (SS) coax cables of the same attenuation to provide better thermalization. The SR occupation after the attenuator swap was lower by more than a quanta at the highest powers. Evidently, thermalizing the attenuators of the fridge line is absolutely essential in ridding the SR of quanta. This was not a conclusive investigation as we noticed that the SR occupation recovered slightly over the course of two weeks. We are not entirely sure why. Further experiments on bulkier attenuators need to be performed to investigate this phenomenon. Switching gears to the double pump configuration, we discuss below the key measurements and results obtained.

The double pump measurement was achieved using the circuit described in section 4.2.2.2. Figure 6.18 shows the red and blue sideband spectrum measured at the SA resulting from the double pump drives at low and high pump powers. The microwave sources are tuned so that the red sideband is exactly on resonance with the

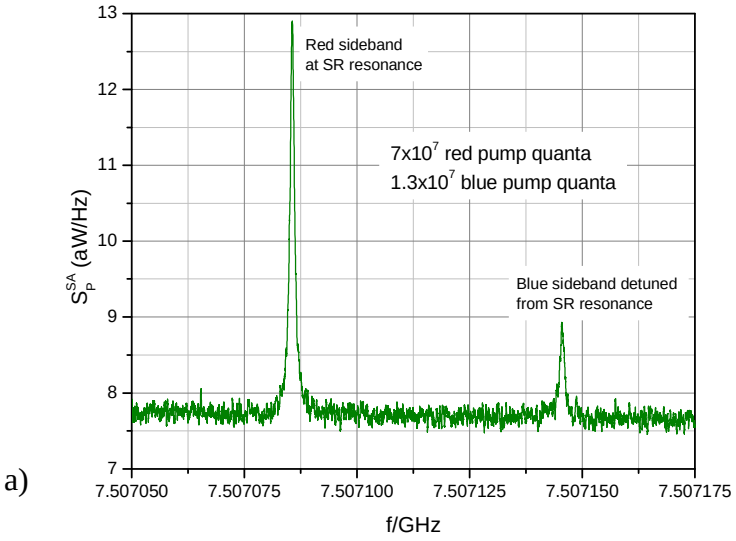

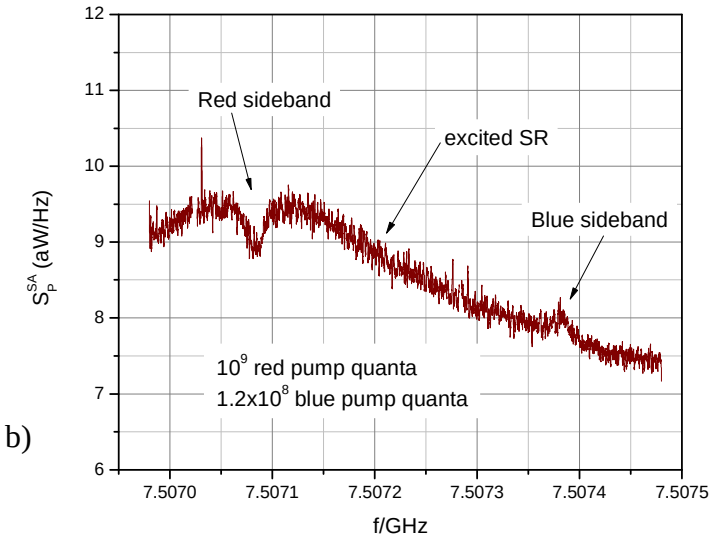

Figure 6.18 Sample spectrums for a) low power and b) high power drive for the double pump configuration. The sidebands are separated by 60 kHz in a) and 300kHz in b)

SR and the blue sideband is to the right (higher frequency) of the SR resonance. At low powers, the SR is not occupied and the sidebands are just lorentzian peaks. At high powers, the occupation of the SR will eventually lead to the inversion of the lorentizian peak of the the red sideband as shown in Figure 6.18 b). While the red sideband can become a lorentzian dip at high powers, the blue sideband is always a lorentzian peak and never inverts. The sidebands were separated by $300kHz$ to avoid interference at the highest power where the broadened linewidth reached an excess of $60kHz$. By maintaining a $\sim 10:1$ ratio in the transmitted power as we increased the strength of the red and blue pumps, we were able to track the number of quanta resulting from the red and blue sidebands. The data was collected in such a way that each double pump dataset was preceded by a single red pump dataset. With the single red pump dataset, we can determine the initial cooling state (linewidth and number of quanta) of the NR and also the number of SR quanta associated with the red drive. This latter quantity is described by the variable $\bar{n}_{sr,R}^{T}$ in section 2.2.3.1. Any increase in SR occupation on application of the blue pump would be used to determine $\bar{n}_{sr,B}^{T} = \bar{n}_{sr}^{T} - \bar{n}_{sr,R}^{T}$ the portion of the SR noise associated with the application of the blue pump. With double pump configuration, we expect to be able to distinguish between the scattering rates of the up-converted and down-converted photons and measure an extra quanta in the blue sideband compared to the red. Given that the blue drive is weaker than the red drive, we expect the backaction effects resulting from the detuning of the blue sideband to be negligible. We also do not expect the weaker blue drive to change the SR occupation appreciably at the highest red drives. Given a typical noise spectral containing the two sideband separated by $300kHz$, we proceed to extracting the number of quanta.

a)

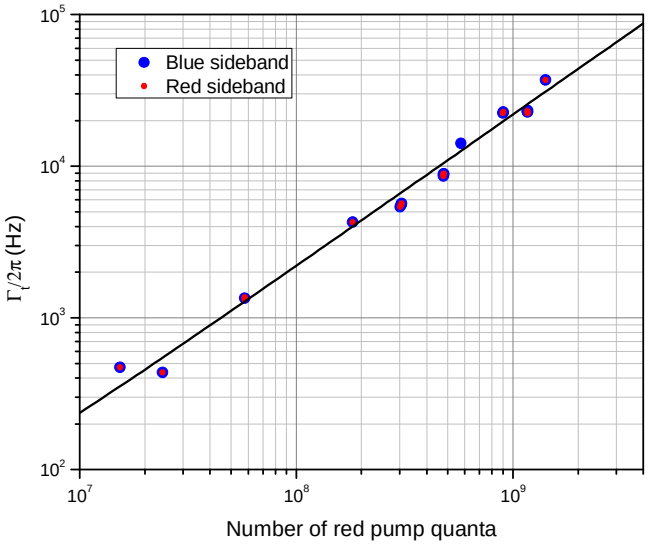

b)

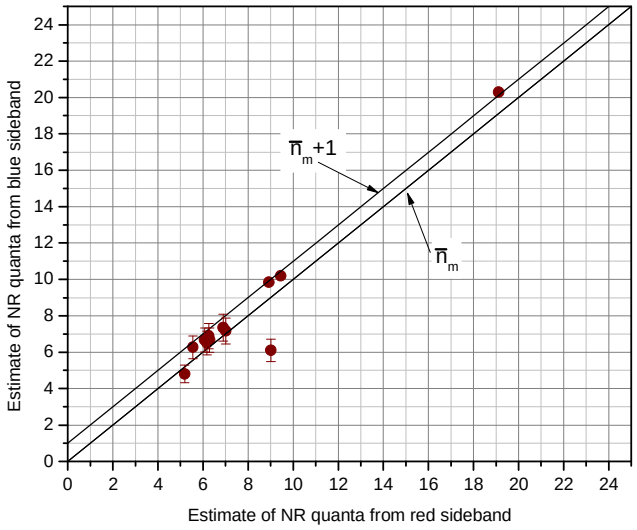

Figure 6.19 a) linewidth broadening corresponding to application of additional blue pump b) resulting estimate of actual quanta represented by blue and red sidebands.

The number of quanta in the red sideband is computed as before in section 6.2.1. and 6.2.2 using $\bar{n}_{sr,R}^{T}$ to determine the actual number of quanta from the effective quanta measured (according to Eq. 2.89 and 2.91). For the blue sideband, we first subtract the SR background near the sideband and then fit the remaining sideband lorentzian response to determine the effective number of quanta in the blue sideband. If there is noise associated with the blue pump, then the effective blue quanta measured directly can be converted to the actually number of quanta associated with the blue sideband by using Eq. 2.90 and 2.92. Figure 6.19 shows the first results for Sample3 where we compare the number of quanta estimated from the red and blue sidebands. The linewidth broadens linearly as expected for the ~10:1 ratio of red to blue transmitted power. For greater than ~10 quanta, where there is less than one quanta in the SR, we clearly see $\bar{n}_m/(\bar{n}_m + 1)$ behavior in the cooling plot. Below 10 quanta, the SR occupation complicates the analysis and this can be seen by the deviation of the points from the $\bar{n}_m + 1$ line of Figure 6.19. The process of estimating the SR occupation involves best estimates of the gain of the return line and dissipation of the SR associated with the output port of the NR-SR. This errors can sometimes be as high as 30-50% compared to a <10% (for < 10 quanta) margin needed to make these precise measurements. With our set-up we can only do a best possible estimate of the resulting occupation associated with the red and blue sidebands. Improving the NR-SR to have better coupling to avoid the complications of dealing with SR occupation and the NR bath heating would be one logical way forward. The alternative would be to stabilize the system and take long averages (of the order of days). This will involve setting up a non-trivial feedback systems to track the frequency and phase of the NR-SR device and the filter cavities. *Better na for go with that strong coupling idea.* In an attempt to further understand the heating effects

a)

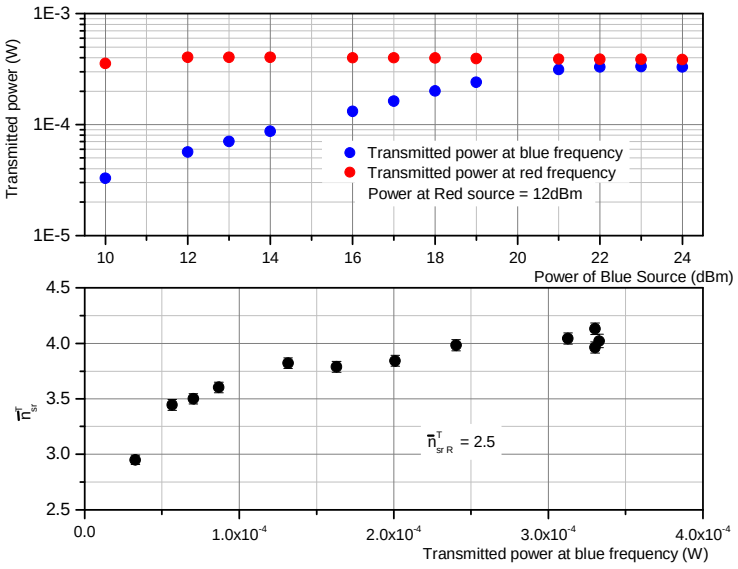

b)

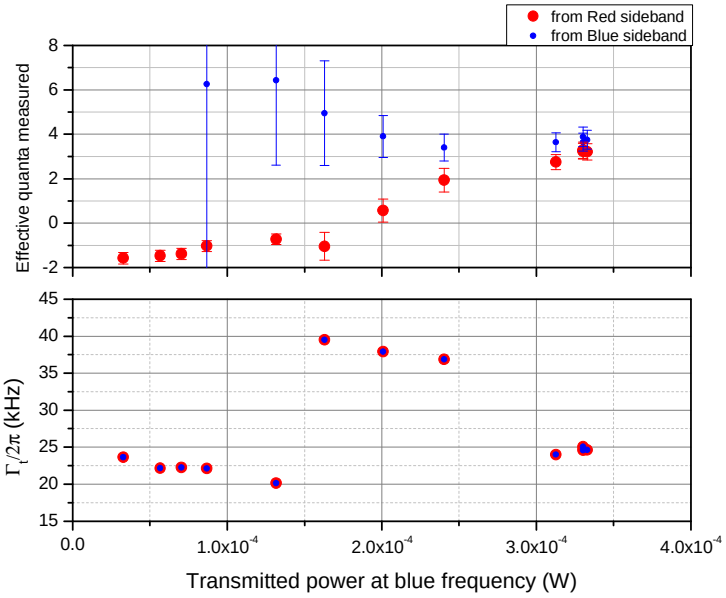

Figure 6.20 a) plot of transmitted power versus power at microwave source (top panel). Plot of SR occupation versus blue transmitted power (bottom panel) b) Plot of effective quanta (top panel) and linewidth (bottom panel) from the red and blue sidebands.

associated with high powers and SR occupation we varied the blue strength for a fixed high power red drive.

Starting with a single red drive that cools the NR to 4 quanta (linewidth of 21.4 kHz, $\bar{n}_p = 10^9$ pump quanta, SR occupation of ~2.5 quanta), we varied the blue drive to investigate the behavior of the NR. The results are shown in Figure 6.20. Firstly we notice from Figure 6.20 a) that the transmitted blue power starts to saturate at beyond $2.4 \times 10^{-4} W$. This could be associated with frequency drifts in the blue filter cavity or saturation of the power amplifier on the blue side of the input circuit. The SR occupation monotonically increased beyond the 2.5 quanta of the single red pump as seen in the bottom panel of Figure 6.20 a). The effective occupation of the red sideband initially increases gradually with the blue drive. Then suddenly increases quickly until it again starts to saturate at the highest powers. The effective blue quanta starts to drop when the pump powers become comparable and seems to plateau at the highest powers as well. The linewidth plot captures this perculiar behavior where it start to decrease as expected as we increase the blue pump. Then all of a sudden at ~1.5x10^{-4}W of transmitted blue power, the linewidth jumps by 2 times its current value and then continues to drop afterwards. This atypical behavior is not yet fully understood and could be due to the competiton between the backaction bath heating , the SR heating and the blue drive dynamical backaction heating of the NR. This could be a potential limit on the possible backaction at high powers.

CHAPTER 7: CONCLUSIONS

The work presented in this dissertation provides a quantum description of the motion of a mechanical device. We have provided a complete quantum mechanical theoretical description of the microwave field inside and outside a SR. We have derived analytical expressions for the transmission and reflection coefficients. We have been able to use the quantum noise approach to calculate the output spectra for various pump configurations for an NR-SR system. The pump configurations include the single red drive which leads to backaction cooling, the single blue drive which leads to back action heating, the double pump drive with separated sidebands and the double pump drive with overlapped sidebands which leads to quantum non-demolition squeezing of the NR. In the derivations, we were careful to include the effects from the SR occupation. The detailed fabrication sequence for our devices has been provided as well as the measurement setups and measurement methods we used in studying these devices.

We have measured bare SR devices at 1K showing Qs just under 10^9 for undercoupled and Qs in the range 2-7x10^4 for overcoupled samples. In the single red pump measurement, we have been able to demonstrate substantial linewidth broadening from 15Hz to >30 kHz. For our best device, an Al/Nb-NR-SR, we have observed cooling from 480 quanta to a minimum of 3.8 +/- 1.3 quanta in the NR. This amount of cooling is sufficient to put the NR in the ground state 20% of the time. This minimum NR occupation is low enough to consider next generation experiments that make use of the quantum nature of the NR; such as the creation of non-classical states like squeezed states, Fock states and entangled states of the NR. The close agreement between the cooling measurements and the backaction cooling theory indicates that

our model theory accurately captures the behavior of our system. We have shown preliminary results of double pump configuration with separated sidebands. We observe that for greater than 10 quanta the NR-SR system behaves like a Raman scatterer with the blue sideband having an extra quantum compared to the red. Below 10 quanta where the SR occupation is important, our results are not completely understood. We believe that radically increasing the measurement times to an excess of ~8 hours per point, to resolve the sidebands (especially the blue sideband), would improve our understanding of the system at this lower NR occupation.

There are a few key additions that I would like to discuss as possible immediate future works. Firstly, the theoretical description in Chapter 2 only considers the linear regime and the weak coupling limit in the equations and analytical formulas derived. Extending the theory to include strong coupling and/or also non-linear effects would come in handy for future devices which operate in these regimes. For instance, in our current measurements, we have seen non-linear effects like parametric amplification in the double pump configuration which destroys the quantum non-demolition (QND) nature of the measurement. Secondly, improving the measurement setup for the double pump with separated sidebands to take longer averages would yield a better comparison to the theory for the lower quanta points. An alternative approach for this measurement would be to use a pulse sequence similar to that of [81] and [82] to monitor the red and the blue sidebands simultaneously. This measurement would involve: preparing the NR in a cool state with <10 quanta, turning off the cooling signal, probing the NR with a signal applied at the SR resonance, measure the resulting red and blue sidebands and determine that there is one more quantum in the blue sideband, and then recooling the NR again to its initial cool state. The above sequence of measurements has to be done in less than $t_1 = (\gamma_m \bar{n}_m^T)^{-1}$, the time

required to exchange one quanta between the NR and the bath. For a typical value of $t_1 = 10\mu s$, and for 1000 points, we estimate that 1000 averages of the red and blue sideband traces can be achieved in ~2hrs. Thirdly, building on the brief description of the QND squeezing scheme of section 2.2.3, the next steps would be to make devices which have NR that can be squeezed below the SQL. In that section, we already provide a few example devices for which we can beat the SQL limit. This measurement will naturally lead to an elaborate set up that would create and detect the quantum squeezed states of the NR. Given the squeezed states, one route of creating Fock (number) states would involve manipulating the squeezed states. This will ultimately lead to the generation of entangled states of the NR. In the mean time, I am pleased to have been part of the physics community that showed quantum mechanics in macroscopic mechanical devices.

APPENDICES: DETAILS OF CALCULATIONS

Appendix 1: Single Red Drive: Backaction Cooling

Appendix 1.1: Equation of Motion for the Single Red Drive

Eq. 2.54, with $\mathcal{E}_2 = 0$, can be solved for the single red drive case using the ansatz $\hat{a}(t) = \hat{a}_r(t)e^{i\delta_R t} + \hat{a}_-(t)e^{i(\omega_m+\delta_R)t}$ where $\delta_R = \Delta_1 - \omega_m$ is the frequency of the red sideband relative to the SR frequency (see Figure 2.6 (a)). The second term of the ansatz represents the drive term at the red frequency which gets to steady states at the drive power. The mechanical sideband in resonance with the cavity resulting from the anti-Stokes scattering process is depicted by the first term. We have neglected the off-resonant sideband in the ansatz above. Substituting this ansatz into Eq. 2.54 and collecting terms that oscillate at the same frequency, we get

$$\partial_t \hat{a}_r(t) = -\left(i\delta_R + \frac{\kappa}{2}\right)\hat{a}_r(t) - igx_{zpf}\hat{a}_-(t)\hat{c}(t) - \sqrt{\kappa}\hat{a}_{rin}(t) \qquad (A.1a)$$

$$\partial_t \hat{a}_-(t) = -\left(i\Delta_1 + \frac{\kappa}{2}\right)\hat{a}_-(t) - i\mathcal{E}_1 - igx_{zpf}\hat{c}^\dagger(t)\hat{a}_r(t) - \sqrt{\kappa}\hat{a}_{-in}(t) \qquad (A.1b)$$

$$\partial_t \hat{c}(t) = -igx_{zpf}\hat{a}_-^\dagger(t)\hat{a}_r(t) - \frac{\gamma_m}{2}\hat{c}(t) - \sqrt{\gamma_m}\hat{c}_{in}(t) \qquad (A.1c)$$

For the two-sided cavity, we see from Eq. A.1*b* that $P_{in,1} = \hbar\omega_1|i\mathcal{E}_1/\sqrt{\kappa_1}|^2$ for $\mathcal{E}_1 \gg \sqrt{\kappa_1}\hat{a}_{-in}$ and this gives the steady sates solution

$$|\langle\hat{a}_-(t\to\infty)\rangle|^2 = \frac{\mathcal{E}_1^2}{\Delta_1^2 + \left(\frac{\kappa}{2}\right)^2} = \frac{P_{in,1}}{\hbar\omega_1}\frac{\kappa_1}{\Delta_1^2 + \left(\frac{\kappa}{2}\right)^2} = \bar{n}_p \qquad (A.2)$$

Where we have made used of Eq. 2.42 to write the solution in terms of $\bar{n}_p$, the average photon population inside the SR due to the single red drive. Thus using the effective coupling strength $\alpha_R = gx_{xpf}\langle a_-(t\to\infty)\rangle = gx_{xpf}\sqrt{\bar{n}_p}$, we can write Eq. A.1*a* and A.1*c* as

$$\partial_t \hat{a}_r(t) = -\left(i\delta_R + \frac{\kappa}{2}\right)\hat{a}_r(t) - i\alpha_R\hat{c}(t) - \sqrt{\kappa}\hat{a}_{rin}(t) \qquad (A.1a')$$

$$\partial_t \hat{c}(t) = -i\alpha_R^* \hat{a}_r(t) - \frac{\gamma_m}{2}\hat{c}(t) - \sqrt{\gamma_m}\hat{c}_{in}(t) \qquad (A.1c')$$

Fourier transforming Eq. A.1 a', c', linearizing the cavity field in the usual way as in Eq. 2.31-2.33, e.g. $\hat{a} = \bar{a} + \hat{d}$, and then collecting the quantum noise terms[****] gives the system of equations

$$\hat{d}_r[\omega] = \chi_{sr}^r[\omega]\left[i\alpha_R\hat{c}[\omega] + \sqrt{\kappa}\hat{d}_{rin}[\omega]\right] \qquad (A.3a)$$

$$\hat{c}[\omega] = \chi_m[\omega]\left[i\alpha_R^*\hat{d}_r[\omega] + \sqrt{\gamma_m}\hat{c}_{in}[\omega]\right] \qquad (A.3b)$$

where $\chi_m[\omega] = 1/\left(i\omega - \frac{\gamma_m}{2}\right)$ is the mechanical susceptibility and $\chi_{sr}^r[\omega] = 1/\left[i(\omega - \delta_R) - \frac{\kappa}{2}\right]$ is the cavity susceptibility for the red sidebands. Eqs. A.3*a* and b and their corresponding Hermitian conjugates can now be easily solved using matrix algebra. The solution gives the SR and the NR field operators inside the cavity as

$$\hat{d}_r = \chi_{sr}^r\chi_{ba}^r\sqrt{\kappa}\hat{d}_{rin} + i\alpha_R\chi_{sr}^r\chi_m^r\sqrt{\gamma_m}\hat{c}_{in} \qquad (A.4a)$$

$$\hat{c} = \chi_m^r\left[i\alpha_R^*\chi_{sr}^r\sqrt{\kappa}\hat{d}_{rin} + \sqrt{\gamma_m}\hat{c}_{in}\right] \qquad (A.4b)$$

where $\chi_m^r[\omega] = \frac{\chi_m[\omega]}{1+|\alpha_R|^2\chi_{sr}^r[\omega]\chi_m[\omega]}$ is the effective mechanical susceptibility in the presence of cavity backaction from the red pump, and $\chi_{ba}^r[\omega] = 1 - |\alpha_R|^2\chi_{sr}^r[\omega]\chi_m^r[\omega]$. Eq. A.4 gives the solution of the field operators inside the cavity for any n-port device. This can be achieved by replacing $\sqrt{\kappa}\hat{d}_{rin}$ in Eq. A.4 with $\sum_{j=1}^n\sqrt{\kappa_j}\hat{\zeta}_j$ and $\hat{c}_{in}$ with $\hat{\eta}$, where $\hat{\zeta}_j$ (given by Eq. 2.45 and 2.46) describes the noise entering the cavity from port j and $\hat{\eta}$ is the noise associated with the intrinsic mechanical damping. Thus we can re-write Eq. A.4 as

$$\hat{d}_r = \chi_{sr}^r\chi_{ba}^r\sum_{j=1}^n\sqrt{\kappa_j}\hat{\zeta}_j + i\alpha_R\chi_{sr}^r\chi_m^r\sqrt{\gamma_m}\hat{\eta} \qquad (A.4a')$$

$$\hat{c} = \chi_m^r\left[i\alpha_R^*\chi_{sr}^r\sum_{j=1}^n\sqrt{\kappa_j}\hat{\zeta}_j + \sqrt{\gamma_m}\hat{\eta}\right] \qquad (A.4b')$$

In the NR-SR system of this work, we limit ourselves to only three ports by taking $j = 1,2,I$. For non-zero equilibrium temperature, the noise operator $\hat{\eta}$ is given by

[****] The classical terms simplify to the same expressions of Eq. 2.37, 2.39, 2.40, 2.42, 2.43, 2.44 of section 2.1.3

$$\langle \hat{\eta}^{\dagger}(t)\hat{\eta}(t')\rangle = \bar{n}_m^T \delta(t-t') \tag{A.5a}$$

$$\langle \hat{\eta}(t)\hat{\eta}^{\dagger}(t')\rangle = (\bar{n}_m^T + 1)\delta(t-t') \tag{A.5b}$$

where $\bar{n}_m^T$ is the number of thermal quanta in the intrinsic bath coupled to the NR. Using Eq. 2.21 we can write Eq. A.5 in frequency space as

$$\langle \hat{\eta}^{\dagger}[\omega]\hat{\eta}[\omega']\rangle = \bar{n}_m^T 2\pi\delta(\omega+\omega') \tag{A.6a}$$

$$\langle \hat{\eta}[\omega]\hat{\eta}^{\dagger}[\omega']\rangle = (\bar{n}_m^T + 1)2\pi\delta(\omega+\omega') \tag{A.6b}$$

Appendix 1.2: Output Spectrum for Red Drive

For the two-sided cavity, the output microwave field, $\hat{\mathcal{A}}_q$, leaving port q, is given by

$$\hat{\mathcal{A}}_q = \hat{\zeta}_q + \sqrt{\kappa_q}\hat{d}_r \qquad\qquad q = 1, 2, I \tag{A.7}$$

In particular, the microwave field leaving port 2, the output port can be written in frequency space with the help of Eq. A.4a' as

$$\hat{\mathcal{A}}_2 = \hat{\zeta}_2 + i\alpha_R\sqrt{\kappa_2}\chi_{sr}^r\chi_m^r\sqrt{\gamma_m}\hat{\eta} + \sqrt{\kappa_2}\chi_{sr}^r\chi_{ba}^r\sum_{j=1,2,I}\sqrt{\kappa_j}\hat{\zeta}_j \tag{A.8}$$

Using Eq. A.8 we can compute the symmetric-in-frequency noise spectrum, $\bar{S}_{\hat{\mathcal{A}}_2}^R$, associated with this field. This is given by[††††]

$$\bar{S}_{\hat{\mathcal{A}}_2}^R[\omega] = \frac{1}{2}\int_{-\infty}^{+\infty}\langle\{\hat{\mathcal{A}}_2[\omega+\delta_R], \hat{\mathcal{A}}_2^{\dagger}[\omega']\}\rangle\frac{d\omega'}{2\pi}$$

$$= [1 + \kappa_2(\chi_{sr}^r\chi_{ba}^r + \chi_{sr}^{r*}\chi_{ba}^{r\,*})]\left(\bar{n}_2^T + \frac{1}{2}\right) + \kappa_2|\alpha_R|^2|\chi_m^r|^2|\chi_{sr}^r|^2\gamma_m\left(\bar{n}_m^T + \frac{1}{2}\right)$$

$$+ \kappa_2|\chi_{sr}^r|^2|\chi_{ba}^r|^2\kappa\left(\bar{n}_{sr,R}^T + \frac{1}{2}\right) \tag{A.9}$$

In Eq. A.9, the susceptibilities are computed at $\omega + \delta_R$ to incorporate the fact that the sideband is detuned from the cavity resonance. Given that the only source of noise

[††††] From the ansatz, $\hat{a}(t) = \hat{a}_r(t)e^{i\delta_R t} \Rightarrow \hat{a}[\omega] = \hat{a}_r[\omega+\delta_R]$. And hence we use $\hat{\mathcal{A}}_2[\omega+\delta_R]$ and not $\hat{\mathcal{A}}_2[\omega]$ in Eq. 2.65

entering at port 2 is vacuum noise as we drive our system exclusively at port 1, we let $\bar{n}_2^T = 0$. We expect that any excess thermal noise driving the cavity is due entirely to internal losses, implying $\bar{n}_{sr,R}^T = (1/\kappa)\sum_{j=1,I} \kappa_j \bar{n}_j^T$. Using these facts in the above expression and simplifying in the relevant weak coupling limit, $\delta\omega_m^R \ll \Gamma_t^R \ll \kappa \ll \omega_m$, we get Eq. 2.58.

Appendix 2: Single Blue Drive: Backaction heating, Negative Temperature

Appendix 2.1: Equation of Motion for the Single Blue Drive

We sketch the derivation below for the NR-SR system driven by a single blue signal such that $\mathcal{E}_1 = 0$ in Eq. 2.54a. Figure 2.9a) shows a schematic sketch of the pump configuration. We use the ansatz $\hat{a}(t) = \hat{a}_b(t)e^{-i\delta_B t} + \hat{a}_+(t)e^{-i(\omega_m+\delta_B)t}$ where $\delta_B = -\Delta_2 - \omega_m$ is the frequency of the blue sideband relative to the SR frequency. The first term represents the sideband that results from the Stokes scattering process and the second term is the steady state drive term from the blue source. Substituting this ansatz into Eq. 2.54 and defining the effective coupling $\alpha_B = g x_{xpf}\langle a_+(t \to \infty)\rangle$ from the steady states equation, we can write

$$\partial_t \hat{a}_b(t) = -\left(-i\delta_B + \frac{\kappa}{2}\right)\hat{a}_b(t) - i\alpha_B \hat{c}^\dagger(t) - \sqrt{\kappa}\hat{a}_{bin}(t) \qquad (A.10a)$$

$$\partial_t \hat{c}(t) = -i\alpha_B \hat{a}_b^\dagger(t) - \frac{\gamma_m}{2}\hat{c}(t) - \sqrt{\gamma_m}\hat{c}_{in}(t) \qquad (A.10b)$$

Fourier transforming Eq. A.10, linearizing it as in the single red drive case and then collecting the quantum noise terms gives the system of equations

$$\hat{d}_b[\omega] = \chi_{sr}^b[\omega]\left[i\alpha_B \hat{c}^\dagger[\omega] + \sqrt{\kappa}\hat{d}_{bin}[\omega]\right] \qquad (A.11a)$$

$$\hat{c}[\omega] = \chi_m[\omega]\left[i\alpha_B \hat{d}_b^\dagger[\omega] + \sqrt{\gamma_m}\hat{c}_{in}[\omega]\right] \qquad (A.11b)$$

where $\chi_{sr}^{b}[\omega] = 1/\left[i(\omega + \delta_B) - \frac{\kappa}{2}\right]$ is the cavity susceptibility for the blue sideband. Solving the resulting matrix equation that arises from Eq. A.11 and its Hermitian conjugate counterpart, we get

$$\hat{d}_b = \chi_{sr}^{b}\chi_{ba}^{b}\sqrt{\kappa}\hat{d}_{bin} + i\alpha_B\chi_{sr}^{b}\bar{\chi}_{m}^{b}\sqrt{\gamma_m}\hat{c}_{in}^{\dagger} \quad (A.12a)$$

$$\hat{c} = \chi_{m}^{b}\left[i\alpha_B\bar{\chi}_{sr}^{b}\sqrt{\kappa}\hat{d}_{bin}^{\dagger} + \sqrt{\gamma_m}\hat{c}_{in}\right] \quad (A.12b)$$

where $\chi_{m}^{b}[\omega] = \frac{\chi_m[\omega]}{1-|\alpha_B|^2\bar{\chi}_{sr}^{b}[\omega]\chi_m[\omega]}$ is the effective mechanical susceptibility in the presence of cavity backaction from the blue pump, and $\chi_{ba}^{b}[\omega] = 1 + |\alpha_B|^2\chi_{sr}^{b}[\omega]\bar{\chi}_{m}^{b}[\omega]$. Notice also in Eq. A.12 that we have used the notation $\bar{\chi}[\omega] = \chi^*[-\omega]$ for all the susceptibilities. For an n-port device, Eq. A.12 takes the form

$$\hat{d}_r = \chi_{sr}^{b}\chi_{ba}^{b}\sum_{j=1}^{n}\sqrt{\kappa_j}\hat{\zeta}_j + i\alpha_B\chi_{sr}^{b}\bar{\chi}_{m}^{b}\sqrt{\gamma_m}\hat{\eta}^{\dagger} \quad (A.12a')$$

$$\hat{c} = \chi_{m}^{b}\left[i\alpha_B\bar{\chi}_{sr}^{b}\sum_{j=1}^{n}\sqrt{\kappa_j}\hat{\zeta}_j^{\dagger} + \sqrt{\gamma_m}\hat{\eta}\right] \quad (A.12b')$$

Again we limit ourselves to the case where $n = 3$, with $j = 1,2,I$ only as in the single red drive case of section 2.2.2.1.

Appendix 2.2: Output Spectrum for the Single Blue Drive

For the blue drive, the output microwave field leaving port 2 is given by

$$\hat{\mathcal{A}}_2 = \hat{\zeta}_2 + i\alpha_B\sqrt{\kappa_2}\chi_{sr}^{b}\bar{\chi}_{m}^{b}\sqrt{\gamma_m}\hat{\eta}^{\dagger} + \sqrt{\kappa_2}\chi_{sr}^{b}\chi_{ba}^{b}\sum_{j=1,2,I}\sqrt{\kappa_j}\hat{\zeta}_j \quad (A.13)$$

The symmetric-in-frequency noise spectrum, $\bar{S}_{\hat{\mathcal{A}}_2}^{B}$, associated with this field is

$$\bar{S}_{\hat{\mathcal{A}}_2}^{B}[\omega] = \frac{1}{2}\int_{-\infty}^{+\infty}\langle\{\hat{\mathcal{A}}_2[\omega - \delta_B], \hat{\mathcal{A}}_2^{\dagger}[\omega']\}\rangle\frac{d\omega'}{2\pi}$$

$$= \left[1 + \kappa_2\left(\chi_{sr}^{b}\chi_{ba}^{b} + \chi_{sr}^{b*}\chi_{ba}^{b\,*}\right)\right]\left(\bar{n}_2^T + \frac{1}{2}\right) + \kappa_2|\alpha_B|^2|\bar{\chi}_{m}^{b}|^2|\chi_{sr}^{b}|^2\gamma_m\left(\bar{n}_m^T + \frac{1}{2}\right)$$

$$+ \kappa_2|\chi_{sr}^{b}|^2\left|\chi_{ba}^{b}\right|^2\kappa\left(\bar{n}_{sr,B}^T + \frac{1}{2}\right) \quad (A.14)$$

Neglecting $\bar{n}_2^T$ and using the weak coupling approximation, Eq. A.14 simplifies to Eq. 2.64

Appendix 3: Double Pump Drive: Separated Sidebands

Appendix 3.1: Equation of Motion for Double Pump Drive with Separated Sidebands

As in the previous two appendices where we studied the single red and single blue pump configuration, we begin by considering a suitable ansatz to Eq. 2.54. For the double pump configuration with serparated sidebands, Eq. 2.54 can be solved using the ansatz $\hat{a}(t) = \hat{a}_r(t)e^{i\delta_R t} + \hat{a}_b(t)e^{-i\delta_B t} + \hat{a}_-(t)e^{i(\omega_m+\delta_R)t} + \hat{a}_+(t)e^{-i(\omega_m+\delta_B)t}$ where δ_R and δ_B are the frequencies of the red and blue sidebands relative to the SR frequency (see Figure 2.12(a)). Substituting this ansatz into Eq. 2.54 and collecting terms that oscillate at the same frequency, we get

$$\partial_t \hat{a}_r(t) = -\left(i\delta_R + \frac{\kappa}{2}\right)\hat{a}_r(t) - i\alpha_R\hat{c}(t) - \sqrt{\kappa}\hat{a}_{rin}(t) \quad (A.15a)$$

$$\partial_t \hat{a}_b(t) = -\left(-i\delta_B + \frac{\kappa}{2}\right)\hat{a}_b(t) - i\alpha_B\hat{c}^\dagger(t) - \sqrt{\kappa}\hat{a}_{bin}(t) \quad (A.15b)$$

$$\partial_t \hat{c}(t) = -i\left[\alpha_R^*\hat{a}_r(t) + \alpha_B\hat{a}_b^\dagger(t)\right] - \frac{\gamma_m}{2}\hat{c}(t) - \sqrt{\gamma_m}\hat{c}_{in}(t) \quad (A.15c)$$

where $\alpha_R = gx_{xpf}\langle\hat{a}_-(t)\rangle$ and $\alpha_B = gx_{xpf}\langle\hat{a}_+(t)\rangle$ are the effective coupling constants resulting from the red and blue drives respectively. Fourier transforming and then linearizing the cavity fields of Eq. A.15, gives the system of equation

$$\hat{d}_r[\omega] = \chi_{sr}^r[\omega]\left[i\alpha_R\hat{c}[\omega] + \sqrt{\kappa}\hat{d}_{rin}[\omega]\right] \quad (A.16a)$$

$$\hat{d}_b[\omega] = \chi_{sr}^b[\omega]\left[i\alpha_B\hat{c}^\dagger[\omega] + \sqrt{\kappa}\hat{d}_{bin}[\omega]\right] \quad (A.16b)$$

$$\hat{c}[\omega] = i\chi_m[\omega]\left[\alpha_R^*\hat{d}_r[\omega] + \alpha_B\hat{d}_b^\dagger[\omega] + \sqrt{\gamma_m}\hat{c}_{in}[\omega]\right] \quad (A.16c)$$

Using matrix algebra, Eq. A.16 and its corresponding Hermitian conjugate can be solved to give

$$\hat{d}_r = \chi_{sr}^r \chi_{ba}^{tr} \sqrt{\kappa} \hat{d}_{rin} - \alpha_R \alpha_B \bar{\chi}_{sr}^b \chi_{sr}^r \chi_m^{br} \sqrt{\kappa} \hat{d}_{bin}^\dagger + i\alpha_R \chi_{sr}^r \chi_m^{br} \sqrt{\gamma_m} \hat{c}_{in} \quad (A.17a)$$

$$\hat{d}_b = \chi_{sr}^b \chi_{ba}^{tb} \sqrt{\kappa} \hat{d}_{bin}^\dagger + \alpha_R \alpha_B \bar{\chi}_{sr}^r \chi_{sr}^b \bar{\chi}_m^{br} \sqrt{\kappa} \hat{d}_{rin} + i\alpha_B \chi_{sr}^b \bar{\chi}_m^{br} \sqrt{\gamma_m} \hat{c}_{in}^\dagger \quad (A.17b)$$

$$\hat{c} = \chi_m^{br} \left[i\alpha_R^* \chi_{sr}^r \sqrt{\kappa} \hat{d}_{rin} + i\alpha_B \bar{\chi}_{sr}^b \sqrt{\kappa} \hat{d}_{bin}^\dagger + \sqrt{\gamma_m} \hat{c}_{in} \right] \quad (A.17c)$$

where $\chi_m^{br}[\omega] = \frac{\chi_m[\omega]}{1+\chi_m[\omega]\left(|\alpha_R|^2 \chi_{sr}^r[\omega] - |\alpha_B|^2 \bar{\chi}_{sr}^b[\omega]\right)}$ is the effective mechanical susceptibility in the presence of cavity backaction from both the red and the blue pumps, $\chi_{ba}^{tr} = 1 - |\alpha_R|^2 \chi_{sr}^r \chi_m^{br}$ and $\chi_{ba}^{tb} = 1 + |\alpha_B|^2 \chi_{sr}^b \bar{\chi}_m^{br}$. Eq. A.17 gives the solution of the field operators inside the cavity for any n-port device. To see this, replace c_{in} by η and $\sqrt{\kappa}\hat{d}_{r(b)in}$ by $\sum_{j=1}^n \sqrt{\kappa_j} \hat{\zeta}_j^{r(b)}$ where $\hat{\zeta}_j^{r(b)}$ describes the noise entering the cavity from port j due to the red (blue) source. I have assumed that there are no cross-correlations between the input noise of the red and blue pumps. That would mean for instance that $\langle a_{rin}^\dagger a_{bin} \rangle = \langle a_{bin} a_{rin}^\dagger \rangle = 0$. We limit ourselves to the case where $n = 3$, with $j = 1,2,I$ only.

Appendix 3.2: Output Spectrum for Double Pump Drive with Separated Sidebands

The output field, $\hat{\mathcal{A}}_2$, leaving the cavity at port 2 is given by

$$\hat{\mathcal{A}}_2 = \hat{\zeta}_2 + \sqrt{\kappa_2} \hat{d}$$

where $\hat{d} = \hat{d}_r + \hat{d}_b$, $\hat{\zeta}_2 = \hat{\zeta}_2^r + \hat{\zeta}_2^b$ and similarly $\hat{\mathcal{A}}_2 = \hat{\mathcal{A}}_2^r + \hat{\mathcal{A}}_2^b$. Thus the output noise spectrum

$$\bar{S}_{\hat{\mathcal{A}}_2}[\omega] = \frac{1}{2} \int_{-\infty}^{+\infty} \langle \{ \hat{\mathcal{A}}_2^r[\omega + \delta_R] + \hat{\mathcal{A}}_2^b[\omega - \delta_B], \hat{\mathcal{A}}_2^\dagger[\omega'] \} \rangle \frac{d\omega'}{2\pi} = \bar{S}_{\hat{\mathcal{A}}_2^r}[\omega] + \bar{S}_{\hat{\mathcal{A}}_2^b}[\omega]$$

Where

$$\bar{S}_{\hat{\mathcal{A}}_2^r}[\omega] = \frac{1}{2} \int_{-\infty}^{+\infty} \langle \{ \hat{\mathcal{A}}_2^r[\omega + \delta_R], \hat{\mathcal{A}}_2^{r\,\dagger}[\omega'] \} \rangle \frac{d\omega'}{2\pi}$$

$$= [1 + \kappa_2 (\chi_{sr}^r \chi_{ba}^{tr} + \chi_{sr}^{r*} \chi_{ba}^{tr\,*})] \left(\bar{n}_2^T + \frac{1}{2} \right)$$

$$+\kappa_2|\alpha_R|^2|\chi_m^{br}|^2|\chi_{sr}^r|^2\gamma_m\left(\bar{n}_m^T+\frac{1}{2}\right)$$

$$+\kappa_2|\chi_{sr}^r|^2|\chi_{ba}^{tr}|^2\kappa\left(\bar{n}_{sr,R}^T+\frac{1}{2}\right)$$

$$+\kappa_2|\alpha_R|^2|\alpha_B|^2|\chi_{sr}^r|^2|\bar{\chi}_{sr}^b|^2|\chi_m^{br}|^2\kappa\left(\bar{n}_{sr,B}^T+\frac{1}{2}\right) \quad \text{(A. 18)}$$

and

$$\bar{S}_{\hat{\mathcal{A}}_2^b}[\omega]=\frac{1}{2}\int_{-\infty}^{+\infty}\langle\{\hat{\mathcal{A}}_2^b[\omega-\delta_B],\hat{\mathcal{A}}_2^{b\,\dagger}[\omega']\}\rangle\frac{d\omega'}{2\pi}$$

$$=\left[1+\kappa_2\left(\chi_{sr}^b\chi_{ba}^{tb}+\chi_{sr}^{b*}\chi_{ba}^{tb\,*}\right)\right]\left(\bar{n}_2^T+\frac{1}{2}\right)$$

$$+\kappa_2|\alpha_B|^2|\bar{\chi}_m^{br}|^2|\chi_{sr}^b|^2\gamma_m\left(\bar{n}_m^T+\frac{1}{2}\right)$$

$$+\kappa_2|\chi_{sr}^b|^2\left|\chi_{ba}^{tb}\right|^2\kappa\left(\bar{n}_{sr,B}^T+\frac{1}{2}\right)$$

$$+\kappa_2|\alpha_R|^2|\alpha_B|^2|\chi_{sr}^r|^2|\bar{\chi}_{sr}^b|^2|\chi_m^{br}|^2\kappa\left(\bar{n}_{sr,B}^T+\frac{1}{2}\right) \quad \text{(A. 19)}$$

Assuming $\bar{n}_2^T=0$ and for the weak coupling regime, a few steps of algebra simplifies Eq. A.18 and A.19 to give Eq 2.71 and Eq 2.72 respectively.

Appendix 4: Double Pump Drive: Overlapped Sidebands

Appendix 4.1: Equation of Motion for Double Pumps with Overlapped Sidebands

The equations of motion can be solved for the overlapped sideband case by substituting the ansatz, $\hat{a}(t)=\hat{a}_o(t)+\hat{a}_1(t)e^{i\omega_m t}+\hat{a}_1(t)e^{-i\omega_m t}$ into Eq. 2.54. Linearizing the field operators in the usual way, we can write the system of equations of the quantum noise terms as

$$\partial_t\hat{d}(t)=-\frac{\kappa}{2}\hat{d}(t)-i\alpha\left[\hat{c}(t)\left(1+e^{-i2\omega_m t}\right)+h.c.\right]-\sqrt{\kappa}\hat{d}_{in}(t) \quad \text{(A. 20}a\text{)}$$

$$\partial_t\hat{c}(t)=-\frac{\gamma_m}{2}\hat{c}(t)-i\alpha\left(1+e^{i2\omega_m t}\right)\left(\hat{d}(t)+\hat{d}^\dagger(t)\right)-\sqrt{\gamma_m}\hat{c}_{in}(t) \quad \text{(A. 20}b\text{)}$$

where $\alpha=gx_{xpf}\langle\hat{a}_1(t)\rangle=\alpha_R=\alpha_B$ is the effective coupling strength.

Appendix 4.2: Mechanical Occupation for Overlapped Sideband

Fourier transforming Eq. A.20 and solving the resulting equations by matrix algebra, we can write the position spectrum as

$$S_{xx}[\omega] = x_{zpf}^2 |\chi_m[\omega]|^2 \{\gamma_m(2\bar{n}_m^T + 1) + 2\Gamma(\bar{n}_{sr}^T + 1)\} \quad (A.21)$$

In Eq. A.21, $\Gamma = 4|\alpha|^2/\kappa = \Gamma_B(0) = \Gamma_R(0)$ is proportional to the strength of the individual pumps and $\bar{n}_{sr}^T$ is the thermal occupation of the SR. Integrating Eq. A.21 and collecting terms, we can write the detailed balanced equation for the overlapped sidebands as

$$\bar{n}_m = \bar{n}_m^T + \bar{n}_{BA} \quad (A.22)$$

where $\bar{n}_{BA} = 2\frac{\Gamma}{\gamma_m}(\bar{n}_{sr}^T + 1)$ is associated with backaction heating.

Appendix 4.3: Position spectrum of Quadratures

Writing the solution of Eq. A.20 in terms of the quadratures in frequency space, we get

$$\hat{X}_1[\omega] = x_{zpf}\chi_m[\omega]\{\sqrt{\gamma_m}(\hat{\eta}[\omega] + \hat{\eta}^\dagger[\omega]) + i\alpha(\hat{F}_{BA}[\omega + 2\omega_m] - \hat{F}_{BA}[\omega - 2\omega_m])\} \quad (A.23a)$$

$$\hat{X}_2[\omega] = -ix_{zpf}\chi_m[\omega]\{\sqrt{\gamma_m}(\hat{\eta}[\omega] - \hat{\eta}^\dagger[\omega]) - i\alpha(2\hat{F}_{BA}[\omega] + \hat{F}_{BA}[\omega + 2\omega_m] + \hat{F}_{BA}[\omega - 2\omega_m])\} \quad (A.23b)$$

where $\hat{F}_{BA}[\omega] = \chi_m[\omega]\sum_j \sqrt{\kappa_j}(\hat{\zeta}_j[\omega] + \hat{\zeta}_j^\dagger[\omega])$. Thus the position spectral density of the quadratures are given by [31]

$$S_{X_1}[\omega] = x_{zpf}^2 |\chi_m[\omega]|^2 \gamma_m\{1 + 2(\bar{n}_m^T + \bar{n}_{bad})\} \quad (A.24a)$$

$$S_{X_2}[\omega] = x_{zpf}^2 |\chi_m[\omega]|^2 \gamma_m\{1 + 2(\bar{n}_m^T + \bar{n}_{bad} + \bar{n}_{BA})\} \quad (A.24b)$$

where $\bar{n}_{bad} = \frac{\bar{n}_{BA}}{32}\left(\frac{\kappa}{\omega_m}\right)^2$ is the backaction heating associated with the bad cavity limit. Eq. 2.76 is the exact copy of Eq. A.24 above.

REFERENCES

[1] Schwab, K.C., Roukes, M.L., "Putting Mechanics into Quantum Mechanics," Physics Today **58**, 36 (2005.)

[2] LaHaye, M., Buu, O., Camarota, B., Schwab, K., Science **304**, 74 (2004).

[3] Teufel, J. D. , Harlow, J. W., Regal, C. A., Lehnert, K. W., *Phys. Rev. Lett.*, **101**, 197203 (2008)

[4] Schliesser, A., Arcizet, O., Rivière, R., Anetsberger, G., Kippenberg, T.J., Nature Physics **5**, 509 (2009)

[5] Park, Y.-S., Wang, H., Nature Physics **5**, 489-493 (7 June 2009)

[6] Gröblacher, S., Hertzberg, J.B., Vanner, M.R., Cole, G.D., Gigan, S., Schwab, K.C., Aspelmeyer, M., Nature Physics 5, 485 - 488 (2009)

[7] Naik, A., Buu, O., LaHaye, M.D., Armour, A.D., Clerk, A.A., Blencowe, M.P., Schwab, K.C., Nature **443**, 193-196 (2006).

[8] Rocheleau, T., Ndukum, T., Macklin, C., Hertzberg, J. B., Clerk, A. A., Schwab, K. C., Nature **463**, 72-75 (2010)

[9] O'Connell, A. D., Hofheinz, M., Ansmann, M., Bialczak, R. C., Lenander, M., Lucero, E., Neeley, M., Sank, D., Wang, H., Weides, M., Wenner, J. , Martinis, J. M., Cleland, A. N. , Nature **464**, 697-703 (2010)

[10] Regal, C. A., Teufel, J. D., Lehnert, K. W., *Nature Physics*, **4**, 555 (2008).

[11] Marquardt, F., Chen, J. P., Clerk, A. A., Girvin, S. M., Phys. Rev. Lett. **99**, 093902 (2007).

[12] Marquardt, F., Clerk, A. A., Girvin, S. M., J. Mod. Optics **55**, 3329 (2008).

[13] Wilson-Rae, I., Nooshi, N., Zwerger, W., Kippenberg, T.J., Phys. Rev. Lett. **99**, 093901 (2007)

[14] Xue, F., Wang, Y.D., Liu, Y.-X., Nori, F., Phys. Rev. B 76, 205302 (2007)

[15] Day, P. K., LeDuc, H. G., Mazin, B. A., Vayonakis, A., Zmuidzinas, J., Nature **425** 817 (2003)

[16] Frunzio, L., Wallraff, A., Schuster, D., Majer, J., Schoelkopf, R., IEEE Trans Appl Sup **15** 860 (2005)

[17] O'Conell, A. D., Ansmann, M., Bialczak, R. C., Hofheinz, M., Katz, N., Lucero, E., McKenney, C., Neeley, M., Wang, H., Weig, E. M., Cleland, A. N., Martinis, J. M., Appl Phys Letts **92** 112903 (2008)

[18] A. A. Clerk, M. H. Devoret, S. M. Girvin, F. Marquardt and R. J. Schoelkopf, arXiv:0810.4729v1, Rev. Mod. Phys. **82**, 1155 (2010).

[19] Blais, A., Huang, R.-S., Wallraff, A., Girvin, S. M., Schoelkopf, R. J., Phys. Rev. A **69**, 062320 (2004)

[20] B. Yurke, J. S. Denker, Phys. Revs. A, **29**, 1419 (1984)

[21] D. F. Walls, G. J. Milburn, Quantum Optics (Springer, New York, 1995)

[22] M. J. Collet, C. W. Gardiner, Phys. Rev. A, **30**, 1386 (1984)

[23] M. J. Collet, C. W. Gardiner, Phys. Rev. A, **31**, 3761 (1985)

[24] Casimir, H. B. G., Proc. Kon. Ned. Akad. Wetenschap **51** 793 (1948)

[25] Bell, D. A. , *Electrical Noise: Fundamental and Physical Mechanism*, London, Von Nostrand, 1960

[26] Milonni, P. W., *The Quantum Vacuum*, Boston Academic Press, 1994

[27] Beenakker, C., Schönenberger, C., Physics Today, page 37, May 2003

[28] For a literature review on shot noise, see for instance Blanter, Y. M., Büttiker, M., Phys. Rep. **336**, 1 (2000)

[29] Private communication with Aash A. Clerk … notes on Schwab group server

[30] Wooley, M. J., Doherty, A. C., Milburn, G. J., Schwab, K. C., Phys Rev A **78**, 062303 (2008)

[31] Clerk, A. A., Marquardt, F., Jacobs, K., New J. Phys. 10, 095010 (2008).

[32] Caves,C M, Thorne, K S, Drever RWP, Sandberg V D, Zimmermann M Rev. Mod. Phys. **52** 341–92 (1980)

Bocko M F, Onofrio R Rev. Mod. Phys. **68** 755–99 (1996)

Caves C M Phys. Rev. D **26** 1817–39 (1982)

[33] Hertzberg, J. B., Rocheleau, T., Ndukum, T., Savva, M., Clerk, A. A., Schwab, K. C., Nature Phys. **6**, 213 (2010)

[34] Matthew D. LaHaye, *The Radio-Frequency Single-Electron Transistor Displacement Detector*, PhD thesis, University of Maryland, College Park, 2005.

[35] Akshay Naik, *Near Quantum Limited Measurement in Nanoelectromechanical Systems*, PhD thesis, University of Maryland, College Park, 2006.

[36] Patrick Truitt, *Measurement of coupling between the electron gas and nanomechanical modes*, PhD Thesis, University of Maryland, College Park, 2007

[37] Jared Hertzberg, *Back-action Evading Measurements of Nanomechanical Motion Approaching Quantum Limits*, PhD Thesis, University of Maryland, College Park, 2009.

[38] G. Hammer, S. Wuensch, M. Roesch, K. Ilin, E. Crocoll, and M. Siegel, *Superconducting coplanar waveguide resonators for detector applications*, Supercond. Sci. Technol., 20:S408, October 2007.

K. C. Gupta, Ramesh Garg, and I. J. Bahl, *Microstrip Lines and Slotlines*, Artech House, Dedham, MA, 1979.

Rainee N. Simons, *Coplanar Waveguide Circuits, Components, and Systems*, John Wiley and Sons, New York, 2001.

[39] Alley, G. D. IEEE Trans M. T. T., **18** 1028 1970

[40] Esfandiari, R., Maki, D. W., Siracusa, M. IEEE Trans M. T. T. **31** 57 1983

[41] David M. Pozar, *Microwave Engineering*, John Wiley and Sons, third edition, 2005.

[42] David Isaac Schuster, *Circuit Quantum Electrodynamics*, PhD thesis, Yale

University, 2007.

[43] Verbridge, S. S., Shapiro, D. F., Craighead, H. G., Parpia, J. M., Nano Letts **7** 1728 (2007)

[44] C. Kittel, *Introduction to Solid State Physics, 1st ed. 1953 - 8th ed. 2005, ISBN 047141526X*

[45] Verbridge, S. S., Parpia, J. M., Reichenbach, R. B., Bellan, L. M., Craighead, H. G., J Appl Phys **99** 124304 (2006)

[46] www.cnf.cornell.edu

[47] http://www.mri.psu.edu/Facilities/NNIN/Index.asp

[48] Silicon Quest Internation - http://www.siliconquest.com/

Silicon Valley Microelectronics - http://www.svmi.com/

Ultrasil - http://www.ultrasil.com/

[49] http://www.jpl.nasa.gov/

[50] Pobell, F., *Matter and Methods at Low Temperatures*, 3rd, rev. and exp. Ed., Springer 2007.

[51] Richardson, R. C., Smith, E. N., *Experimental Techniques in Condensed Matter Physics at Low Temperatures*, Westview Press, 1998.

[52] DeLong, L. E., Symko, O. G., Wheatley, J. C., Rev Sci Instr **42** 147 (1971)

[53] http://www.oxinst.net/

[54] http://www.techmfg.com/

[55] Biquard, F., Septier, A. Nuclear Instr and Methods **44** (1) 18-28 (1966).

[56] Benjamin A. Mazin, *Microwave Kinetic Inductance Detectors*, PhD thesis, California Institute of Technology, 2004.

[57] Bardeen, J. Phys Rev Letts, **1** 399 (1958)

[58] Mattis, D. C., Bardeen, J., Phys Rev **111** 412 (1958)

[59] Halbritter, J., Z. Physik **266** 209 (1974)

[60] Linden, D. S., Orlando, T. P., Lyons, W. G., IEEE Trans Appl Sup **4** 136 (1994)

[61] Vendik, O. G., Vendik, I. B., Kaparkov, D. I., IEEE Trans M. T. T. **46** 469 (1998)

[62] Gibbons, D. F., Phys. Rev. **112**, 2139 (1958).

[63] Wilson-Rae, I., Phys. Rev. B **77**, 245418 (2008)

[64] Quirin P. Unterreithmeier, Thomas Faust, and Jörg P. Kotthaus, Phys. Rev. Lett. **105**, 027205 (2010)

[65] Cross ,M. C., Lifshitz, R., Phys. Rev. B **64**, 085324 (2001)

[66] Lifshitz, R., Roukes, M. L., Phys. Rev. B **61**, 5600, 2000

[67] Löhneysen, H. v., Phys. Rep. **79**, 161 (1981).

[68] Hoehne, F., Pashkin, Y, A., Astafiev, O., Faoro, L., Ioffe, L. B., Nakamura, Y., Tsai, J. S., Phys Rev B **81** 184112 (2010)

[69] Hunklinger, S. Raychaudhuri, A. K., Prog. Low Temp. Phys. **9**, 265 (1986)

[70] Fefferman, A. D. , Pohl, R. O., Zehnder, A. T., Parpia, J. M., Phys Rev Lett **100,** 195501 (2008)

[71] Kleiman, R. N., Agnolet, G., Bishop D. J., Phys Rev Lett **59** 2079 (1987)

[72] Southworth, D. R., Barton, R. A., Verbridge, S. S., Ilic, B., Fefferman, A. D., Craighead, H. G., Parpia, J. M. Phys Rev Letts **102**, 225503 (2009)

[73] Black, J. L., Fulde, P., Phys. Rev. Lett. **43**, 453 (1979)

[74] König, R., Ramos, M. A., Usherov-Marshak, I., Arcas-Guijarro, J., Hernando-Mañeru, A., Esquinazi, P., Phys. Rev. B **65**, 180201 (2002).

[75] Liu, X., Thompson, E., White Jr., B. E., Pohl, R. O. Phys Rev B 59 11767 (1999)

[76] Fefferman, A. D., Pohl, R. O., Parpia, J. M., Phys Rev B **82**, 064302 (2010)

[77] Phillips, W. A., Rep. Prog. Phys. **50**, 1657 _1987_.

[78] Yu, C. C., Leggett, A. J., Comments Condens. Matter Phys. **14**, 231 _1988_.

[79] Jiansong Gao, *The Physics of Superconducting Microwave Resonators*, PhD Thesis, CalTech, Pasadena, 2008

[80] Teufel, J. D., Regal, C. A. & Lehnert, K. W., New J. Phys. **10**, 095002 (2008).

[81] Diedrich, F., Bergquist J. C., Itano, W. M., Wineland, D. J., Phys Rev Letts **66** 403 (1989)

[82] Bergquist J. C., Hulet, R. G., Itano, W. M., Wineland, D. J., Phys Rev Letts **57** 1699 (1986)